2008-04-01

Numerical Analysis of Passive Force on Skewed BridgeAbutments with Reinforced Concrete Wingwalls

Scott Karl Snow
Brigham Young University

Numerical Analysis of Passive Force on Skewed Bridge Abutments with Reinforced Concrete Wingwalls

Scott Karl Snow

A thesis submitted to the faculty of
Brigham Young University
in partial fulfillment of the requirements for the degree of

Master of Science

Kyle M. Rollins, Chair
Fernando S. Fonseca
Norman L. Jones

Department of Civil and Environmental Engineering

Brigham Young University

ABSTRACT

Numerical Analysis of Passive Force on Skewed Bridge Abutments with Reinforced Concrete Wingwalls

Scott Karl Snow
Department of Civil and Environmental Engineering, BYU
Master of Science

Historically bridges with skewed abutments have proven more likely to fail during earthquake loadings (Toro et al, 2013) when compared to non-skewed bridges (Apirakvorapinit et al. 2012; Elnashai et al. 2010). Previous studies including small-scale laboratory tests by Jessee (2012), large-scale field tests by Smith (2014), and numerical modeling by Shamsabadi et al. (2006) have shown that 45° skewed bridge abutments experience a reduction in peak passive force by about 65%. With numerous skewed bridges in the United States, this study has great importance to the nation's infrastructure.

The finite element models produced in this study model the large-scale field-testing performed by Smith (2014), which was performed to study the significant reduction in peak passive resistance for abutments with longitudinal reinforced concrete wingwalls. The finite element models largely confirm the findings of Smith (2014). Two models were created and designed to match the large-scale field tests and were used to calibrate the soil parameters for this study. Two additional models were then created by increasing the abutment widths from 11 feet to 38 feet to simulate a two-lane bridge. The 45° skewed 11-foot abutment experienced a 38% reduction in peak passive resistance compared to the non-skewed abutment. In contrast, the 45° skewed 38-foot abutment experienced a 65% reduction in peak passive resistance compared to the non-skewed abutment. When the wingwalls are extended 10 feet into the backfill the reduction decreased to 59% due to the change in effective skew angle.

The finite element models generally confirmed the findings of Smith (2014). The results of the 11- and 38-foot abutment finite element models confirmed that the wingwall on the obtuse side of the 45° skewed abutments experienced approximately 4 to 5 times the amount of horizontal soil pressure and 5 times the amount of bending moment compared to the non-skewed abutment. Increases in the pressures and bending moments are likely caused by soil confined between the obtuse side of the abutment and the wingwall.

A comparison of the 11- and 38-foot 45° skewed abutment models showed a decrease in the influence of the wingwalls as the abutment widened. The wingwall on the acute side of the 38-foot abutment developed approximately 50% of the horizontal soil pressure compared to the 11-foot abutment. The heave distribution of the 11-foot abutment showed approximately 1- to 2-inches of vertical displacement over a majority of the abutment backwall versus more than half of the 38-foot abutment producing ½ an inch or less.

Keywords: abutments, backfill, bending moment, deflection, displacement, earthquake, finite element, heave, passive force, pressure, reduction, Rollins, Shamsabadi, skew

ACKNOWLEDGEMENTS

I would like to thank my graduate advisor, Dr. Kyle M. Rollins, for giving me the opportunity to work with him on this project and for his mentorship and patience throughout the research and writing process. I would also like to thank Dr. Kevin W. Franke for teaching with a passion that helped me develop my interest in geotechnical engineering.

I'm thankful for my wife, Lauren, and for her encouragement and continual support through the long nights of modeling and performing this study. I am also grateful for parents who taught me the value of hard work and perseverance.

The Federal Highway Administration (FHWA) along with Departments of Transportation from the states of California, Minnesota, Montana, New York, Oregon and Utah supported this FHWA pooled fund study TPF-5(264). The Utah Department of Transportation served as the lead agency for the study. I sincerely appreciate their support and patience. While this research has been sponsored by these agencies, the opinions, recommendations, and conclusions from this study do not necessarily represent those of the supporting organizations.

TABLE OF CONTENTS

LIST OF TABLES

LIST OF FIGURES

1 INTRODUCTION

1.1 Background

Numerous studies have been performed to define the passive force-deflection relationships with varying soil types and abutment configurations, including large-scale tests on densely compacted granular backfills (Duncan and Mokwa 2001; Rollins and Sparks 2002; Cole and Rollins 2006; Lemnitzer et al. 2009). The results from these field tests have indicated that the peak passive force is obtained at a deflection of 3% to 5% of the abutment backwall height (Cole and Rollins 2006; Lemnitzer et al. 2009). Other studies have been performed to develop hyperbolic passive force-deflection curves to be used in design (Duncan and Mokwa 2001; Shamsabadi et al. 2006). Currently design specifications require the use of basic bilinear curves (Caltrans 2010; AASHTO 2011).

A specific area of concern is skewed bridge abutments. Historically, bridges with skewed abutments have proven more likely to fail during earthquake loadings (Toro et al. 2013). This is likely caused by the current design practices, which assume that the peak passive force is the same for both skewed and non-skewed bridge abutments (AASHTO 2011). Recently, a series of studies and large-scale field tests have been performed that explore this relationship (Jessee 2012; Smith 2014). Small-scale laboratory testing by Jessee (2012) focused on the relationship between skew angle and passive resistance. From this data, a reduction factor (R_{skew}) was developed to determine

the passive force for a skewed abutment ($P_{p\text{-}skew}$) relative to that for a non-skewed abutment ($P_{p\text{-}no\ skew}$). R_{skew} is computed using the equation

$$R_{skew} = \frac{P_{p-skew}}{P_{p-no\ skew}} = 8 * 10^{-5}\theta^2 - 0.018\theta + 1 \quad (1\text{-}1)$$

where θ is the skew angle in degrees. This relationship is supported by finite element results produced by Shamsabadi et al. (2006). Because this relationship is only supported by small-scale lab testing and a finite element model, it was determined that large-scale tests on skewed abutments were necessary to validate this relationship. A series of tests began in the summer of 2012 to investigate the effect of varying soil types and abutment geometries including abutments with transverse wingwalls (unconfined backfill), longitudinal MSE wingwalls, and longitudinal reinforced concrete wingwalls (Smith 2014). The test results generally confirmed the findings from the small-scale test except in the case with the reinforced concrete wingwalls. In that case, the reduction in resistance was far less than anticipated. Observations during testing suggest that this may have occurred because backfill soil was trapped at the wingwall/backwall interface and reduced the effective skew angle. Conceivably, this effect might become insignificant for wider abutment walls.

Ideally, physical tests would be performed with wider backfills than the 11 ft wide abutment that was used in the field tests, but this is not economically feasible. Instead, numerical models were calibrated with the results from the field tests (Smith 2014) and then simulations were performed with the numerical model. This approach was adopted by Guo (2015) for abutments with unconfined backfill. This approach should provide a reasonable means for assessing the behavior of skewed abutments with geometries more typical of those employed in practice.

1.2 Research Objectives

The research objectives of this study will include the following:

1. Use the results from large-scale tests with reinforced concrete wingwalls (Smith 2014) to calibrate material parameters for a numerical model.
2. Investigate the effect of wider abutment walls and varying soil properties on the passive force-deflection relationship and skew reduction factor for abutments with reinforced concrete wingwalls.
3. Develop relationships to help predict the structural and geotechnical response of reinforced concrete wingwalls during development of passive force on bridge abutments.

1.3 Scope

The breadth of this study will include modeling variations of skewed bridge abutments with longitudinally reinforced concrete wing-walls. To obtain reliable results, it is essential to calibrate the numerical models with the two large-scale field tests performed by Smith (2014). The 0° skew and 45° skew abutment tests will be recreated in Plaxis 3D and the soil parameters will be varied until acceptable agreement is achieved with the measured passive force-deflection curves. Once calibration has been completed, the skew angle and the width of the abutment will be varied and relevant test results will be computed.

2 LITERATURE REVIEW

2.1 Passive Earth Pressure Theories

Three primary theories that have been developed to predict passive earth pressures in a given soil are the Coulomb (1776), Rankine (1857), and Logarithmic Spiral (Log Spiral) theories. Each of these three theories differs in the assumed shear failure plane, and ultimately the method in predicting the passive earth pressure coefficient (K_p). Once this coefficient has been predicted, each theory uses Equation (2-1) to determine the passive earth pressure.

$$P_p=\frac{1}{2}K_p\gamma H^2+2\sqrt{K_p}c'H \quad (2\text{-}1)$$

where,

P_p = Ultimate passive force per unit width

K_p = Passive earth pressure coefficient

γ = Moist soil unit weight

H = Wall height

c' = Soil cohesion

2.1.1 Coulomb (1776)

The Coulomb Lateral Earth Pressure Theory, developed in 1776, was mathematically formulated based on a simple failure surface geometry. Coulomb defined the mobilization of the failure wedge using the following parameters: the soil friction angle (φ), the slope of the wall being

displaced into the soil (θ), the slope of the embankment being retained (α), and the friction angle at the soil-wall interface (δ). This geometry is depicted in Figure 2.1.

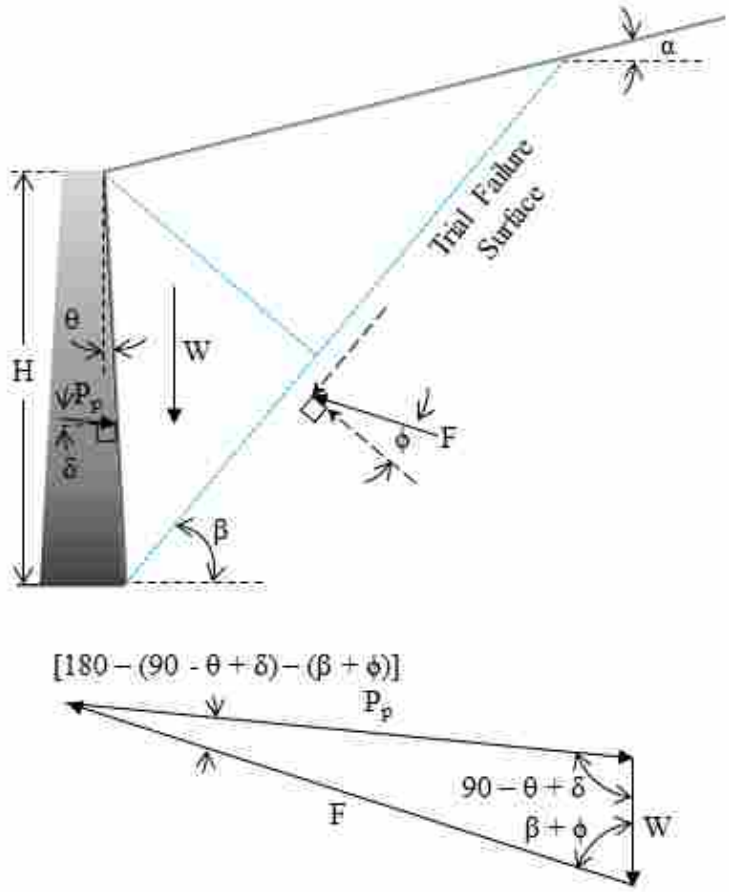

Figure 2.1. Coulomb shear plane geometry (Smith 2014).

Coulomb approximated the shear wedge as a linear failure plane while considering the soil interface friction. In order to obtain a solution, trial wedges with varying slopes are selected until a wedge produces the smallest passive force. This wedge is critical and the failure plane would likely occur along this orientation according to theory. However, the Coulomb theory tends to produce results that are extremely high when $\delta > 0.5\varphi$. Because this is a common condition with construction materials (Potyondy 1961), as shown below in Table 2.1, this theory is not recommended for use in design for passive force.

Table 2.1. Common Values of δ_{max}/φ, adapted from Potyondy (1961)

Soil type	δ_{max}/φ		
	Steel	Concrete	Wood
Sand	0.54	0.76	0.76
Silt and clay	0.54	0.5	0.55

2.1.2 Rankine (1857)

Rankine's Passive Earth Pressure Theory also assumes a linear failure surface but neglects wall friction at the soil-wall interface. This procedure determines the value of the passive force based on when the Mohr circle intercepts the Mohr-Coulomb failure envelope (Rankine 1857). Rankine described K_p with the Equation (2-2).

$$K_P=\frac{\cos\alpha+\sqrt{\cos^2\alpha-\cos^2\varphi}}{\cos\alpha-\sqrt{\cos^2\alpha-\cos^2\varphi}} \tag{2-2}$$

where,

φ = soil friction angle

α = embankment inclination

Rankine theory tends to predict a steeper slope for the shear plane, which results in a smaller failure wedge than would occur naturally. This smaller wedge produces a smaller, more conservative passive force resistance. Despite neglecting parameters such as interface friction angle, wall slope, or other complex geometries, the conservative estimates produced from Rankine theory have commonly been used in engineering design.

2.1.3 Log Spiral (Terzaghi 1943)

Log spiral theory was developed by Terzaghi (1943) and is generally considered to be the best approximation of the mobilized shear failure mass (Duncan and Mokwa 2001; Rollins and Cole 2006). The initial segment of the failure plane was modeled by a log spiral curve followed by a linear Rankine segment as shown in Figure 2.2. This geometry allows the log spiral theory to better predict K_p for cases with steel, concrete, or wooden walls where $\delta > 0.4\varphi$ (Duncan and Mokwa 2001).

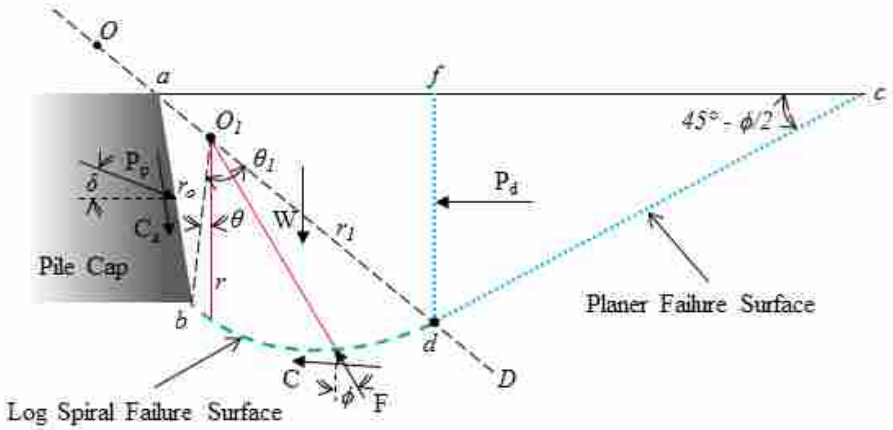

Figure 2.2. Log spiral failure plane geometry (Smith 2014).

Figure 2.3 shows a comparison of the failure surface geometries for a scenario with $\delta/\varphi=0.75$.

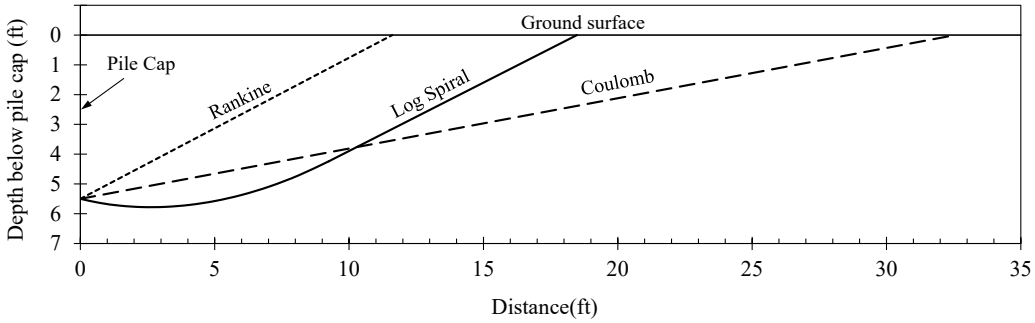

Figure 2.3. Comparison of failure geometries (Smith 2014).

2.2 Passive Force-Deflection Relationships

The ultimate passive resistance is typically mobilized with a deflection equal to 3 to 5% of the wall height; however, it is useful to know how much passive resistance might be available at smaller deflections. Large-scale tests have been performed to study these relationships (Cole and Rollins 2006, Lemnitzer et al. 2009). One important case where this resistance value is important is that of bridge abutment design. In order to design the abutment for lateral earthquake forces, the lateral resistance from the foundation system as well as the passive soil resistance must be known.

2.2.1 Caltrans Method

The Caltrans method approximates the nonlinear passive-force deflection relationship using a bilinear curve developed based on large-scale abutments tests performed at BYU, UC Davis, and UCLA. This relationship is presented in Figure 2.4.

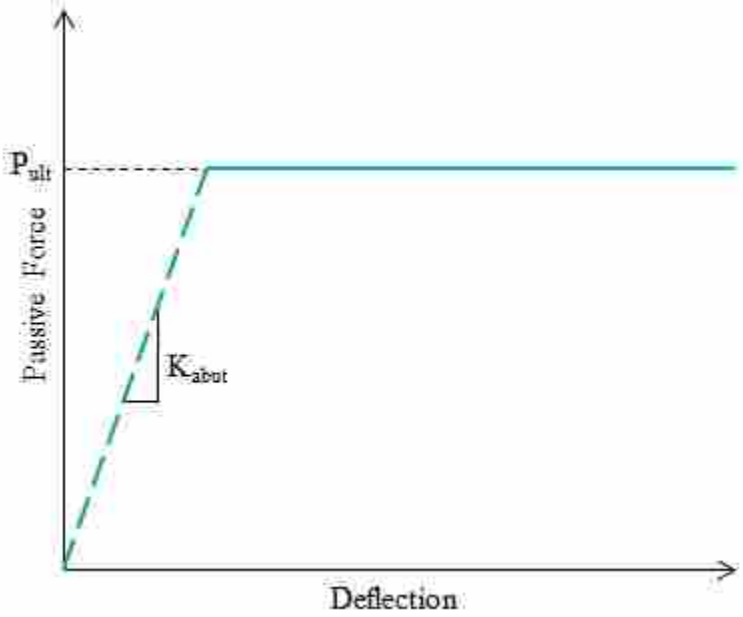

Figure 2.4 Caltrans bilinear passive-force deflection curve (Smith 2014).

The initial stiffness (K_i) is a function of the backfill type. If the backfill material meets Caltrans Standard Specifications, Equation (2-3) may be used to determine the initial stiffness; Equation ((2-4)) is used for backfill material not meeting specifications.

$$K_i = \frac{50\ \text{kip/in}}{\text{ft}} \tag{2-3}$$

$$K_i = \frac{25\ \text{kip/in}}{\text{ft}} \tag{2-4}$$

The initial stiffness is adjusted based on the abutment height and width and is represented by Equation (2-5).

$$K_{abut} = K_i \times w \times \frac{h}{5.5\text{ft}} \tag{2-5}$$

where,

K_i = initial stiffness

w = abutment width

h = abutment height

The ultimate passive force (P_{ult}) defined on the above curve is approximated using Equation (2-6).

$$P_{ult} = A_e \times 5.0\text{ksf} \times \frac{h}{5.5} \tag{2-6}$$

where,

A_e = Effective abutment area

h = abutment height

The Caltrans bilinear curve is limited by the method it uses for calculating initial stiffness. As shown above, the model uses a 50% reduction in initial stiffness from backfill meeting Caltrans Standard Specifications to backfill not meeting Caltrans Standard Specifications. This does not accurately predict initial stiffness for materials not meeting Caltrans Standard Specifications as there would be a gradual reduction in stiffness based on varying soil types..

2.2.2 AASHTO Method

The American Association of State Highways and Transportation Officials (AASHTO) uses a bilinear curve to approximate the passive force-deflection relationship. Rather than being defined by an initial stiffness, similar to the Caltrans approach, the AASHTO model is defined by $\frac{\Delta_{max}}{H}$ and P_{ult}. AASHTO recommends $\frac{\Delta_{max}}{H} = 0.05$ to be used for conservative design and P_{ult} be calculated using the log spiral method. The AASHTO design curve is illustrated in Figure 2.5.

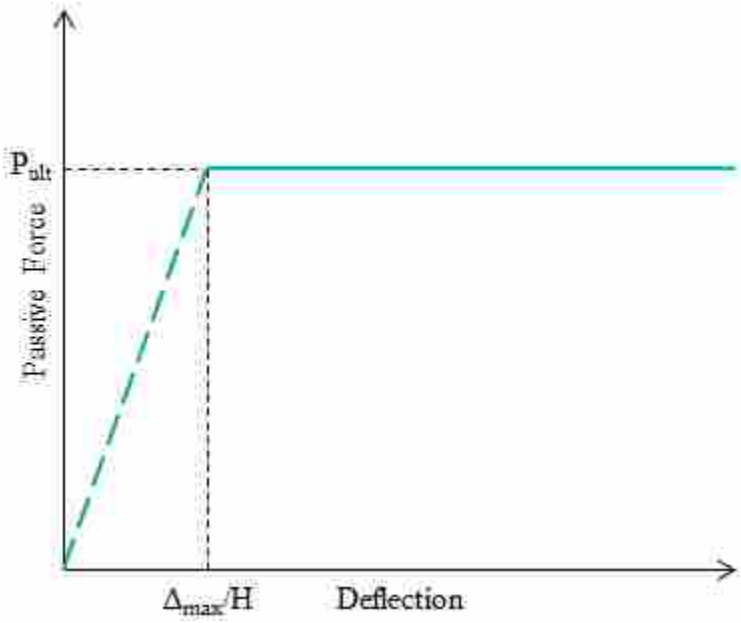

Figure 2.5 AASHTO bilinear passive force-deflection curve (Smith 2014).

2.2.3 Duncan and Mokwa (2001)

Duncan and Mokwa (2001) proposed a hyperbolic curve to represent the relationship between passive resistance and deflection. This relationship was developed based on a stress-strain hyperbolic curve created by Duncan and Chang (1970) and is shown in Figure 2.6. The initial slope for the curve was developed with an initial stiffness (K_{max}), and P_{ult} was computed using the log spiral method. This hyperbolic relationship is expressed in Equation (2-7).

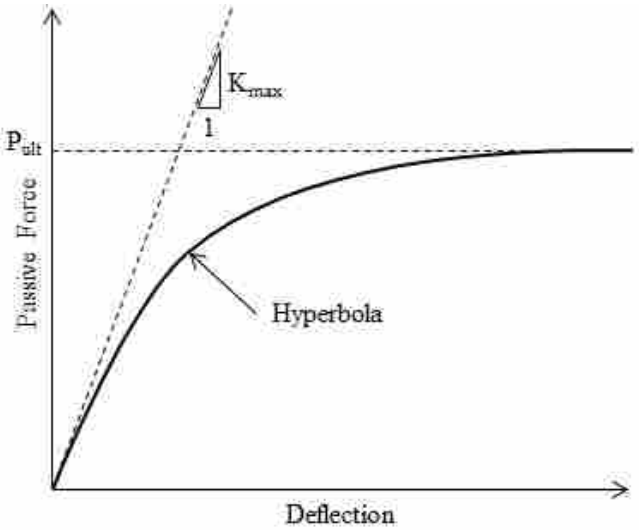

Figure 2.6. Hyperbolic passive force-deflection curve developed by Duncan and Mokwa (2001).

$$P=\frac{y}{\left[\frac{1}{K_{max}}+R_f\frac{y}{P_{ult}}\right]} \quad (2\text{-}7)$$

where,

y = Pile cap deflection

K_{max} = Maximum soil stiffness

R_f = Failure ratio = 0.75 to 0.95

P_{ult} = Maximum passive soil resistance

K_{max} is estimated using an approach developed by Douglas and Davis (1964), which uses Poisson's ratio (ν) and Young's Modulus (E) along with elastic theory. These values, along with the applied force (P), pile cap dimensions, and influence factors are used to compute the average deflection (y_{avg}). The maximum stiffness (K_{max}) is calculated by using Equation (2-8).

$$K_{max}=\frac{P}{y_{avg}} \tag{2-8}$$

The failure ratio is the ratio of the ultimate passive pressure over the asymptotic value of the passive resistance. When data from testing is not available, failure ratio (R_f) values ranging from 0.75 to 0.95 are suggested by Duncan and Chang (1970) for their stress-strain relationship. These values will also produce reasonable passive force-deflection curves. The asymptotic value of passive resistance is P_{ult} and is expressed in Equation ((2-9). Duncan and Mokwa (2001) developed a spreadsheet (PYCAP) to compute this parameter using the log spiral method.

$$P_{ult}=E_p bM \tag{2-9}$$

where,

E_p = Passive resistance per unit width

b = Pile cap width

M = Brinch Hansen 3D correction factor

The Brinch Hansen 3D correction factor essentially expands the width of the backfill providing resistance and its value ranges from 1 to 2 in PYCAP. Further details regarding PYCAP are provided by Duncan and Mokwa (2001).

The hyperbolic passive force-deflection curve developed by Duncan and Mokwa (2001) has been shown to more accurately estimate the continued increase in passive force with continued deflection when compared with the Caltrans and AASHTO methods (Cole and Rollins 2006). By using the Brinch Hansen 3D correction and the log spiral method, more accurate estimates of P_{ult} are obtained; consequently, better estimates of the ultimate passive resistance are obtained for both confined and unconfined soil backfills.

2.3 Finite Element Studies of Skewed and Non-Skewed Bridge Abutments

Two and three dimensional finite element studies have been performed in recent years on both skewed and non-skewed bridge abutments. Wilson and Elgamal (2010) and Nasr and Rollins (2010) both studied the effects of back wall deflection on passive force resistance. Shamsabadi et al. (2006) also studied the effects of skew angle on passive force-displacement curves. Guo (2015) used finite element analysis to validate the results of large-scale tests performed with the intent to study the effects of abutment skew angle and abutment geometry on passive force-deflection relationships. These studies will be summarized below.

2.3.1 Wilson and Elgamal (2010)

Wilson and Elgamal (2010) displaced a vertically reinforced concrete wall into a densely compacted backfill comprised of sand and 7% silt. The intent of this study was to observe the effects of the wall displacement on the passive force resistance and failure mechanism. The peak resistance was found to occur when the wall had horizontally displaced about 2.7-3.0% of the backfill height.

Soil strength parameters were determined by performing triaxial and direct shear tests on the backfill material. These parameters were then used as inputs in a Plaxis 2D finite element model that was calibrated using physical test data. This finite element model produced load-deflection results within 95% of the peak resistance. This model was then used to generate passive force-deflection curves for varying engineering applications and was used to study the relationship between passive resistance and vertically restrained walls (abutments supported on deep foundations). These studies showed that the passive resistance significantly increased with a vertically restrained wall.

2.3.2 Nasr and Rollins (2010)

Nasr and Rollins (2010) used Plaxis 2D to simulate plane strain passive force behavior of previous full scale lateral load tests on pile caps with limited width dense granular backfill. The intent of the study was to develop equations to help predict the passive resistance as a function of dense gravel thickness and soil friction angle. Analytical results from PYCAP (Duncan and Mokwa 2001) and ABUTMENT (Shamsabadi et al. 2007) were also used to calibrate these models. Table 2.2 shows the parameters used by Nasr and Rollins (2010).

Table 2.2. Input Parameters for Hardening Soil Model as Used by Nasr and Rollins (2010)

Parameter	*Loose Sand*	*Dense Gravel*	*Unit*
Friction Angle, ϕ	27.7	42.0	Degrees
Cohesion, c_{ref}	0.5 (10.44)	1.9 (39.68)	kPa (lb/ft^2)
Dilation Angle, ψ	0	12	Degrees
Soil Unit Weight	17.3 (110.1)	22.1 (140.7)	kN/m^3 (lb/ft^3)]
Secant Stiffness Modulus E_{50}^{ref}	15.8 (330)	81.4 (1,700)	MPa (kip/ft^2)]
Reference Stress, P_{ref}	100 (2089)	100 (2089)	kPa (lb/ft^2)

Poisson's Ratio, ν_{ur}	0.2	0.2	—
Interface Friction Angle, δ	0.75ϕ	0.75ϕ	Degrees
Interface Strength Reduction Factor, R_{inter}	0.7	0.7	—

Once calibrated, the model was used in parametric studies to investigate the effects of pile cap geometry and soil backfill parameters. These results were then compared with tests performed by Rollins et al. (2010) to determine the effects of varying parameters. It was found that the friction angle of the dense gravel backfill would alter the passive resistance dramatically, while unit weight, cohesion, and stiffness did not have as much influence. This means that a soil with a lower unit weight, cohesion or stiffness could be used as long the friction angle remains high and the width of the dense layer is greater than about 50% of the wall height.

2.3.3 Shamsabadi et al. (2006)

Shamsabadi et al. (2006) used Plaxis 3D to develop passive force-deflection curves for skew angles of 0°, 30°, 45°, and 60°. The model consisted of a 75-foot wide by 5½-foot tall abutment containing longitudinal wingwalls and a silty sand backfill. The model's soil parameters are presented in Table 2.3. This study showed that passive force resistance decreases as the skew angle increases. A plot of these results is shown in Figure 2.7.

Table 2.3 Backfill Properties (Shamsabadi 2006)

Soil Type	ɣ, pcf [kN/m^3]	ϕ	c, psf [kPa]	δ
Silty Sand	119.7 [18.8]	34°	522 [25]	23°

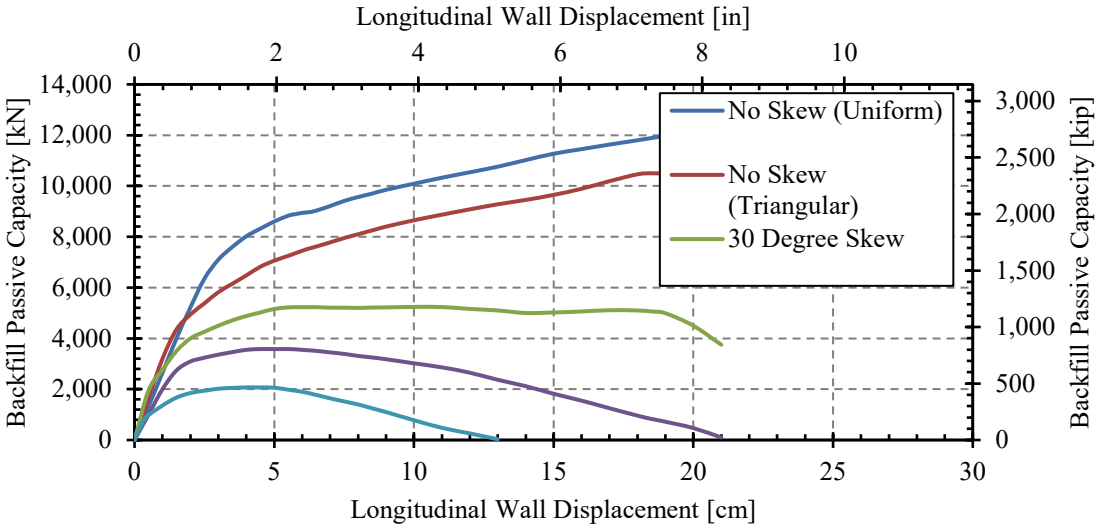

Figure 2.7. Passive force-deflection curves for varying skew angles (Shamsabadi et al. 2006).

Shamsabadi et al. suggest that the effect of the skew angle on the development of passive pressure should be studied further. In addition, the authors indicated that the effect of the wingwalls on the development of passive pressure is small and would likely increase as abutment width decreases.

2.3.4 Guo (2015)

Using Plaxis 3D, Guo (2015) created models to simulate skewed abutment displacements into densely compacted granular fill. This involved modeling the geometry, soil backfill strength parameters, and calibrating the model using data from large scale tests performed by Rollins et al. (2010). A more detailed explanation of the modelling process will be presented later in Chapter 4.

Table 2.4 provides a summary of the soil strength parameters used in the model. These parameters were derived from lab and fieldwork, as well as using Plaxis 3D default values. Table 2.5 displays the structural properties used to model the pile cap.

Table 2.4. Plaxis Model Parameters for Hardening Soil Model

(Guo 2015)

Symbol	Parameter	Value	Default Units
	Failure parameters (same as for Mohr-Coulomb model)		
c	(Effective) cohesion	85	[lb/ft^2]
ϕ	(Effective) angle of internal friction	40	[°]
δ	Wall friction angle	30	[°]
ψ	Angle of dilatancy	15	[°]
R_{inter}	Interface Friction Ratio	0.6881	
	Basic soil stiffness parameters		
γ_{unsat}	Unsaturated Unit Weight	116.5	[lb/ft^3]
γ_{sat}	Saturated Unit Weight	120	[lb/ft^3]
E_{50}^{ref}	Secant stiffness in standard drained triaxial test	1.920E6	[lb/ft^2]
E_{oed}^{ref}	Tangent stiffness for primary oedometer loading	1.920E6	[lb/ft^2]
E_{ur}^{ref}	Unloading/reloading stiffness (default $E_{ur}^{ref} = 3E_{50}^{ref}$)	4.800E6	[lb/ft^2]
m	Power for stress-level dependency of stiffness	0.5	[-]
	Advanced parameters		
ν_{ur}	Poisson's ratio for unloading-reloading (default $\nu_{ur} = 0.2$)	0.2	[-]
p^{ref}	Reference stress for stiffness (default $p^{ref} = 100$ kN/m^2)	2089	[lb/ft^2]
K_0^{nc}	K_0-value for normal consolidation (default $K_0^{nc} = 1 - \sin\phi$)	0.3601	[-]
R_f	Failure ratio q_f/q_a (default $R_f = 0.9$)	0.9	[-]
σ_{tensio}	Tensile strength (default $\sigma_{tension} = 0$ stress units)	0	[lb/ft^2]
c_{inc}	Incremental increase in cohesion with depth (default $c_{inc} = 0$)	0	[lb/ft^2]
	Alternative soil stiffness parameters		
C_c	Compression index	3.865E-3	[-]

C_s	Swelling index or reloading index	1.392E-3	[-]
e_{init}	Initial void ratio	0.5450	[-]

Table 2.5. Plate Element Parameters for Pile Cap (Guo 2015)

Property	Value	Units
Plate Thickness, d	15	ft
Unit Weight, γ	150	lbf/ft^3
Young's Modulus, E	635.8E6	lbf/ft^2
Poisson's Ratio, ν	0.30	–
Shear Modulus, G	264.9E6	lbf/ft^2

A three-dimensional mesh was generated and the Hardening soil material model was used to run the model and calculate results. Passive force-displacement curves generated by the model were compared to field test results for the zero skew tests, and adjustments were made to soil strength parameters until reasonable agreement was found. Using these same soil properties, analyses were then performed for each of the different abutment skew geometries tested in the field. Agreement with measured passive force-deflection curves was generally reasonable except that the model underestimated skew effects for the 15 degree skew.

After the model calibration, the models were used to study the effects of varying parameters such as the soil friction angle, wall friction angle, soil dilatancy angle, soil stiffness, and restraint in the transverse direction. After studying these effects the authors concluded that shear force is increased and shear resistance is decreased as the skew angle increases. Additionally, the authors determined that passive force resistance was a function of soil friction angle, soil dilatancy angle, and soil stiffness. Increasing each of these parameters increased the passive force.

2.4 Relevant Field and Lab Tests

Multiple studies have been performed on skewed bridge abutments. The following sections are summaries of these investigations as they relate to this study.

2.4.1 Jessee (2012)

Jessee (2012) studied the effects of increasing the skew angle on passive soil resistance and found that as the skew angle increased, the passive resistance decreased. Small-scale laboratory tests were performed by displacing a 4.1-ft (1.26-m) wide by 2-ft (0.61-m) tall concrete wall into a dense sand backfill. Tests were performed at skew angles of 0°, 15°, 30°, and 45°. The test configuration is shown in Figure 2.8.

Figure 2.8. Small-scale lab test configuration (Jessee 2012).

The passive force-deflection curves for the 9 small-scale laboratory tests are presented in Figure 2.9. Similar to the finite element study by Shamsabadi et al. (2006), the passive force is significantly reduced as the skew angle increases.

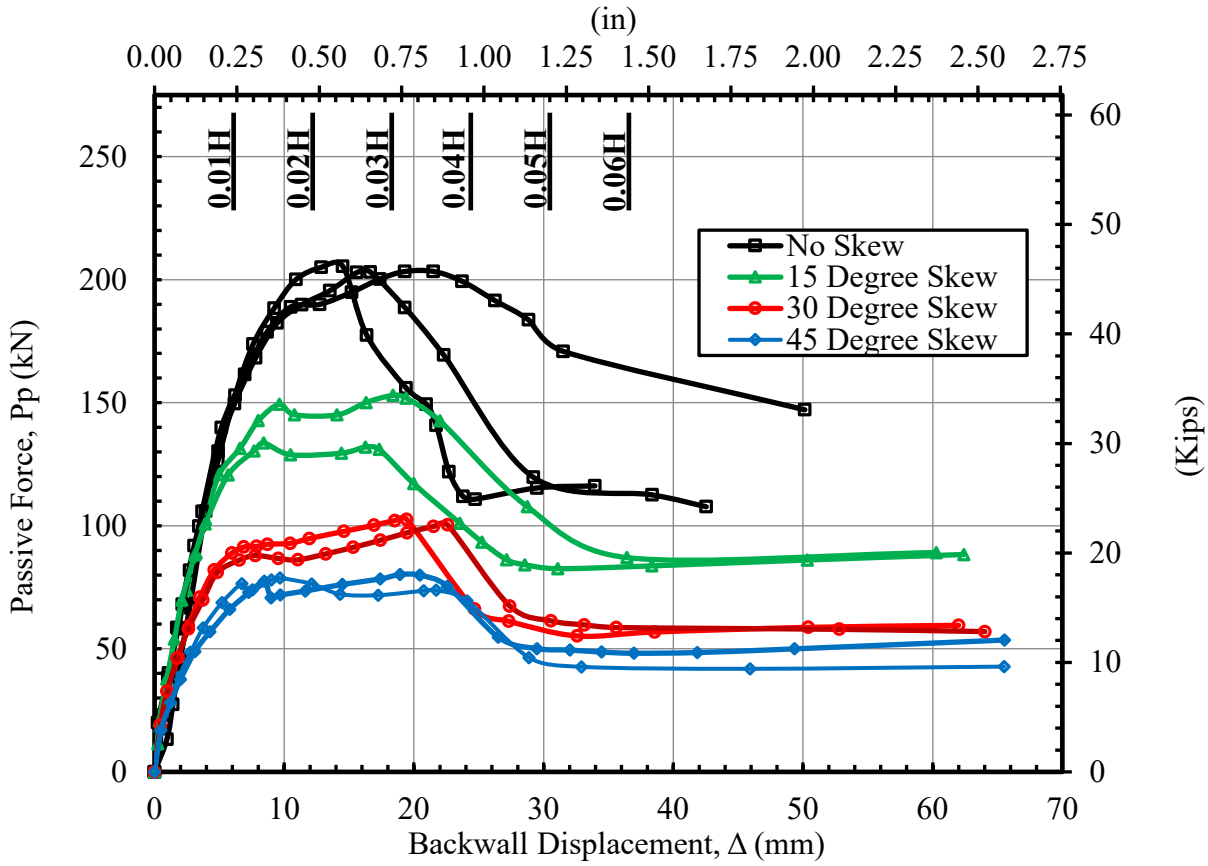

Figure 2.9. Passive force-deflection curves for small-scale lab testing (Jessee 2012).

Jessee (2012) used the resulting data to develop a reduction factor (R_{skew}) that is a function of the skew angle (θ). Equation (2-10) is used to compute R_{skew}. In addition, the reduction factor is presented graphically in Figure 2.10 along with data from the small-scale lab testing and from the study by Shamsabadi et al. (2006).

$$R_{skew} = \frac{P_{p-skew}}{P_{p-no\ skew}} = 8 * 10^{-5}\theta^2 - 0.018\theta + 1 \qquad (2\text{-}10)$$

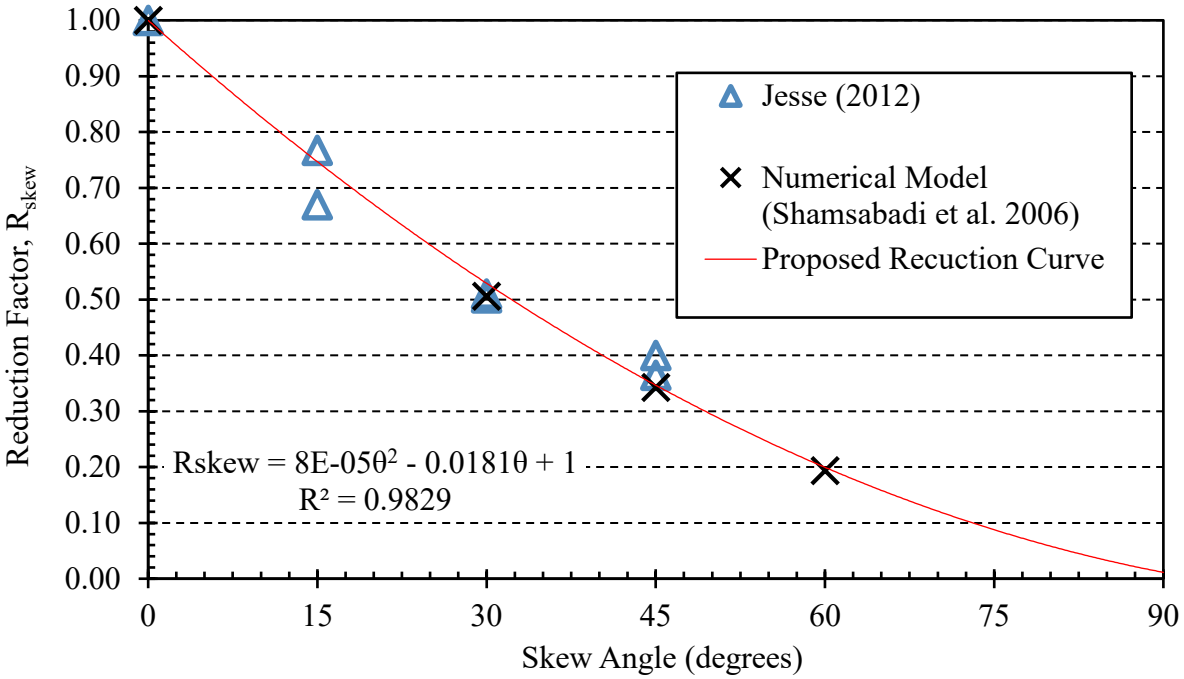

Figure 2.10. Proposed passive force reduction factor as a function of skew angle (After Jessee 2012).

The reduced-scale study shows remarkable agreement with the finite element studies performed by Shamsabadi et al. (2006) and supports the conclusion that as the skew angle increases, the passive resistance of the soil will decrease (See 2.3.3).

2.4.2 Smith (2014)

Smith (2014) performed large-scale tests on skewed bridge abutments containing reinforced concrete wingwalls. Similar to Jessee (2012), these tests also found that there is a reduction of passive resistance based on the skew angle. However, as shown in Figure 2.11, there appears to be some inconsistences in the data for the 45° skew reduction factor. The reduction factor is under predicted in the field tests performed by Smith.

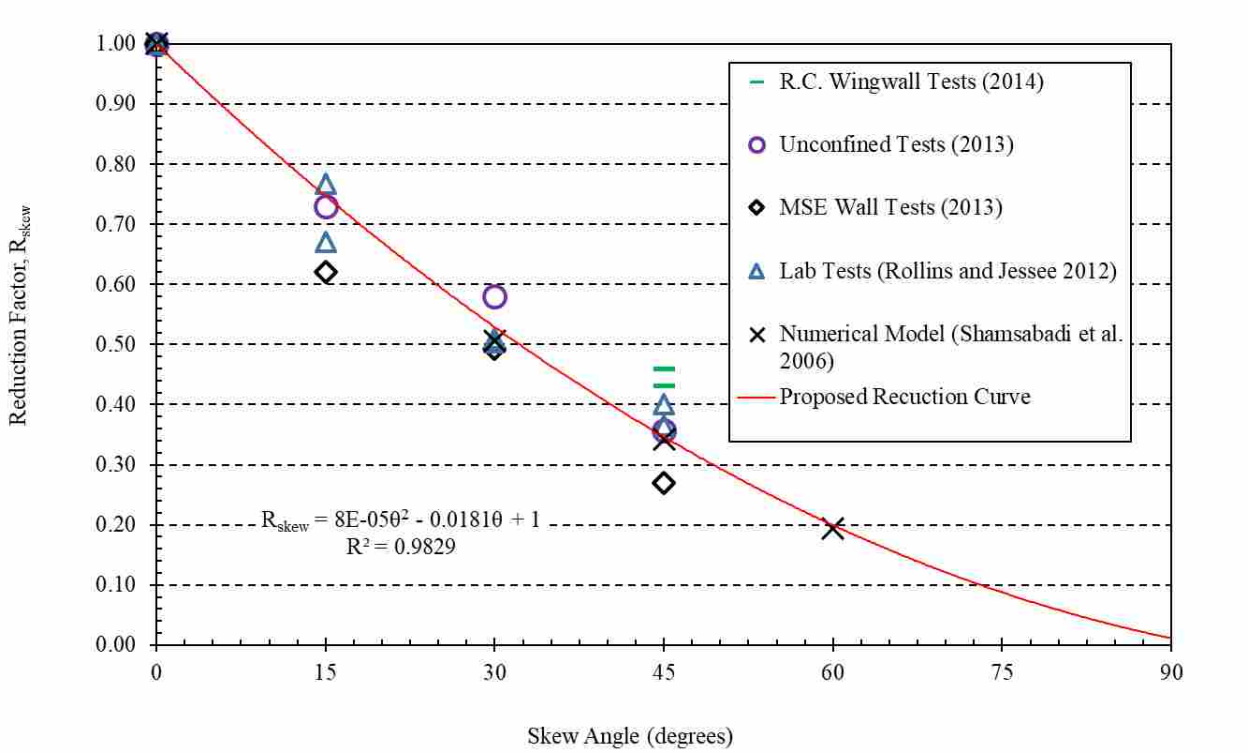

Figure 2.11 Reduction factor, R_{skew} (passive force for a given skew angle normalized to non-skewed passive force) plotted versus skew angle based on lab tests (Jessee 2012), numerical analyses (Shamsabadi et al. 2006) and results from field tests (Smith 2014).

The field tests performed by Smith are the basis for this study and more field test details and results of the study will be presented further in Chapters 3 and 5, respectively.

2.5 Literature Review Summary

Multiple theories have been developed to approximate passive earth pressures. Coulomb's theory tends to over predict passive earth pressures while Rankine theory tends to under predict them. Log Spiral theory is generally considered the best approximation of passive earth pressures.

Caltrans and AASHTO have developed two methods of relating the ultimate passive force to the deflection of the abutment. The Caltrans method is limited in the way it estimates the initial stiffness based on the backfill type while the AASHTO method uses the log spiral method to more

accurately predict ultimate passive force. In addition, Duncan and Mokwa (2001) developed a hyperbolic relationship using both an initial stiffness and ultimate passive force, which is essentially a mix of the Caltrans and AASHTO's method.

Two and three-dimensional finite element studies of skewed and non-skewed abutments have been performed to study the relationship between passive force, deflection, and skew angle. Wilson and Elgamal (2010) determined that the passive resistance significantly increased with a vertically restrained wall. Nasr and Rollins (2010) found that the friction angle of the backfill would significantly affect the passive resistance, while unit weight, cohesion, and stiffness did not have as much influence. The finite element study performed by Shamsabadi et al. (2006) showed that passive force resistance decreases as skew angle increases and that the influence of wingwalls is small but will increase as the size of the abutment decreases. Guo (2015) concluded that shear force is increased and shear resistance is decreased as the skew angle increases. They also found that passive force resistance was a function of the soil friction angle, soil dilatancy angle, and soil stiffness.

Laboratory and field studies have been performed by Jessee (2012) and Smith (2014). Jessee (2012) developed a reduction factor (R_{skew}) based on skew angle (θ). This reduction factor proved to be in good agreement with finite element studies performed by Shamsabadi et al (2006). Smith (2014) performed large field tests on skewed and non-skewed abutments and the results indicate that there is a reduction in passive force resistance with increasing skew angle. However, the field tests under predicted R_{skew} for the 45° skew case and is inconsistent with the reduction factors proposed by Jessee (2012).

3 FIELD TESTING

3.1 Site Description

The large-scale field test performed by Smith (2014) was located at a site about 1,000 ft north of the air traffic control tower at the Salt Lake City International Airport. Additional tests have been performed at this location by Rollins and Sparks (2002), Johnson (2003), Christensen (2006), Taylor (2006), and Rollins et al. (2010). The site has been ideal for performing these tests due to the available soil stratigraphic information, site security, absence of overhead obstructions, and the ease of access for heavy equipment. An aerial view of the site relative to the airport air traffic control tower is shown in Figure 3.1.

Figure 3.1. Test site near air traffic control tower at Salt Lake International Airport.

3.2 Geotechnical Site Characterization

Various methods of subsurface investigation have been performed at the site in order to effectively characterize the soil. Tests that have been performed over the years include drilled holes (DH), hand augers (H), pressuremeter tests (PMT), cone penetration tests (CPT) and dynamic cone penetration tests (DCPT). The location of the tests performed around the site are diagramed in Figure 3.2. The pile cap for this study is located at CPT-06-M. The idealized soil profile of this test location is presented below in Figure 3.3 and Figure 3.4.

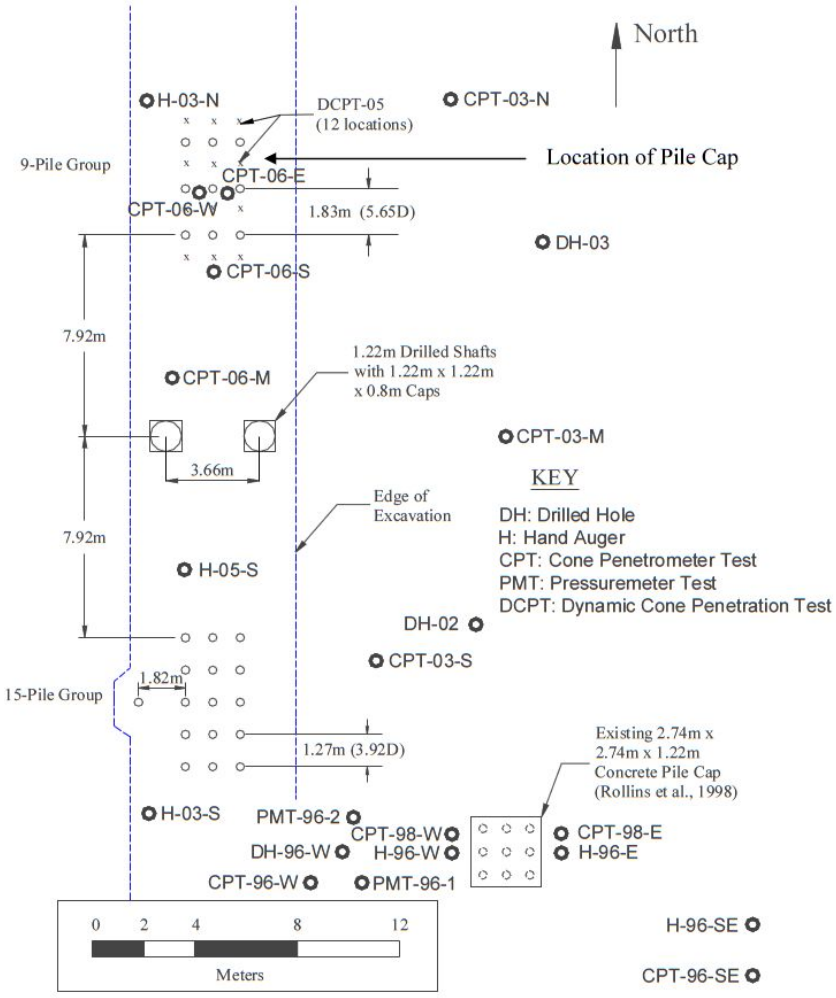

Figure 3.2. Test history at Salt Lake City airport site (Rollins et al. 2010).

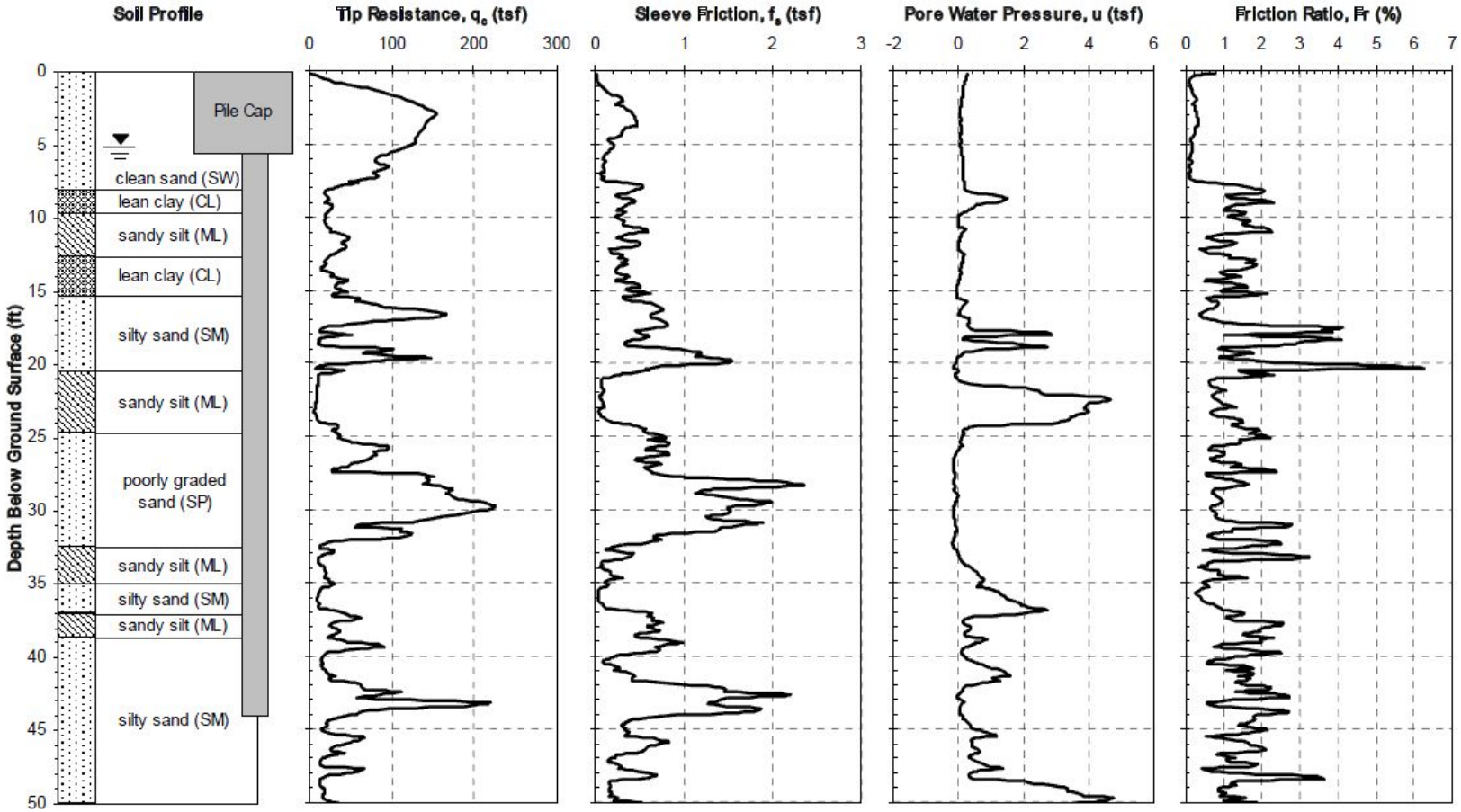

Figure 3.3 Idealized Soil Profile From CPT Test (Rollins et al. 2010)

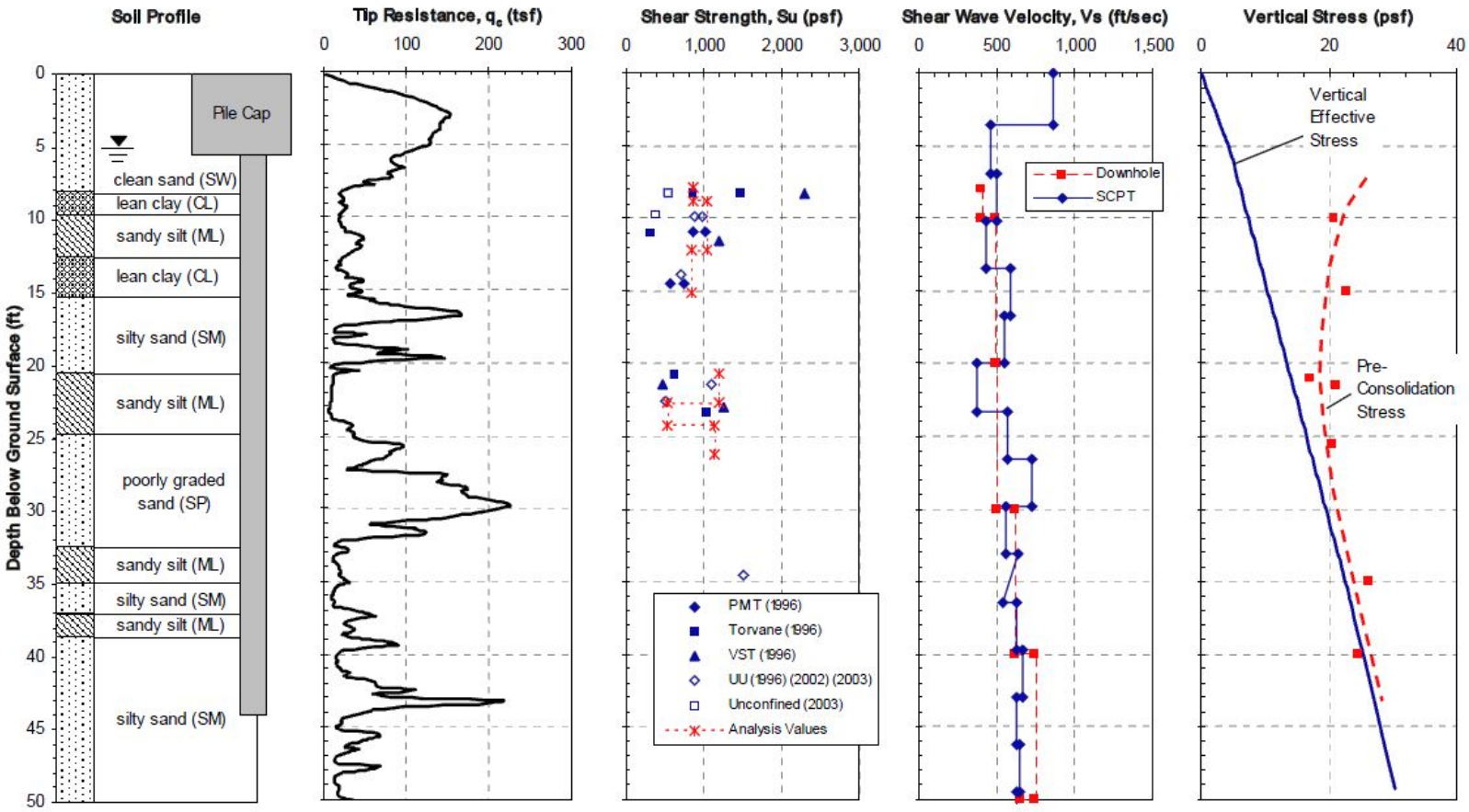

Figure 3.4. Idealized Soil Profile Developed From CPT Test Data (Rollins et al 2010)

Details of the site and its subsurface characterization are available elsewhere (Christensen 2006; Rollins et al. 2010; Strassburg 2010).

3.3 Testing Layout

The two large-scale tests conducted by Smith (2014) were performed on 0° and 45° skewed abutments containing monolithically attached reinforced concrete wingwalls as shown in Fig. 3.5. These specimens, were displaced into the soil backfill by two 600 kip hydraulic actuators. These actuators reacted against a drilled shaft and sheet pile wall foundation system. The pile cap and 15° skew concrete wedge were already available due to prior testing. The 45° skew abutment was assembled by adding an additional wedge to the existing configuration. Reinforced concrete wingwalls were attached to the abutment to simulate a monolithic abutment. Basic details of each component are presented below. Additional information can be obtained from Smith (2014).

3.3.1 Reaction Foundation

As shown in Fig. 3.5, the reaction foundation was composed of two reinforced concrete drilled shafts that were 4 feet in diameter and spaced 12 feet apart, center to center, along an east-west line. A sheet pile wall was attached to span the north side of the drilled shafts and two additional 5-foot by 28-foot I-beams were added to span the north and south sides of the system to increase the rigidity. These were added with the strong axis oriented in the north-south direction.

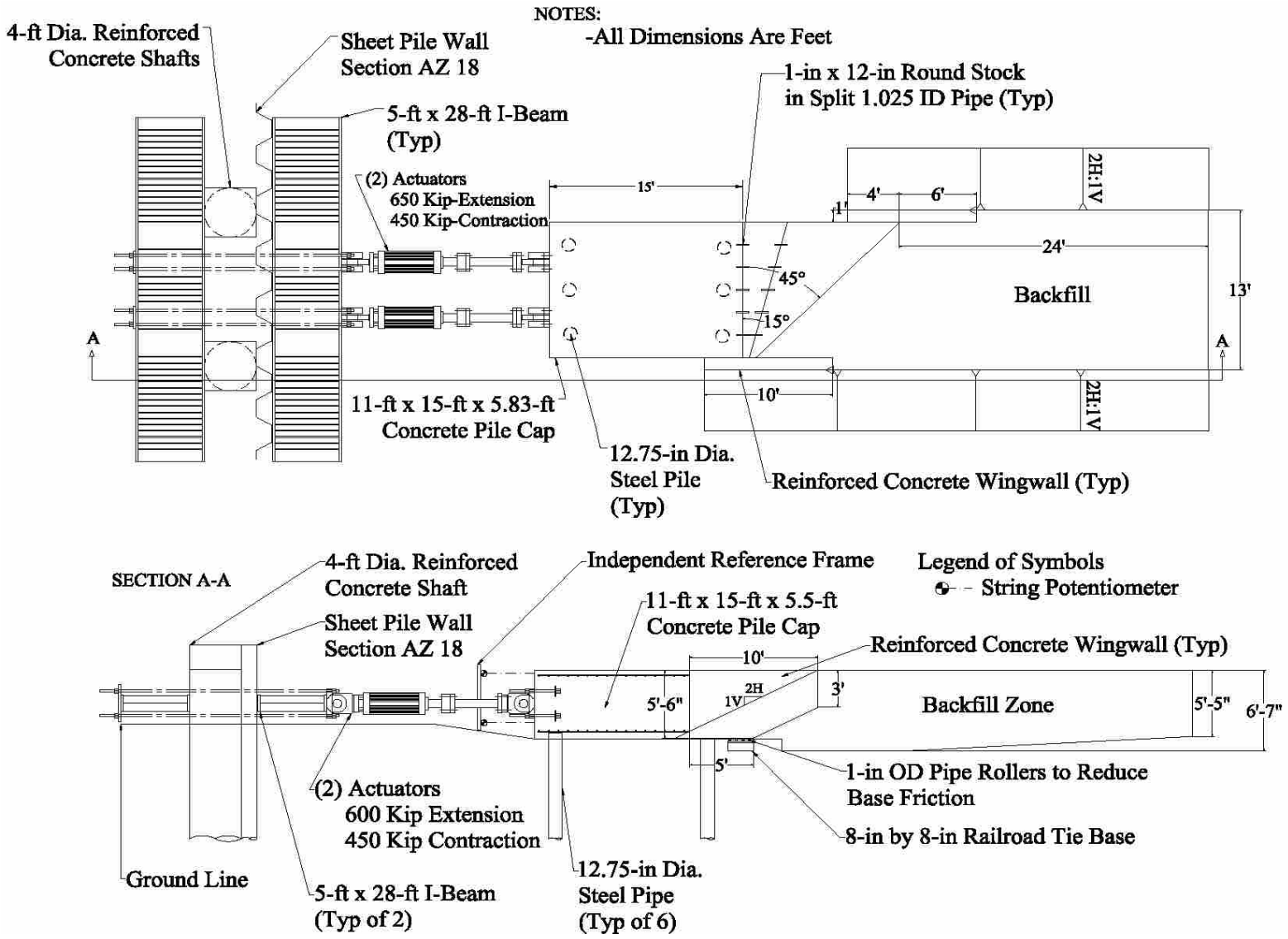

Figure 3.5. Schematic for reaction foundation (Smith 2014).

3.3.2 Piles and Pile Cap

The southern edge of the pile cap was located 16.4 feet north of the reaction foundation. The cap extended 15 feet in length to the north and was 11 feet wide and 5.5 feet tall. The pile cap was supported by a group of 6 steel pipe piles.

3.3.3 Concrete Wedges

In order to test the 45° skew abutment, two different concrete wedges were combined and attached to the pile cap face. A newly poured concrete wedge was attached to the existing 15° wedge to form the 45° skew. The wedge was placed on top of steel rollers as shown in Figure 3.6 to reduce friction resistance along the base of the wedge soil interface. This allowed for the study to focus on the passive resistance of the soil backfill.

Figure 3.6. Steel rollers used to reduce friction at the base of the wedge sections.

3.3.4 Reinforced Concrete Wingwalls

The reinforced concrete wingwalls and the connections used for this study were designed as part of the study performed by Smith (2014). The wingwalls were 1-ft-thick, 5.5-ft-high, and 10-ft-long. The bottom edge of the wingwalls were parallel with the bottom of the pile cap and wedges for the first 5 feet, after which the wingwalls sloped up at a 2H:1V slope. This resulted in the tapered end of the wingwalls being 3 feet high. The first 4 feet of the wingwalls were used to connect the wingwalls to the abutment and the remaining 6 feet of the wingwalls extended into the backfill. The design of the wingwall used 4,000 psi concrete and is shown in Figure 3.7.

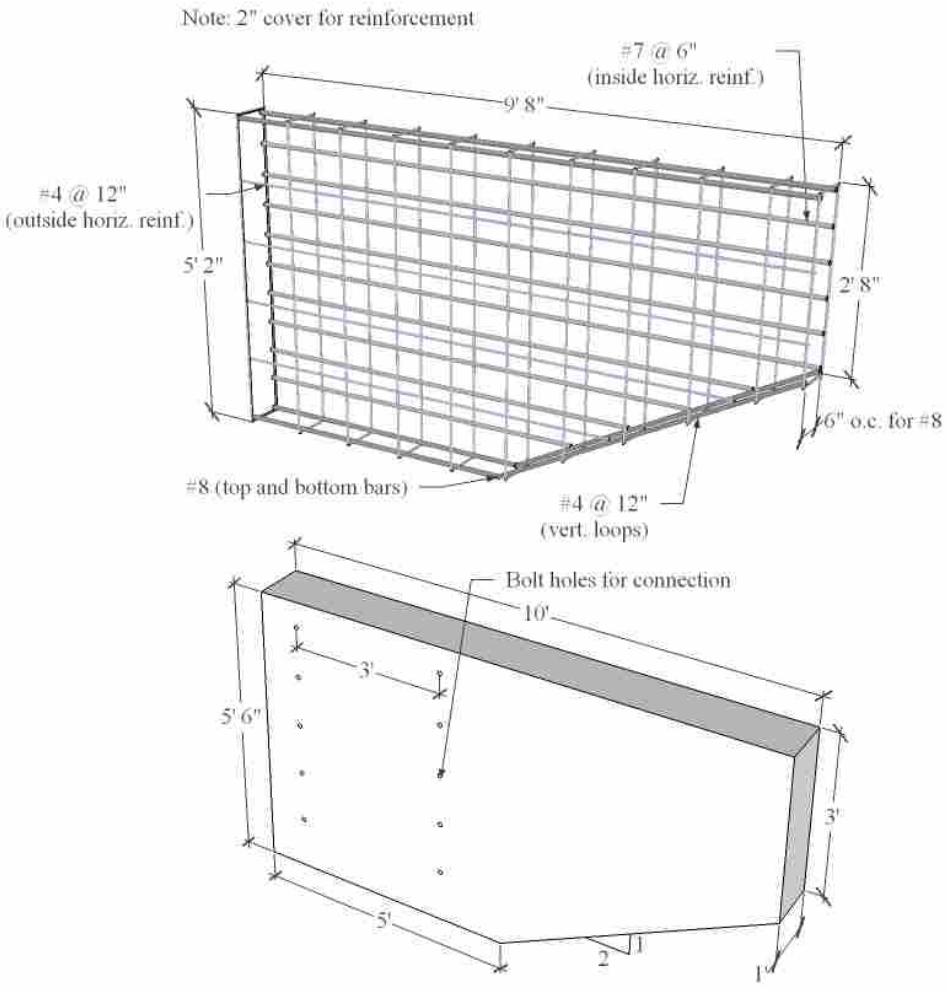

Figure 3.7. Wingwall design used by Smith (2014).

3.3.5 Loading Apparatus

The abutment was loaded into the backfill by placing two MTS actuators between the pile cap and the reaction foundation as shown in Figure 3.8. The actuators were oriented in the north-south direction and were capable of exerting a compression force of 600 kips and a tension force of 450 kips.

Figure 3.8. Two MTS actuators connecting the pile cap and reaction foundation.

3.3.6 Backfill Zone

The backfill zone extended 5 feet beyond either side of the abutment in the transverse direction and 24 feet beyond the abutment backwall in the longitudinal direction. On either side of

the abutment, the backfill sloped downward at a 2H:1V slope over the 5 feet. The depth of the backfill extended about 1 foot beneath the bottom of the abutment in order to fully encompass a potential log-spiral failure surface. The backfill was compacted to 95% of the modified Proctor to simulate field conditions. Depictions of the 0° and 45° skew abutments with their compacted backfill are shown in Figure 3.9 and Figure 3.10.

Figure 3.9. Compacted backfill for the non-skewed abutment.

Figure 3.10. Compacted backfill for 45° skewed abutment.

3.4 Geotechnical Backfill Characterization

This section provides a summary of the data used to characterize the backfill soil, primarily the soil's gradation, relative compaction, relative density, and strength parameters.

3.4.1 Backfill Soil and Compaction

Approximately 250 tons of fill classified as a poorly graded sand (SP in the Unified Soil Classification System, and A-1-a in the AASHTO Classification System) was used for this study. The soil's moisture content was 7%. Details of the pre-test and post-test gradations are provided in Smith (2014). The grain-size distribution of this sandy backfill mostly fell within the limits of a washed concrete sand (ASTM C33).

3.4.2 Soil Strength Parameters

The soil strength parameters of cohesion (c) and friction angle (φ) were determined using direct shear tests performed in accordance with ASTM D3080—Standard Test Method for Direct Shear Test of Soils Under Consolidated Drained Conditions. These tests were performed in the Brigham Young University (BYU) soils laboratory (Franke 2013; Marsh 2013).

To accurately simulate field conditions during direct shear testing, representative normal stresses of 4.1, 8.2, 16.3, and 24.5 psi were selected. Tests were performed both at dry conditions as well as at the compaction moisture content. The resulting values for cohesion (c) and friction angle (φ) from the moist direct shear test are presented below in Table 3.1.

Table 3.1. Soil Strength Parameters (Smith 2014)

Source of Test Result	Peak		Ultimate	
	ϕ (deg)	c (psf) [kPa]	ϕ (deg)	c (psf) [kPa]
Direct Shear (moist)	42.7	92.9 [4.45]	41.4	78.8 [3.77]
Direct Shear (moist, cohesionless)	43.8	0	42.3	0

For comparison, an in-situ direct shear test was performed on an undisturbed sample at the site. The in-situ test results were comparable to those of the laboratory direct shear tests with an apparent cohesion of $c = 191$ psf and $\phi = 41.9°$.

3.5 Instrumentation and Measuring

This section provides a brief summary of the instrumentation that was used to collect data from the large-scale testing.

3.5.1 Abutment Displacement

The movement of the abutment was monitored in both the longitudinal and transverse directions. Four string potentiometers were used to monitor the abutment's longitudinal displacement. This was done by attaching a potentiometer to each corner on the face of the abutment connected to the actuators. Displacement was then measured from an independent reference frame between the foundation and the pile cap.

The transverse displacement was measured by using inclinometers and shape accelerometer arrays. Measurements were taken at the center piles of the pile group. In addition, a total station was used to record the transverse displacement at each of the four corners of the top of the pile cap.

3.5.2 Passive Force Resistance

The passive resistance (P_p) of the soil backfill was measured through the use of pressure transducers located in the actuators and was computed using Equations (3-1) and (3-2).

$$\boldsymbol{P_L = P_{total} - P_{baseline}} \quad (3\text{-}1)$$

$$\boldsymbol{P_p = P_L cos\theta} \quad (3\text{-}2)$$

where P_{total} = the total amount of force required to displace the abutment into the backfill, $P_{baseline}$ = the total amount of force required to displace the abutment with no backfill, and θ = the skew angle. The baseline resistance was attributed to the lateral resistance provided by the pile group.

The 45° skew test also incorporated six Geokon® pressure cells to determine the distribution of the passive pressure along the width of the pile cap. This also allowed for a

comparison to be made between the resistance obtained from the transducers and the resistance measured by the pressure cells. The layout of the pressure cells is shown in Figure 3.11.

Figure 3.11. Geokon® pressure cell layout for 45° skew test (Smith 2014).

3.5.3 Pile Deflection

The deflection of the center piles in the pile group, in both the longitudinal and transverse direction were measured using inclinometers and shape accelerometer arrays (SAAR). The inclinometers and shape arrays were installed into the center of the piles during construction. Further detail for this instrumentation is provided in Smith (2014).

3.5.4 Backfill Heave and Displacements

The backfill heave, transverse displacement, and longitudinal displacement were measured using a total station. Prior to testing, grids were spray-painted onto the backfill surface to provide

a reference. The grids were parallel and perpendicular to the abutment skew and were typically spaced 2 feet apart. The grid was refined to a 1-ft spacing within 6-ft of the abutment for the 0° skew test. Elevation, transverse, and longitudinal measurements were taken before and after each test. The instrumentation for both the 0° and 45° skew tests are shown in Figure 3.12 and Figure 3.13. String potentiometers were also used to monitor backfill surface displacement.

Figure 3.12. Spray-painted grid for 0° skew test (Smith 2014).

Figure 3.13. Spray-painted grid for 45° skew (Smith 2014).

3.5.5 Shear Failure Surface

Columns of red-dyed sand were compacted into the backfill zone to aid in determining the shear failure surface. This was achieved by using hand-augers to bore 3-in holes which were then re-compacted with the red-dyed sand. Within 8-ft of the abutment backwall holes were bored to a

depth of 6-ft. As the distance from the backwall increased the depth of the borings was reduced in anticipation of a shallower failure surface.

3.5.6 Wingwall Instrumentation

Strain gages were bonded to the reinforcing bars within the reinforced concrete wingwalls. They were placed at locations 3-ft and 6-ft from the tapered end and were spaced vertically with 12-in spacing. This spacing is shown in further detail in Figure 3.14. The strain was continuously recorded during testing and the collected data was used to determine the moment and pressure at these locations. The gages located 6-ft from the tapered end were specifically designed to produce the pressure and moment at the wingwall-abutment interface. In addition to these strain gages, two more Geokon® pressure cells were used per wingwall. These pressure cells were installed to help determine the pressure distribution across the wingwall and were located as shown in Figure 3.15.

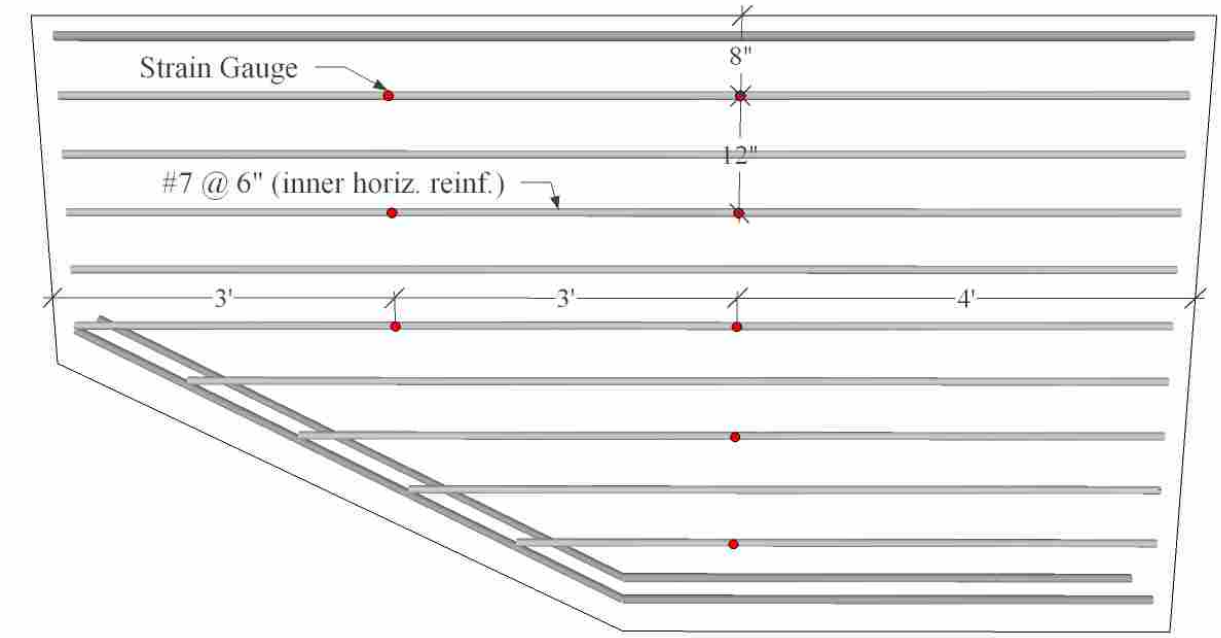

Figure 3.14. Wingwall strain gage locations (Smith 2014).

Figure 3.15. Geokon® pressure cell distribution along each wingwall (Smith 2014).

The transverse deflection of the wingwalls was measured using additional string potentiometers. Figure 3.16 shows four potentiometers that were placed 1-in, 36-in, 76-in, and 93-in from the tapered end along the top, outer edge of the wingwall to measure the deflection.

Figure 3.16. String potentiometers measuring lateral deflection (Smith 2014).

3.6 Testing Procedure

In order to attach the reinforced concrete wingwalls and place the soil backfill, the soil on the sides of the abutment and in the backfill zone from previous testing had to be excavated. Once this was completed the wingwalls were attached and the abutment was displaced without backfill to measure the baseline resistance. The backfill was then placed along with a typical side slope of 2H:1V. Prior to displacing the abutment into the backfill, orange grids were spray-painted onto the backfill surface as described in section 3.5.4 and the coordinates of each of the grid intersections were recorded.

After these measurements were taken, the abutment was displaced longitudinally into the backfill at a rate of 0.05 in/minute up to a maximum displacement of 3 to 3.75 inches. At each displacement interval of 0.25 in., the loading was held constant to allow for collection of load-displacement data and to record the appearance of surface cracks in the backfill. In addition, data from pile deflection, strain in the wingwalls, and pressure on the abutment backwall and wingwalls were continuously recorded. Upon the completion of the test, final coordinates were measured at each grid intersection.

This same process was repeated for each test, save a few small differences as previously noted in the test setup. Two pumps on either side of the abutment ran constantly through the duration of the testing to keep the water table at least 1 to 2 ft below the bottom of the abutment.

4 NUMERICAL MODELING

Numerical modeling for this study was performed using a finite element program called Plaxis 3D. Plaxis 3D is commonly used to consider non-linear properties of soil and is also used for soil-structure applications. Within Plaxis 3D there are two major subprograms, Plaxis 3D Input and Plaxis 3D Output. The Plaxis 3D Input program is used to input boundary conditions, create geometric elements, assign soil and material parameters, generate meshes, and define calculation phases. The Plaxis 3D Output program is used primarily to view calculation results and present data both numerically as well as graphically.

This chapter will outline the basic procedures and methods used in Plaxis 3D to create, run, and calibrate the finite element models. It will also include a description of the calibrated models.

4.1 Geometry Modeling

The first steps in creating a conceptual model in Plaxis 3D are to set the boundary conditions, assign soil stratigraphy, and create soil and structural elements to best match field conditions. Boundary conditions are set to a distance where the calculation will not be influenced by the model extent. The soil stratigraphy and water table elevation for the site are imported into Plaxis 3D by creating a “borehole”. The use of a single borehole to characterize the site causes Plaxis to assume the stratigraphy is constant throughout the model. This assumption is accurate for this series of tests due to the relatively small area the model represents.

Once the boundary conditions and soil stratigraphy have been assigned, soil and structural elements are defined by creating “surfaces” (soil elements) and “plates” (structural elements) and assigning strength parameters to the respective material. The required soil parameters depended on the type of soil constitutive model selected (Hardening Soil Model, Mohr-Coulomb Model, Cam-Clay Model, etc.). The properties required for structural elements are independent of the model type, and properties such as plate thickness, Young’s Modulus, Poisson’s ratio and others were selected. Before generating the mesh, it was necessary to assign loads or prescribed displacements (only prescribed displacements for this study) for the model elements.

Generation of the 3-dimensional tetrahedral mesh can be performed at different densities thus producing more accurate calculation results. The mesh is also able to be refined or coarsened at individual points, lines, surfaces, or volumes to give the user more power to control the analysis. A 3-dimensional finite element mesh was generated as either fine or very fine density. The mesh density was dependent on the model geometry and size. The mesh was designed so that each model would roughly have the same number of elements along the modeled pile cap. The elements used in Plaxis 3D are generally 10-node tetrahedral elements as shown in Figure 4.1.

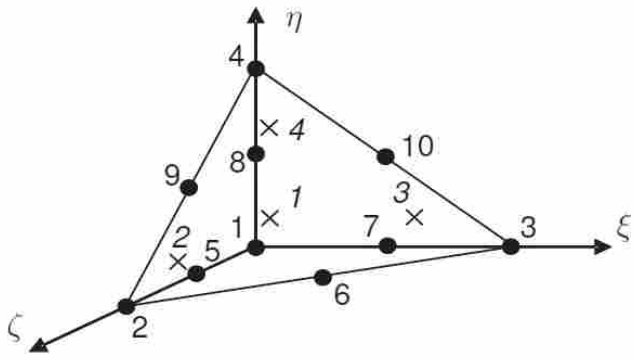

Figure 4.1. 10-node tetrahedral element used in Plaxis 3D (Plaxis 3D Reference Manual)

After the meshing is completed, the calculation stages need to be defined. Calculation stages in Plaxis 3D are designed to simulate stages of construction on a project. For example, in the construction of new building, a sheet pile wall might be installed as phase one prior to the second phase of excavation. These different stages in the calculation process help the user to define the soil conditions and geometry from start to finish. Furthermore, this aids in understanding whether to use total or effective stress conditions and is critical in design.

Once the calculation stages have been defined and the calculation is selected, Plaxis 3D gives the user the options to select Gaussian stress points. Selecting these stress points tells the program to run and save the calculations for these specific points. This data can then be used to develop stress-strain, load-displacement, and other relationships. It is important to note that if Gaussian stress points are not selected, the data can still be accessed, and data is saved for a certain amount of calculation steps that must be pre-selected in the calculation stages. In addition, when using the latter method, the coordinates of the selected points are only approximate and if more precise points are desired, then Gaussian stress points should be selected. This option to select Gaussian stress points was not used in this case as the pile cap is rigid, meaning each point along its face is displaced the same amount and would generate the same passive force-deflection curve. Therefore, Gaussian stress points were not needed.

The duration of the calculation process can vary greatly depending on the complexity of the model and density of the mesh. The calculations may continue for as little as a few hours or as long as a week. After calculation of all stages is completed, the results can be viewed in the Plaxis 3D Output subprogram as previously discussed.

4.2 Material Modeling

As mentioned previously in section 4.1, Plaxis 3D uses multiple soil constitutive models which define the necessary input soil parameters. These models vary in complexity and include the Mohr-Coulomb model (linear-elastic perfectly plastic), the Hoek-Brown model (rock behavior), the Hardening Soil model (isotropic hardening), the Hardening Soil Model with Small-Strain Stiffness, the Soft Soil model, the Soft Soil Creep model (time dependent behavior), the Jointed Rock model (anisotropy), the Modified Cam-Clay Model, the NGI-ADP model (anisotropic undrained shear strength), and the Sekiguchi-Ohta model. The user also has the option of inputting a custom soil constitutive model. The Hardening Soil model was determined to be the most appropriate for this study and was used in every model developed for this thesis.

4.3 Development of Finite Element Models

The boundary extents and geometric elements of the finite element models were developed as described above in Section 4.1. The boundaries modeled the 2:1 side slopes and the 24 feet of backfill materials behind the abutment backwall. The boundaries extend laterally to include only the compacted backfill as depicted in the test layout (5 feet on either side of the abutment, see Section 3.3.6). This is due to having only soil data for the backfill material and it was the only area monitored with instrumentation throughout the study (Smith, 2014). The 0° skew and 45° skew models were designed to model the geometry of the field tests and are shown below in Figure 4.2 and Figure 4.3.

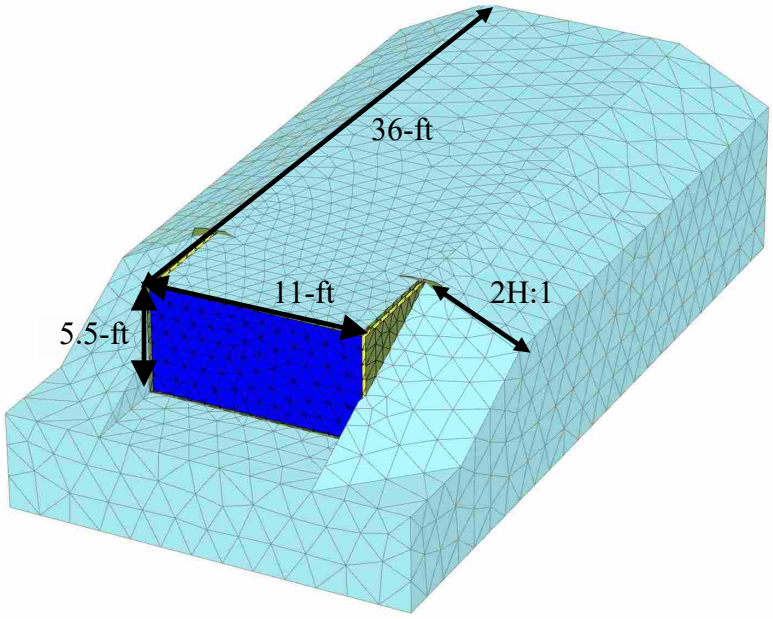

Figure 4.2. Generated mesh for calibrated 0° skew abutment.

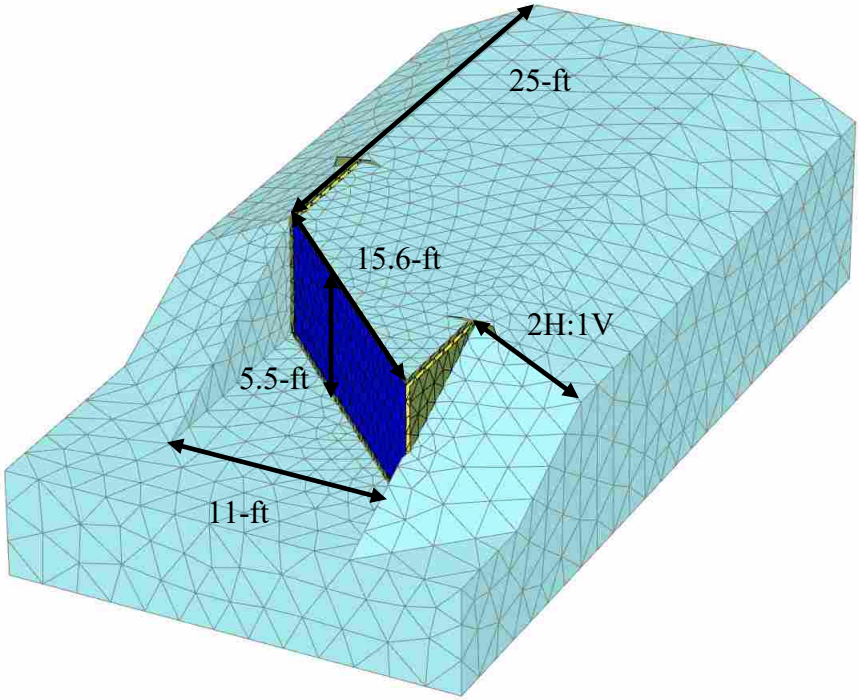

Figure 4.3. Generated mesh for calibrated 45° skew abutment.

These models were designed to match the field test configurations shown in Figure 3.9 and Figure 3.10. Care was taken to simplify the models in order to reduce the computer run time. This was done by the use of mesh refinement. Table 4.1 details the coarseness of each model mesh, the number of elements, nodes, and stress points involved, and the model dimensions.

Table 4.1. Calibrated Model Details

Model	*Coarseness*	*Elements*	*Nodes*	*Stress Points*	*Model Dimensions (x,y,z)*
0 Degree Skew	Fine	19,656	30,544	78,624	(21, 40, 10.5)
45 Degree Skew	Fine	20,273	31,432	81,092	(21, 40, 10.5)

The backfill on the side of the abutment was designed with a 2H:1V slope as designated in Section 3.3.6. The pile cap (in dark blue) and wingwalls (in yellow) were modeled using a "plate" with properties as shown in Table 4.2 and Table 4.3**,** respectively.

Table 4.2. Reinforced Concrete Pile Cap Properties

Property	*Value*	*Units*
Plate Thickness, d	15	ft
Unit Weight, γ	150	lbf/ft^3
Young's Modulus, E	635.8E6	lbf/ft^2
Poisson's Ratio, ν	0.20	–
Shear Modulus, G	264.9E6	lbf/ft^2

Table 4.3. Reinforced Concrete Wingwall Properties

Property	*Value*	*Units*
Plate Thickness, d	1	ft
Unit Weight, γ	150	lbf/ft^3
Young's Modulus, E	519.0E6	lbf/ft^2
Poisson's Ratio, ν	0.20	–
Shear Modulus, G	216.3E6	lbf/ft^2

These values were obtained using correlations for Young's Modulus (E) and the Shear Modulus (G), and by using generally accepted values for the unit weight and Poisson's ratio of normal weight concrete. Young's modulus was estimated using Equations (4-1) and the respective concrete compressive strengths for the pile cap and the reinforced concrete wingwalls of 6000 and 4000 psi.

$$E = 57{,}000\sqrt{f'_c} \tag{4-1}$$

where,

$f'_c = \text{Concrete compressive strength (psi)}$

Shear modulus was computed using the following equation:

$$G = \frac{E}{2(1+v)} \tag{4-2}$$

where,

$E = \text{Young's Modulus}$

$v = \text{Poisson's ratio}$

The PYCAP program (Duncan and Mokwa 2001) was used to estimate the soil parameters in Table 4.4 (Franke, 2013) that were used as the initial strength and stiffness values in the finite element model. These values were input into the hardening soil model and were used to create the initial models.

Table 4.4. Optimized Soil Parameters from PYCAP

Property	*Value*	*Units*
Young's Modulus, E	415	kip/ft^2
Soil Friction Angle, ϕ	40	Degrees
Wall Friction Angle, δ	28	Degrees
Cohesion, c	85	lbf/ft^2
Poisson's Ratio, ν	0.2	N/A
Soil Unit Weight, γ	117	pcf
Adhesion Factor,α	1	
Dmax/H	0.032	-

These values were obtained using field and lab tests, default values, and assumed values within the PYCAP program. The initial stiffness, or Young's Modulus (E), and the wall friction angle were estimated using PYCAP, whereas the soil friction angle, cohesion, and the soil unit weight were approximated from field and lab tests (see section 3.4.2). Poisson's ratio of 0.2 for reinforced concrete is a generally assumed value and is typically used as a default in Plaxis.

Once the geometry and material modeling were complete, interface elements were added to more accurately model the soil-structure interaction. Without interface elements, Plaxis assumes that the structural elements and the adjacent soil are connected and are displaced together because they share common nodes in the finite element mesh as shown in Figure 4.4. If interface elements

are added, relative movement between the structural element and the adjacent soil is allowed, which better simulates field conditions.

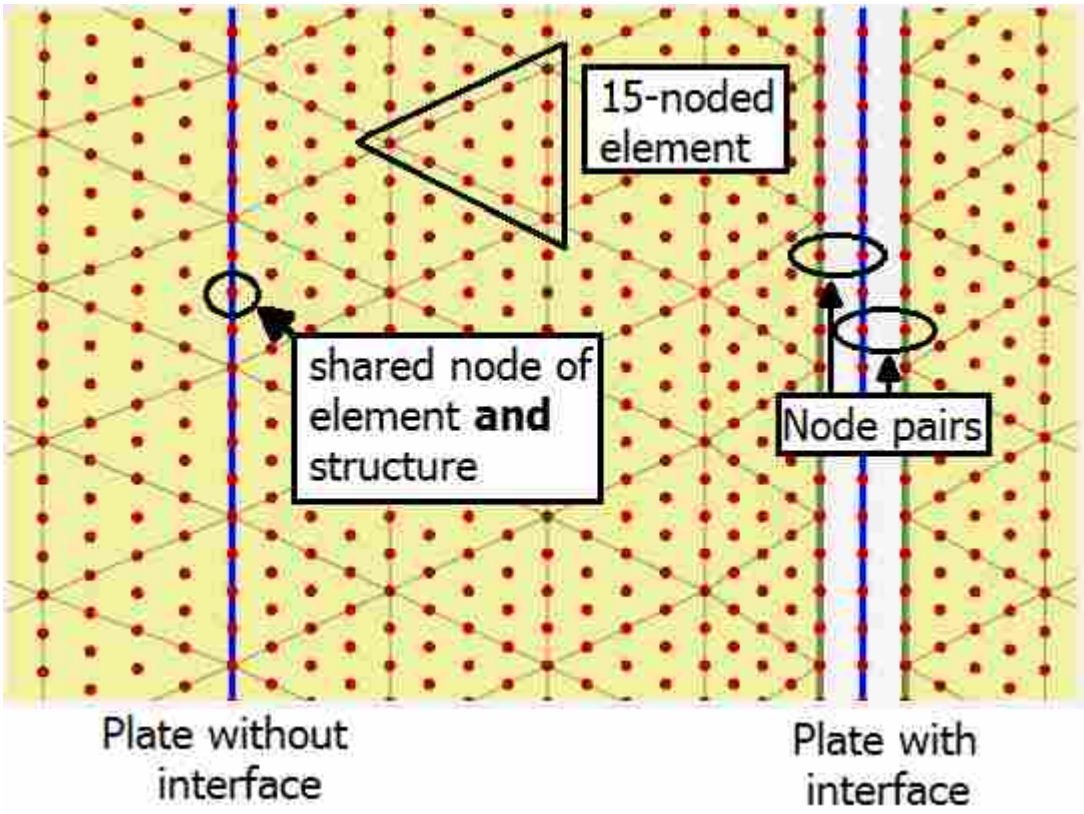

Figure 4.4. Example of soil-structure interaction with and without interface elements (Plaxis 3D Reference Manual 2012).

These interface elements also account for strength reductions caused by soil-structure interactions. According to the Plaxis 3D Reference Manual (Plaxis 3D 2015), the strength reduction factor, R_{inter}, should be equal to 1.0 (rigid) for soil-soil interaction as there should be no reduction of soil strength. However, Plaxis allows a manual input of R_{inter} to account for the reduction in strength caused by a smoother surface (structure) interacting with a rougher surface (soil). The manual states these values should normally be about 2/3.

Using the previously discussed parameters from the PYCAP optimization, the initial strength reduction factor, R_{inter} for soil to concrete interaction was estimated as $R_{inter} = 0.634$. These values were calculated using Equation (4-3).

$$R_{inter} = \frac{\tan\delta}{\tan\varphi} \tag{4-3}$$

where,

$\delta = 28°$ (wall friction angle)

$\phi = 40°$ (soil friction angle)

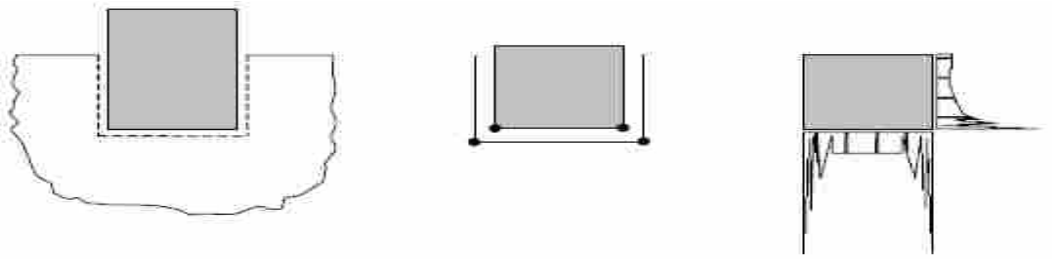

(a) Oscillating stress distributions occur around structure corner points

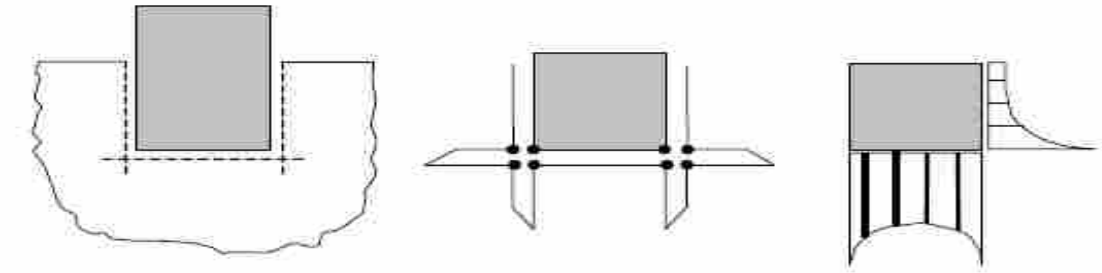

(b) Enhanced stress results using interface element extension plates

Figure 4.5. Stress distributions formed at the corners of structural elements with and without interface elements (Plaxis 3D Reference Manual).

Interface elements also aid in preventing unrealistic stress distributions that can develop at corner points in the mesh. Figure 4.5 shows the differences in stress distributions with and without

interface elements. The figures use the term “interface element extension plates” which are essentially fictitious plates that are created in Plaxis to allow slippage within the soil at geometrical discontinuities. These plates are created in order to assign additional interface elements to the edges of the modeled structure.

Plaxis recommends extending the interface elements beyond the edges of the pile cap and into the soil backfill using the interface element extension plates. The interfaces were extended approximately 1-ft into the backfill. Interface elements for the 0° skew model are shown in Figure 4.6 and Figure 4.7. The interface set up is the same for the 45° skew model, except the interface elements associated with the pile cap are angled at 45°. These interface elements (in turquoise and black) are shown relative to the interface element extension plates (in grey), the pile cap (in blue), and the reinforced concrete wingwalls (in yellow). The turquoise interfaces have interface strength reduction factors that represent the reduced friction in the soil-concrete relationship relative to soil to soil interaction as stated above. In contrast, the black interfaces were defined in areas of soil to soil interaction with R_{inter} = 1.0 representing no reduction. The interfaces were designed to be located in areas where high displacement would occur around the pile cap and wingwalls and were designed to extend 1-ft on either side and below each wingwall. The pile cap interfaces also extended 1-ft beyond either side and 1-ft below the base. The last interface element was placed at the base of the abutment and extended 1-ft in the direction of displacement to ensure that the model would account for both lateral and vertical displacement of the abutment.

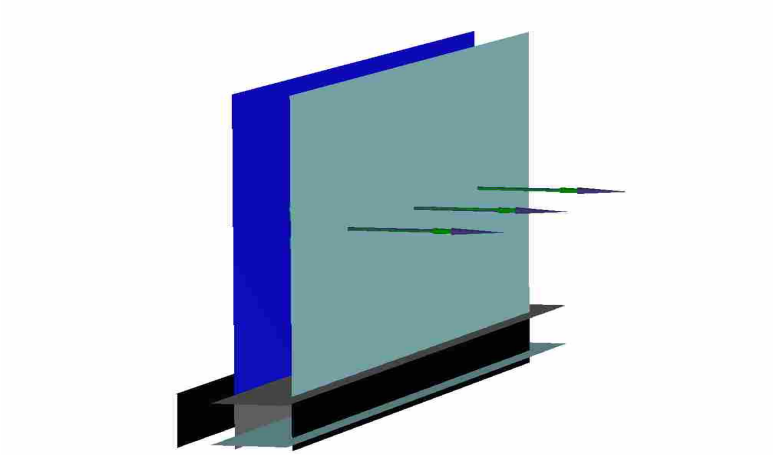

Figure 4.6. Interface elements for pile cap.

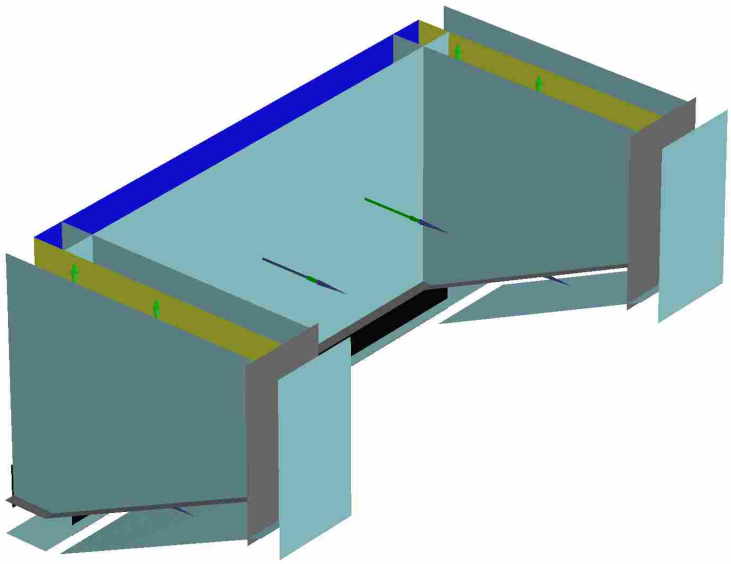

Figure 4.7. Pile cap and reinforced concrete wingwall interfaces.

4.4 Calculation Stages

After the initial models had been developed and parameters were selected, the final step in performing the finite element analysis was to perform the calculation stages. The first stage of this

analysis is called the “initial phase”. During this phase, the material and soil parameters are assigned to their respective elements along with their dimensions. In a way, the first phase simulates the construction or setup of the test in the field. The second stage simulates the displacement of the abutment into the soil backfill. This is done by assigning a prescribed displacement (or enforcing the pile cap and wingwalls to displace longitudinally (“y” direction) into the backfill) of 3.5-inches to each of the three structural elements (the two wingwalls and the pile cap). The structural elements were restrained in the “z” direction (vertical), but were allowed free lateral movement (“x” direction). Assigning this displacement was done at the time the plates representing the abutment were created. However, this final phase simply activates this displacement into the backfill. Once the calculation stages are complete, the results are viewed in the Plaxis 3D Output.

The Plaxis 3D Output file allows the user to view a variety of forces and displacements as will further be discussed in Chapter 5. However, in order to calculate the passive force of the soil backfill, points along the pile cap of the face were selected and graphs were plotted by Plaxis representing the longitudinal force vs. longitudinal displacement. For the 0 Degree Skew model, the load required to displace the pile cap and wingwalls into the soil is the passive force. For the 45 Degree Skew, the passive force is the component of the longitudinal load that is perpendicular to the pile cap face. To calculate this component, the longitudinal force must be reduced by a factor 0.707 (or cos45°).

4.5 Calibration of Finite Element Models

The parameters developed in Section 4.3 are shown in Table 4.5 and were used as a basis for the finite element models developed in this study.

Table 4.5. Initial Model Soil Parameters

Property	*Value*	*Units*
Young's Modulus, E	415	kip/ft^2
Soil Friction Angle, ϕ	40	Degrees
Wall Friction Angle, δ	28	Degrees
Cohesion, c	85	lbf/ft^2
Poisson's Ratio, ν	0.2	N/A
Soil Unit Weight, γ	117	pcf
R_{inter}	0.634	-

These initial values were input into the Plaxis 3D models for the 0° and 45° skew configurations and the simulations were run to produce passive force-deflection curves. These models were then "calibrated" to match the field test passive force-deflection curves by making small modifications to various soil parameters.

The calibration was performed in a methodical manner which involved varying one parameter at a time to determine its effect on the passive force-deflection curves. Additional guidance was provided by parametric studies that were performed by Guo (2015).

Calibration was achieved by modifying the following parameters: the stiffness, friction angle, wall friction angle, and the interface strength reduction factor. The stiffness required the greatest modification and produced the largest effect on the passive force-deflection curves. The friction angle was reduced from 40° to 38° and the wall friction angle was slightly increased to 28.5° from 28° using the relationship of $\delta/\phi = 0.75$ rather than $\delta/\phi = 0.70$. The interface friction

ratio was then recalculated as R_{inter} = 0.695. In addition, the dilatancy angle (ψ) was calculated from Equation (4-4) as an input parameter for the Hardening Soil Model as outlined in the Plaxis User's Manual.

$$\psi = \varphi - \alpha \tag{4-4}$$

where,

$\varphi = \text{soil friction angle}$

$\alpha = 30° \text{ (angle ranging from } 25° \text{ to } 35°)$

Varying these parameters produced passive force-deflection curves that were much more consistent with the field tests performed by Smith (2014) and are shown alongside the respective field tests in Figure 4.8 and Figure 4.9. Relatively good agreement was achieved between the calibrated 0 and 45 Degree Skew models and the performed field tests. The 0 Degree Skew model achieved results with up to about 12.5% error between the field tests and the calibrated model whereas the 45 Degree Skew model achieved results with up to about 13.5% error. As the passive force vs. displacement for the field test appears to increase linearly after a displacement of 2.7 inches (which is likely not realistic), the % error between these two cases was evaluated between a displacement of 0 and 2.7 inches for the 0 Degree Skew models and at 2.93 inches for the 45 Degree Skew model.

As these curves show relatively good agreement with the large-scale test results, it follows that the skew reduction factor produced by these models is similarly underestimating the expected reduction for the 45 degree skew case as shown in Figure 4.10.

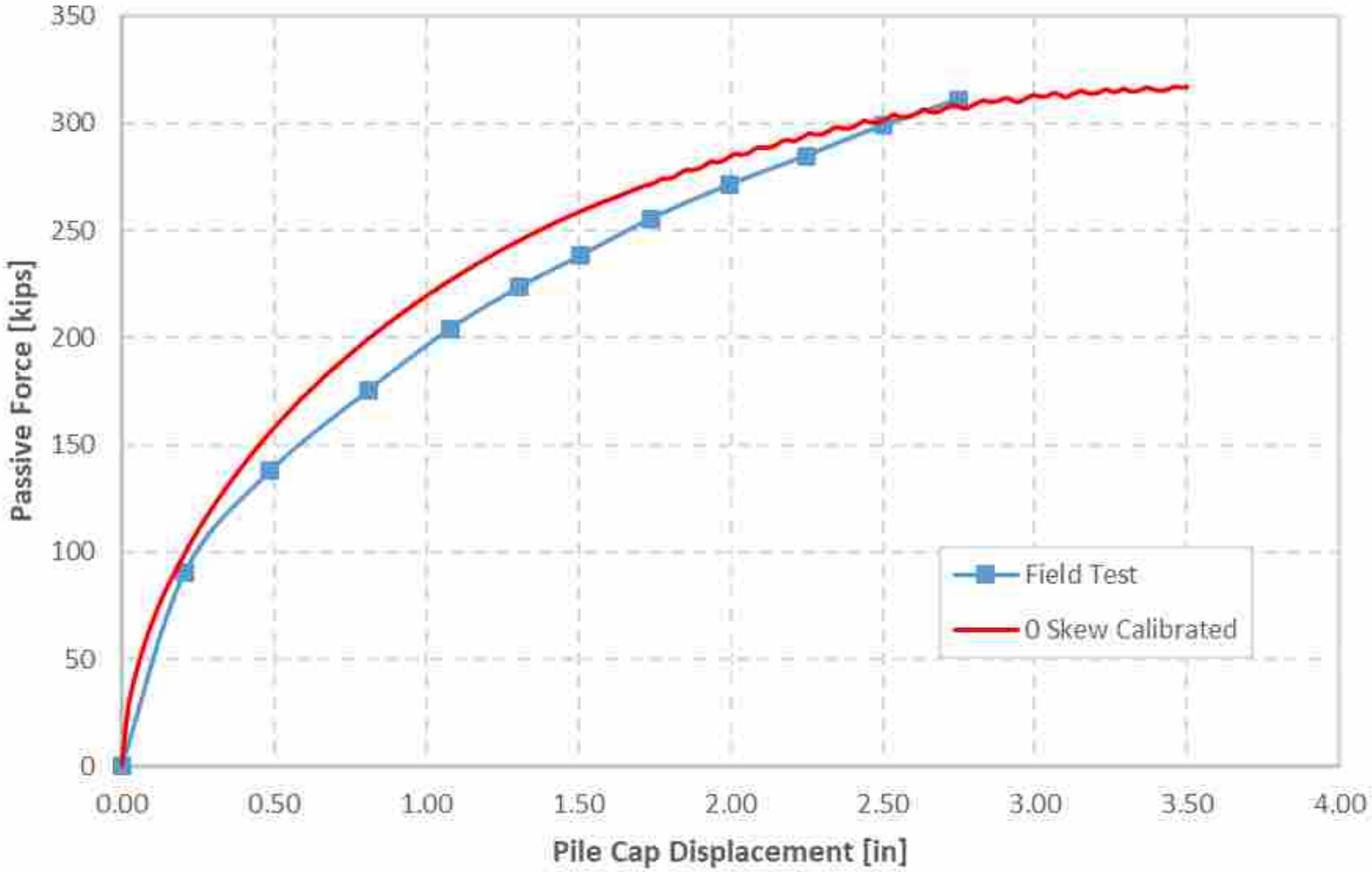

Figure 4.8. Passive force-deflection curve for calibrated 0° skew.

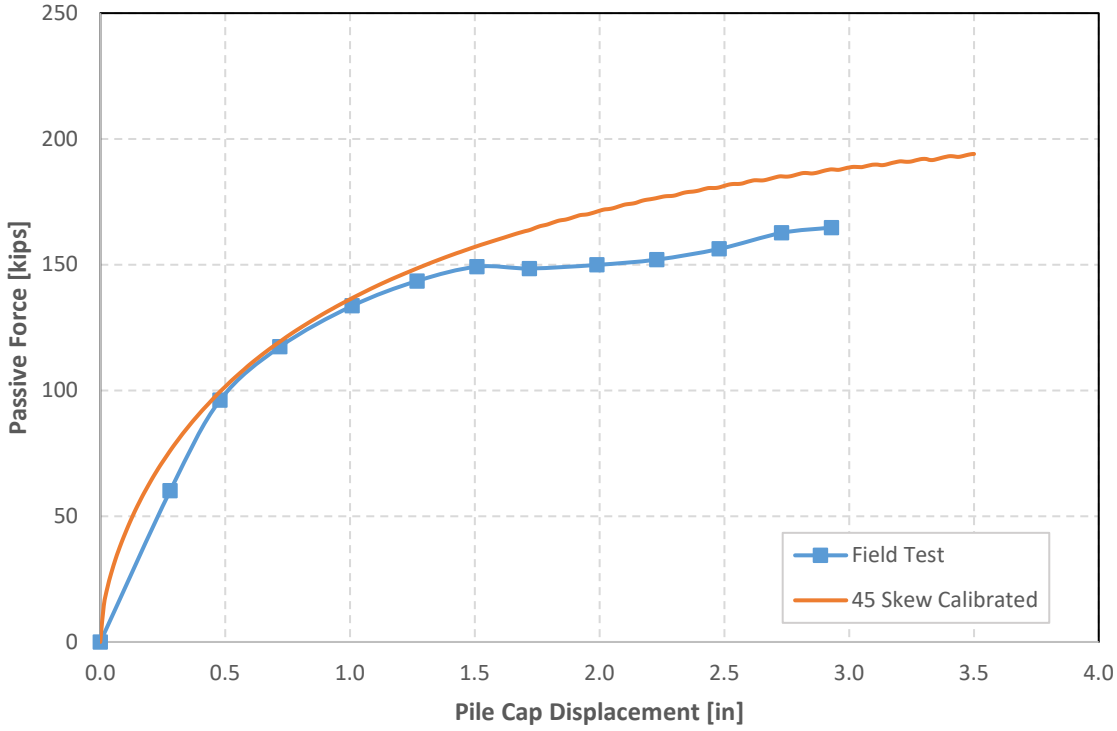

Figure 4.9. Passive force-deflection curve for calibrated 45° skew.

In addition, despite already being somewhat high, the skew reduction factor achieved by the large-scale tests for the 45-degree skew may be artificially low. The calculation of the skew reduction factor involved the passive force at 2.93 inches of displacement for the 45-degree skew and the passive force at 3.7 inches of displacement for the 0-degree skew. In addition, for the 0-degree skew field test results, the passive force increased linearly from a displacement of approximately 2.7 inches to 3.7 inches which seems unrealistic. This study estimates a more realistic skew reduction factor of 0.52 based on the passive force at displacements of approximately 2.5 inches as shown below on Figure 4.10.

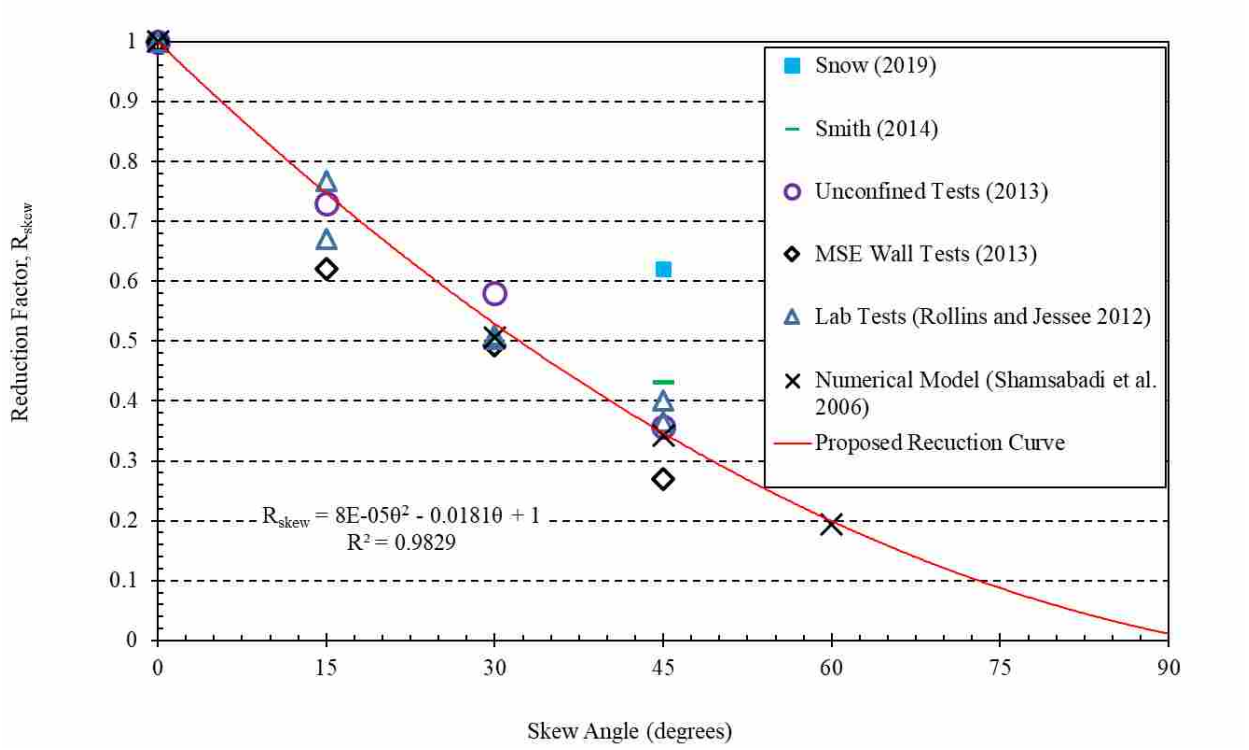

Figure 4.10. Skew reduction curve including calibrated model results.

The calculated R_{skew} value of 0.62 based on the calibrated models seems relatively high upon first glance. However, when considering the revised R_{skew} values produced by the large-scale field tests (0.52) and that the passive force deflection curves are up to approximately 13.5% higher, this value seems appropriate. It is important to note that the R_{skew} value decreases significantly as the abutment width increases as shown later in this study.

The calibrated parameters are listed in Table 4.6 and will be used to develop additional models for this study.

Table 4.6. Calibrated Soil Parameters

Symbol	*Parameter*	*Value*	*Default Units*
	Failure parameters (same as for Mohr-Coulomb model)		
c	(Effective) cohesion	85	[lb/ft^2]
ϕ	(Effective) angle of internal friction	38	[°]
δ	Wall friction angle	28.5	[°]
ψ	Angle of dilatancy	8	[°]
R_{inter}	Interface Friction Ratio	0.695	[-]
	Basic soil stiffness parameters		
γ_{unsat}	Unsaturated Unit Weight	116.5	[lb/ft^3]
γ_{sat}	Saturated Unit Weight	120	[lb/ft^3]
E_{50}^{ref}	Secant stiffness in standard drained triaxial test	1.0E6	[lb/ft^2]
E_{oed}^{ref}	Tangent stiffness for primary oedometer loading	1.0E6	[lb/ft^2]
E_{ur}^{ref}	Unloading/reloading stiffness (default $E_{ur}^{ref} = 3E_{50}^{ref}$)	3.00E6	[lb/ft^2]
m	Power for stress-level dependency of stiffness	0.5	[-]
	Advanced parameters		
ν_{ur}	Poisson's ratio for unloading-reloading (default $\nu_{ur} = 0.2$)	0.2	[-]
p^{ref}	Reference stress for stiffness (default $p^{ref} = 100$ kN/m^2)	2089	[lb/ft^2]
K_0^{nc}	K_0-value for normal consolidation (default $K_0^{nc} = 1 - sin\phi$)	0.3843	[-]
R_f	Failure ratio q_f/q_a (default $R_f = 0.9$)	0.9	[-]
σ_{tensio}	Tensile strength (default $\sigma_{tension} = 0$ stress units)	0	[lb/ft^2]
c_{inc}	Incremental increase in cohesion with depth (default $c_{inc} = 0$)	0	[lb/ft^2]
	Alternative soil stiffness parameters		
C_c	Compression index	3.865E-3	[-]
C_s	Swelling index or reloading index	1.392E-3	[-]
e_{init}	Initial void ratio	0.5450	[-]

4.6 Finite Element Analysis

The essential steps to performing a finite element analysis have partially been described throughout this thesis. The following list outlines the basic steps that were used to perform this finite element analysis:

1. The Plaxis 3D Input program was used to develop a structural model containing geometric elements comparable to field testing and the calibrated soil and material properties.
2. A 3-dimensional finite element mesh was generated as either medium or fine density. The mesh density was dependent on the model geometry and size. The mesh was designed so that each model would roughly have the same number of elements along the modeled pile cap.
3. The option to select Gaussian stress points was available but was not used. Because the pile cap is rigid, each point along its face is displaced the same amount and would generate the same passive force-deflection curve, therefore any point along its face would function the same.
4. The first stage of this analysis is called the “initial phase”. During this phase the material and soil parameters are assigned to their respective elements along with their dimensions. In a way it simulates the construction or setup of the test in the field. The second stage simulates the displacement of the abutment into the soil backfill. This is done by assigning a prescribed displacement of 3.5-in to each of the three structural elements (the two wingwalls and the pile cap). Assigning this displacement was done at the time the plates representing the abutment were created, however, this final phase simply activates this

displacement into the backfill. Once the calculation stages are complete, the results are viewed in the Plaxis 3D Output program.

5 RESULTS AND DISCUSSION

This chapter will present the results of the finite element analysis. It will include comparisons between field test results (Smith, 2014) and the calibrated models. Additional results from models that were created to simulate 2-lane non-skewed and skewed bridge abutments will also be presented.

5.1 Large-Scale Test Results vs. Calibrated Model Results

The results from the large-scale tests, i.e., the passive force deflection curves, are the basis for the comparisons made in this study. Once relatively good agreement had been achieved, each of the following relationships were compared, including the Longitudinal Displacement of the Soil Backfill, Shear Failure Plane geometry, Soil Heave, Backwall Pressure Distributions, Wingwall Deflection, Wingwall Pressure Distributions, and Wingwall Bending Moments.

5.1.1 Passive Force Deflection Curves and Skew Reduction Factor

As previously discussed in Section 4.5, the passive force deflection curves for the calibrated models had relatively good agreement with the field tests performed by Smith (2014) with up to 12.5% and 13.5% error in the 0 and 45-degree skew models, respectively.

In addition, despite already being somewhat high, the skew reduction factor achieved by the large-scale tests for the 45-degree skew may be artificially low. The calculation of the skew

reduction factor involved the passive force at 2.93 inches of displacement for the 45-degree skew and the passive force at 3.7 inches of displacement for the 0-degree skew. In addition, for the 0-degree skew field test results, the passive force increased linearly from a displacement of approximately 2.7 inches to 3.7 inches, which seems unrealistic. This study estimates a more realistic skew reduction factor of 0.52 based on the passive force at displacements of approximately 2.5 inches as shown in Figure 5.1.

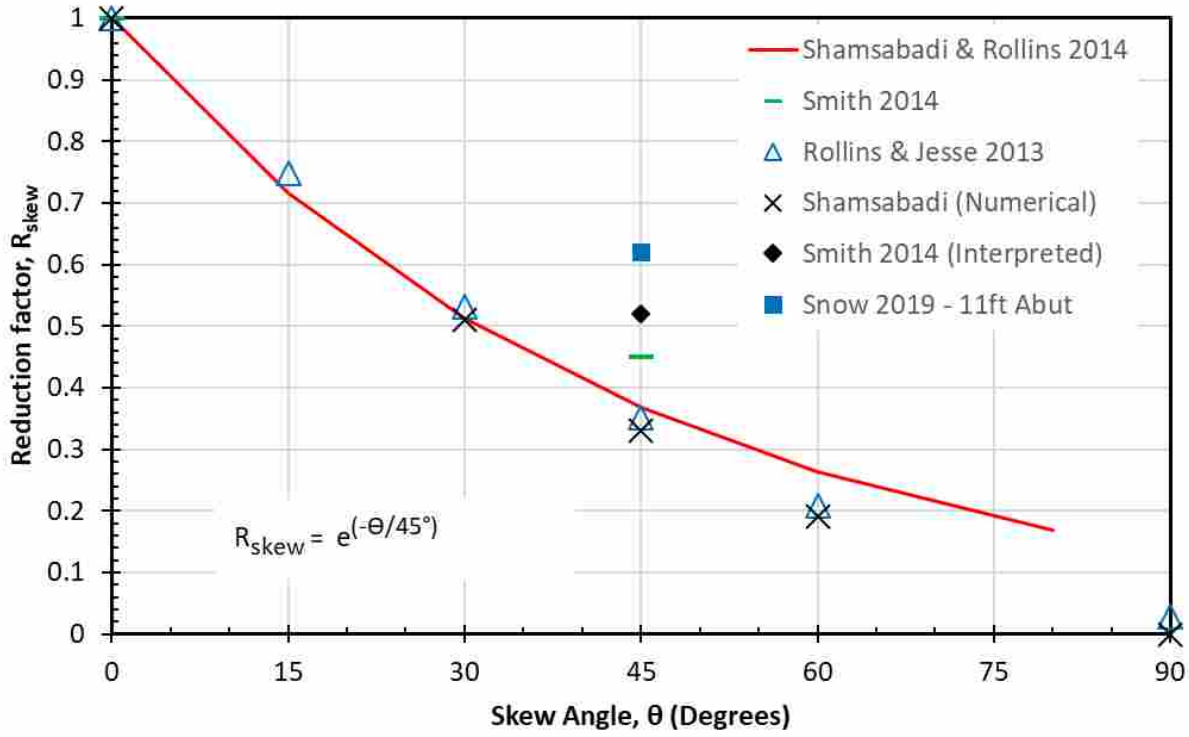

Figure 5.1. Skew reduction curve with skew reduction factor from field tests and calibrated finite element model.

5.1.2 Longitudinal Displacement of Soil Backfill

The longitudinal displacements of the soil backfill from field tests for both the 0° and 45° skew abutments are shown in vector form in Figure 5.3. In comparison, the longitudinal displacements of the 0° and 45° skew calibrated models are displayed in Figure 5.5.

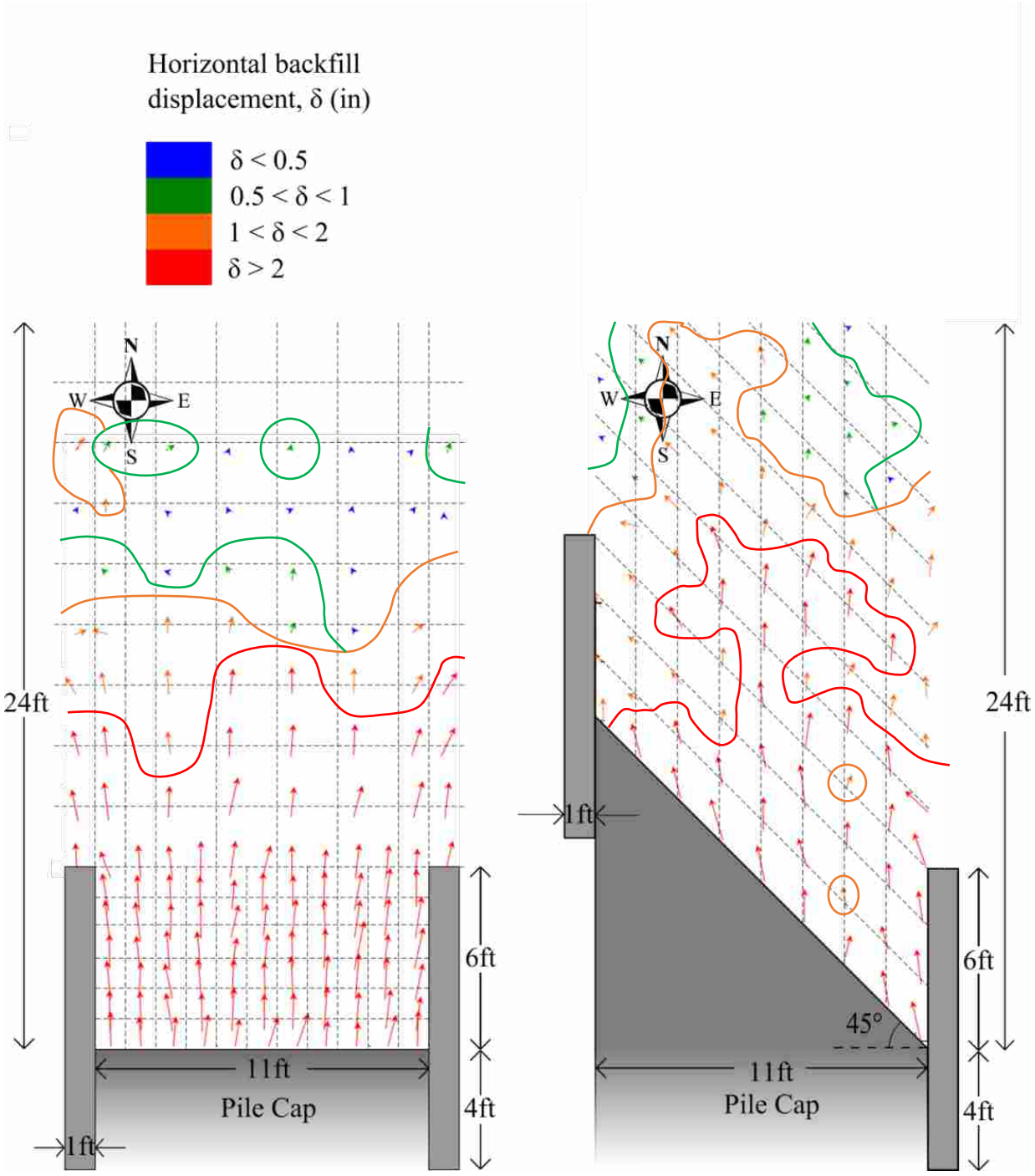

Figure 5.2. Horizontal backfill displacement for 0° and 45° skew at test completion (2ft grid in vertical direction and parallel to abutment skew—refined to 1ft grid within 6ft of pile cap for 0° skew test) by Smith (2014).

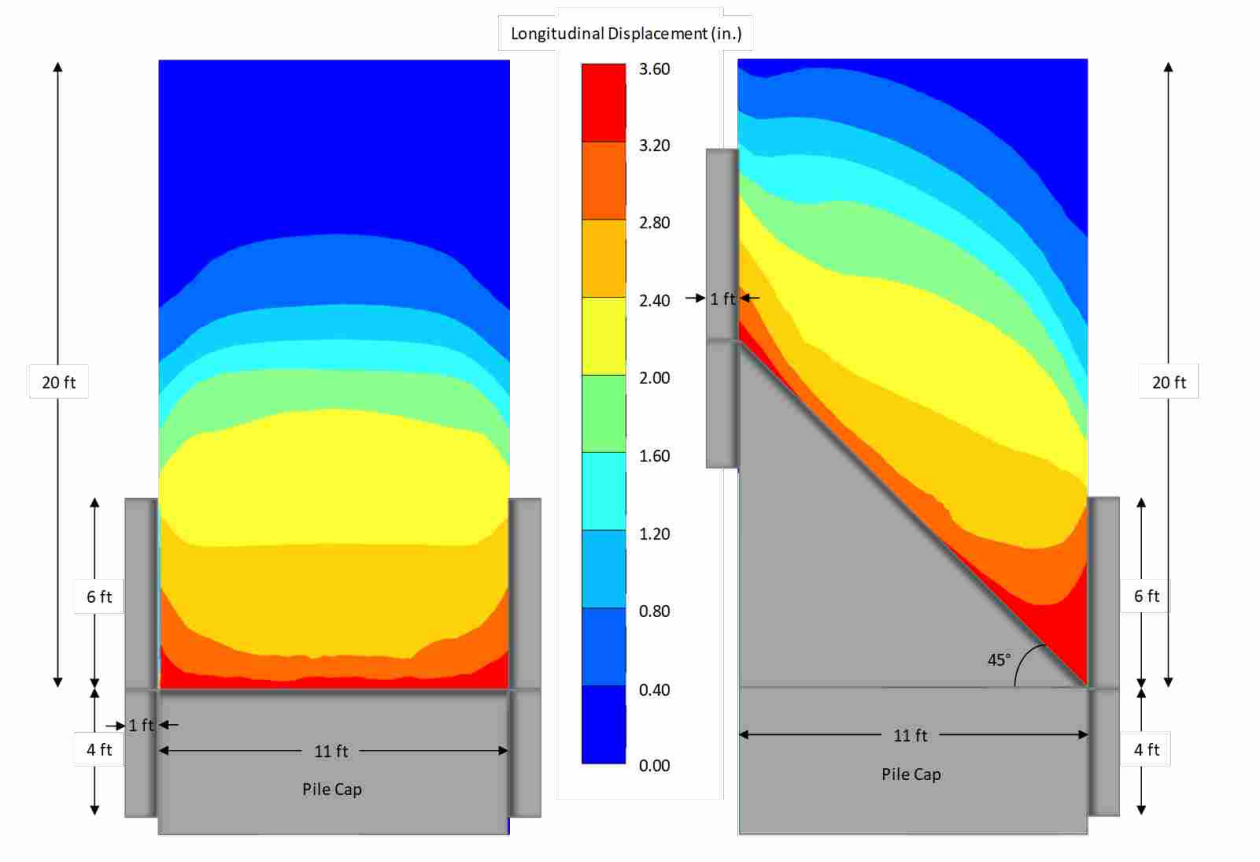

Figure 5.3. Longitudinal displacement of 0° and 45°skew calibrated Plaxis models.

Generally, the results from the FEM computer model compare well with field test data. For the 0° skew tests, the resulting displacements range from about 3.5 inches near the face of the abutment backwall to about 1 to 2 inches just beyond the wingwalls for the computed and measured results.

The displacement results are also similar for the case of the 45º skew tests. Both the field test data and the calibrated model show a small soil pocket trapped between the obtuse side of the abutment and the wingwall. This soil pocket is shown to displace with the abutment and likely increases the length of the failure wedge, which will be discussed in the next section. In addition, this highly constrained pocket of soil can change the effective skew angle of the backfill. This

information is important as it may allow engineers to reconsider how they backfill these regions of entrapped soil.

5.1.3 Shear Failure Planes

Vertical cross sections were taken through the models in the longitudinal direction as depicted in Figure 5.4, to represent the shear failure planes that developed. Due to the 0° skew

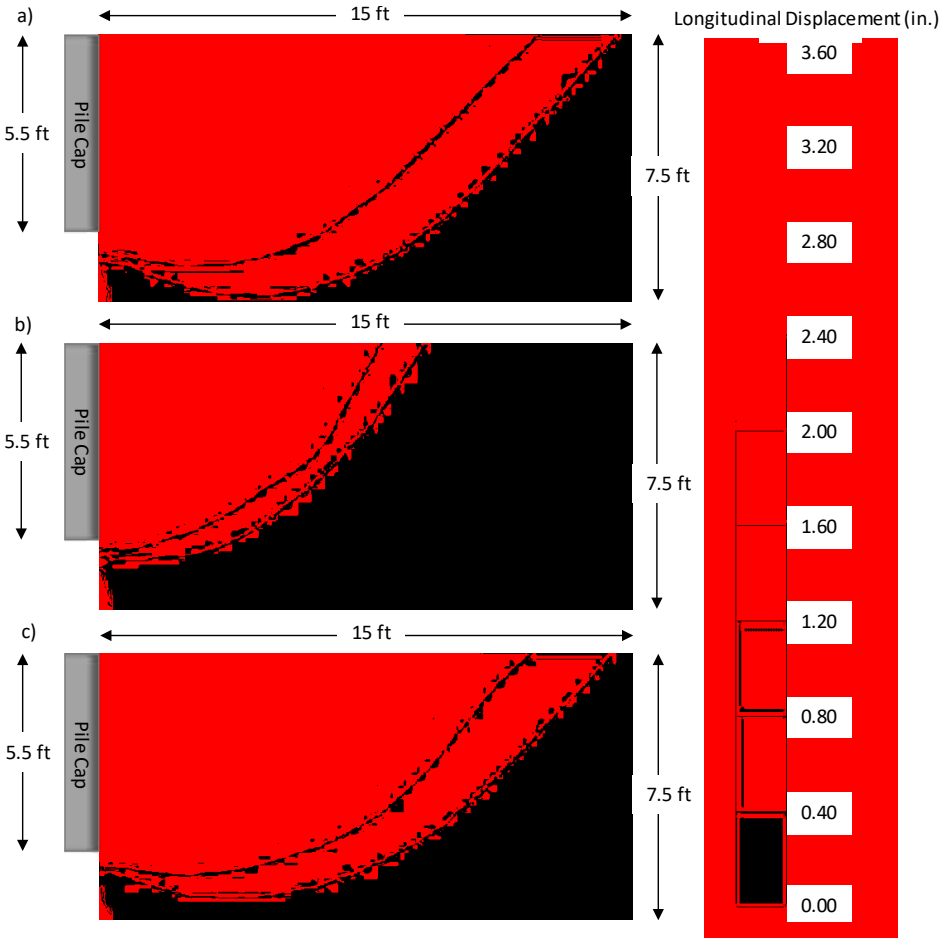

Figure 5.4. Longitudinal displacement showing shear planes of 0° skew model (a), 45° skew model (b) at acute end of abutment, and 45° skew (c) model at obtuse end.

model being symmetrical, only one cross section was taken whereas cross sections were taken at both the acute and obtuse ends of the abutment for the 45° skew model.

Figure 5.4 shows vertical cross sections of the longitudinal displacement of both the 0° and 45° skew models. The top cross section (a) is taken in the middle of the backwall of the 0° skew model as the results are essentially symmetrical. The middle (b) and bottom (c) cross sections are taken approximately 1.2 inches inside the west and east wingwalls, respectively. This plot shows the shape of the shear failure planes for both cases and confirms that they are best approximated by a log-spiral curve as previously predicted. It is important to note that the length of the shear failure plane varies in each case. The acute side of the abutment for the 45° skew model produces the shortest shear failure plane and ultimately the least amount of displacement, whereas the obtuse end of the abutment of the 45° skew model and 0° skew model produce similar results. The reason for the 45° skew model shear failure plane extending significantly farther back into the soil mass from the abutment backwall on the obtuse side of the abutment is likely due to the pocket of soil that is trapped by the wingwall and abutment and displaces with the structure. This soil displacement is shown in both Figure 5.2 and Figure 5.3 in red as a high displacement region.

5.1.4 Soil Heave

With the previously described boundary conditions, when the abutment was displaced longitudinally into the soil mass, the soil is displaced upwards (or heaves in the “z” direction). Color contours of the backfill soil heave in the field test and from the calibrated computer model are illustrated in Figure 5.5 and Figure 5.6, respectively.

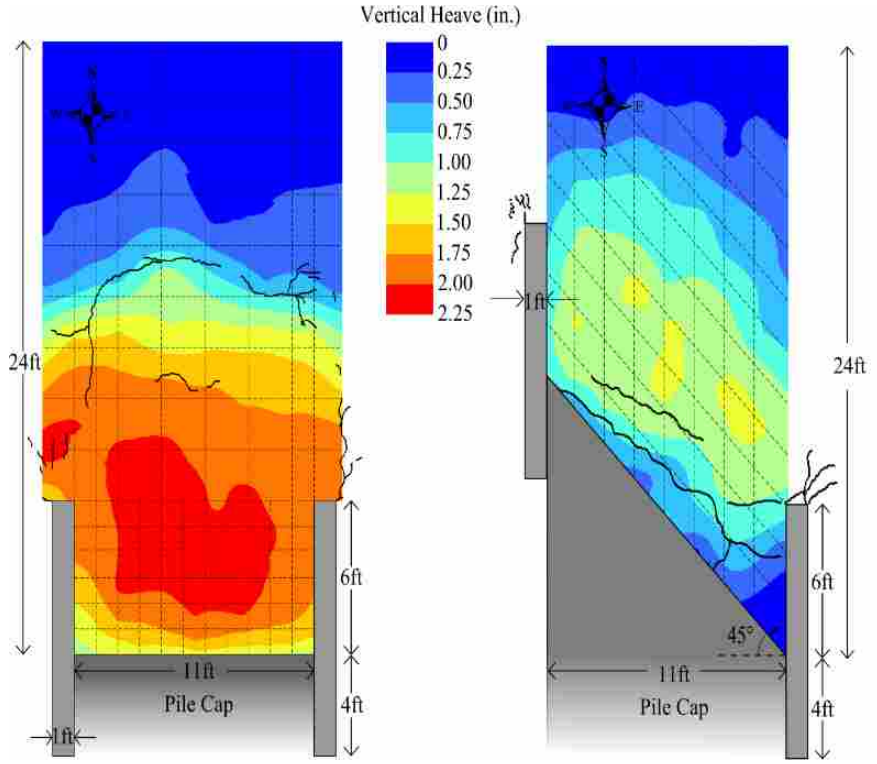

Figure 5.5. Vertical backfill heave for 0° and 45° skew abutment test (Smith 2014).

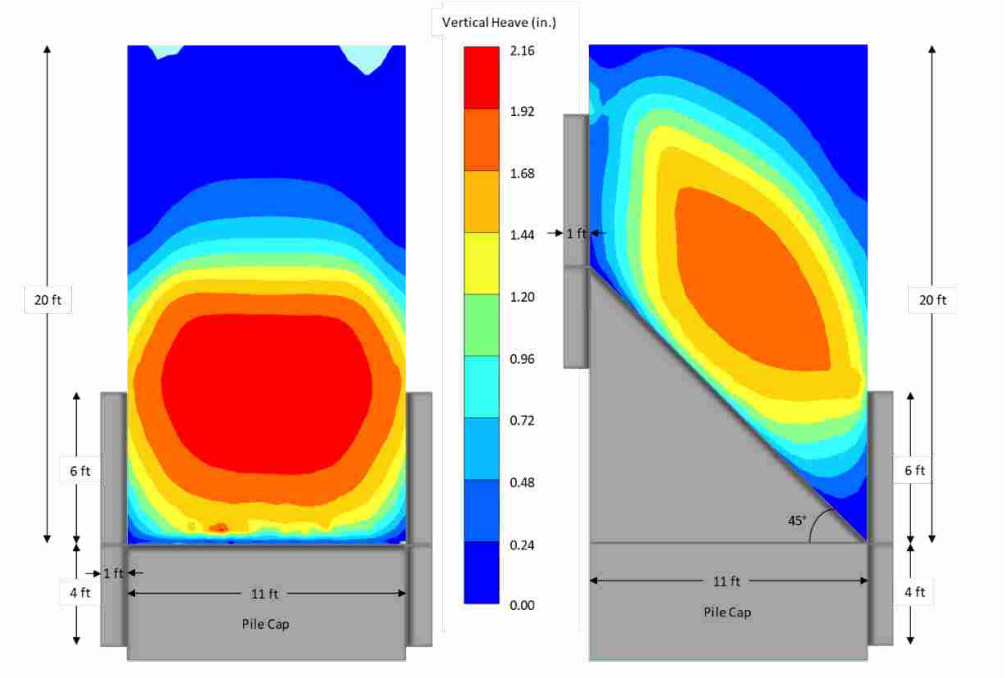

Figure 5.6. Heave for 0° and 45° skew models.

As shown in Figure 5.5, the field tests indicate about 2¼ and 1½ inches of heave for the 0° and 45° skew, respectively, whereas the calibrated models predict up to about 2.16 and 1.68 to 1.92 inches, respectively. Based on these results, the heave contours for the 0° and 45° skew models also appear to be consistent between both the field test and the computer model, meaning that they both depict relatively similar magnitudes of heave (as previously discussed) that are located in the same region (relative to abutment and wingwall locations). Both the field tests and calibrated models produce the highest levels of heave in regions located with the center approximately 6 feet (or the length of the wingwall) off the midpoint of the abutment backwall. These results also confirm the results of the field tests performed by Smith (2014) that show the 0° skew abutment produces greater heave in comparison to the 45° skew wingwall configuration. This is likely due to the fact that the soil is confined on both sides for the 0° skew test while the skew angle leads to less soil confinement behind the obtuse or east side.

5.1.5 Backwall Pressure Distribution

The pressure distributions along the face of the abutment backwall for the 0° and 45° skew calibrated models are shown in Figure 5.7.

Figure 5.7 shows the magnitude of the pressure acting longitudinally ("y" direction) on the abutment backwall of the 0° skew calibrated model (a) and the 45° skew calibrated model (b). This result was derived by taking a vertical slice through the soil mass at an approximately 1-inch offset from the abutment backwalls. It is important to note that while the plots represent the pressure

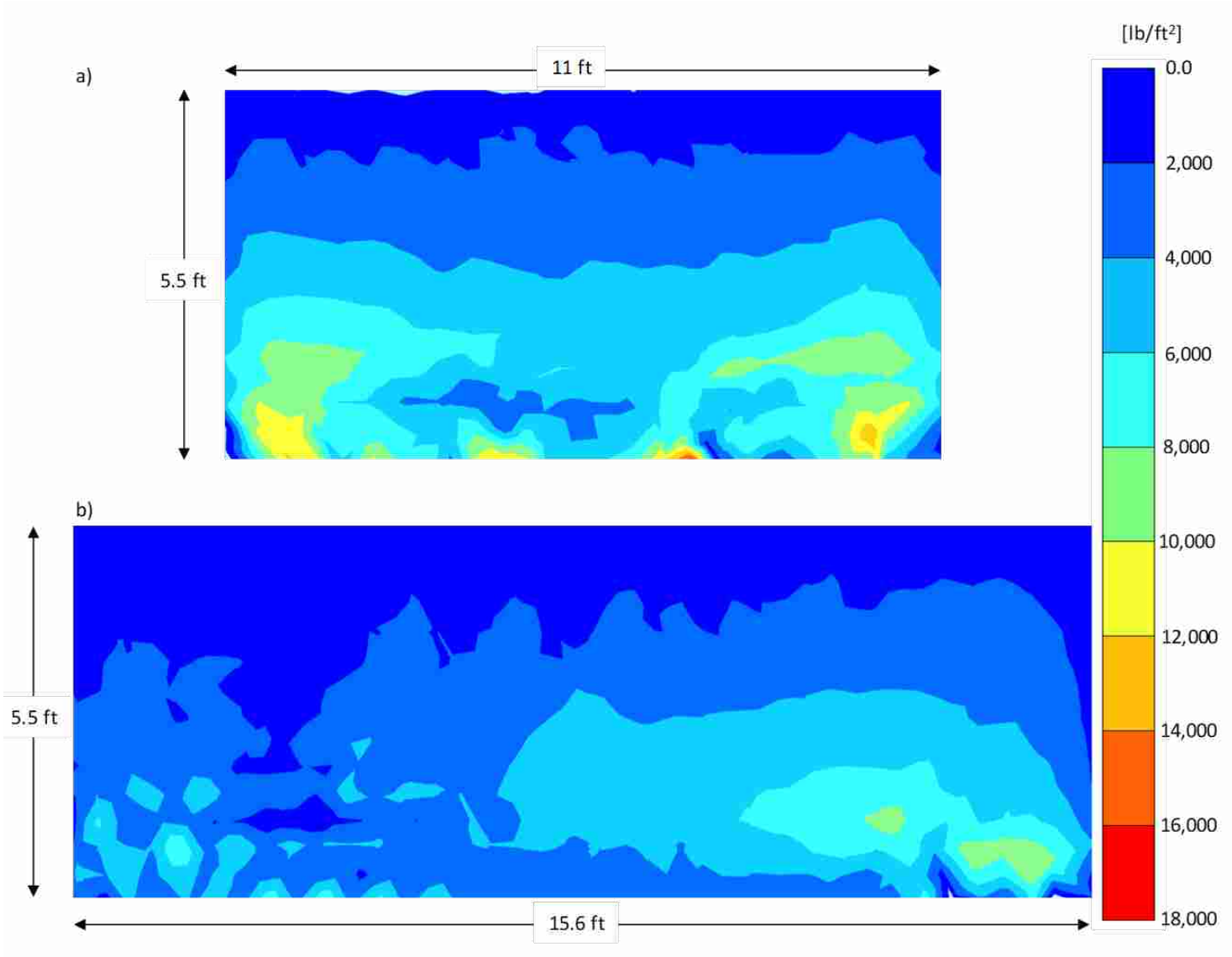

Figure 5.7. Soil pressure on the abutment backwall for (a) the 0° skew calibrated model and (b) the 45° skew calibrated model.

acting in the longitudinal direction, the backwall for the 45° skew model is oriented at a 45° angle from the longitudinal pressure. To accurately represent the backwall pressure of the 45° skew backwall, the contours of Figure 5.7(b) would need to be reduced by a factor of 0.707.

As might be expected, Figure 5.7 shows that the passive pressure is increasing towards the bottom of the abutment. For the 0° skew case, the passive pressures appear to be somewhat higher at the edges of the backwall relative to the center. For the 45° skew backwall, it also shows that the corner with the acute abutment-wingwall connection experiences significantly less soil pressure buildup (a reduction of approximately 25%) relative to the acute abutment-wingwall connection. For example, the acute side of the abutment has a magnitude of up to about 6,000 psf versus about 8,000 psf for the obtuse side of the abutment near the wingwall connection.

Figure 5.8 shows the passive pressure distribution across the 45° skewed abutment from the field tests performed by Smith (2014). After an initial comparison of these differing plots, it appears that the computer model significantly over predicts the pressure. However, after applying the factor of 0.707 to account for the angle of the longitudinal pressure against the backwall (as previously discussed) the maximum and minimum values reduce to approximately 5,600 psi and 4,200 psi, respectively. These values also correspond to a deflection of about 3.5 inches in the calibrated models versus a deflection of 3 inches from the field test. Comparing the model values of about 5,600 psi and 4,200 psi to the field test values of about 4,200 psi and 3,500 psi for the obtuse and acute ends, respectively, the field test produced pressures about 17 to 25% lower than the model values. This gap would likely narrow if the tests were measured with the same abutment deflection.

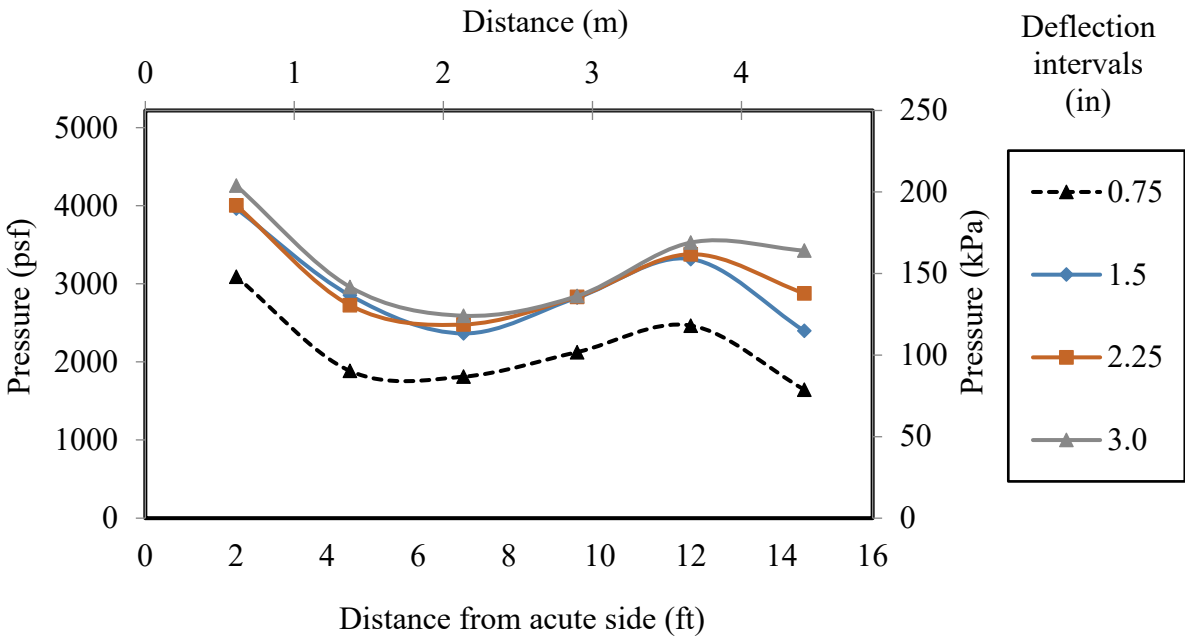

Figure 5.8. Passive pressure distribution across 45° skewed abutment (Smith 2014).

5.1.6 Wingwall Deflection

The wingwall deflection for both the 0° and 45° skew field tests are shown in Figure 5.9. The deflections of the wingwalls in the finite element study were essentially 0. The relative deflections from the end of the wingwall to the wingwall-abutment connection were 0.036 and 0.038 inches for the 0° skew model and 0.024 and 0.102 inches for the 45° skew model for the west and east wingwalls, respectively. In contrast, deflections of 0.25 to 0.5 inch were measured in the field tests. This discrepancy is likely due to not being able to correctly model the wingwall connections. In the field test, the reinforced concrete wingwalls were bolted to the abutment walls which provided much more rotational flexibility in comparison to the computer models where the connection was modeled monolithically with the abutment.

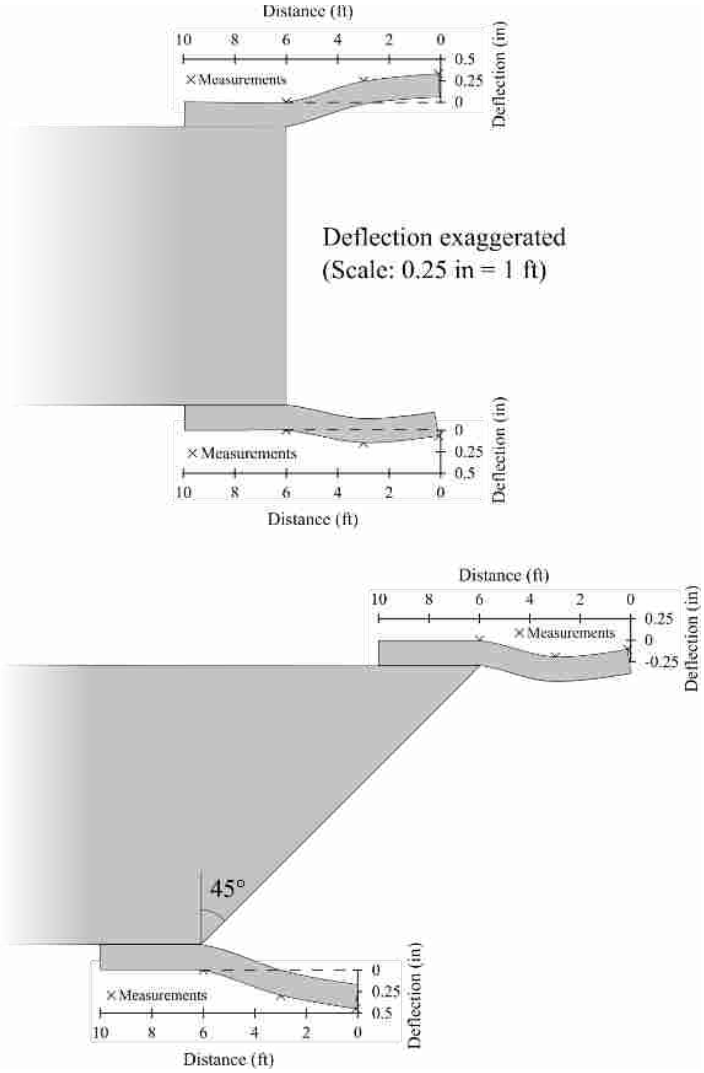

Figure 5.9. Deflection of 0° and 45° skew abutment field tests performed by Smith (2014).

5.1.7 Wingwall Pressure Distribution

As the abutments are displaced into the soil mass, the soil can be displaced in one of a few directions. It can displace longitudinally (in the "y" direction, Section 5.1.2) and compress the soil behind it, or heave (Section 5.1.4), or displace laterally. As the soil displaces laterally, the mass presses against the wingwalls and creates the pressure distributions shown in Figure 5.10 and Figure 5.12. For comparison, the pressure distributions on the wingwalls produced by the finite element models are shown below in Figure 5.11 and Figure 5.13.

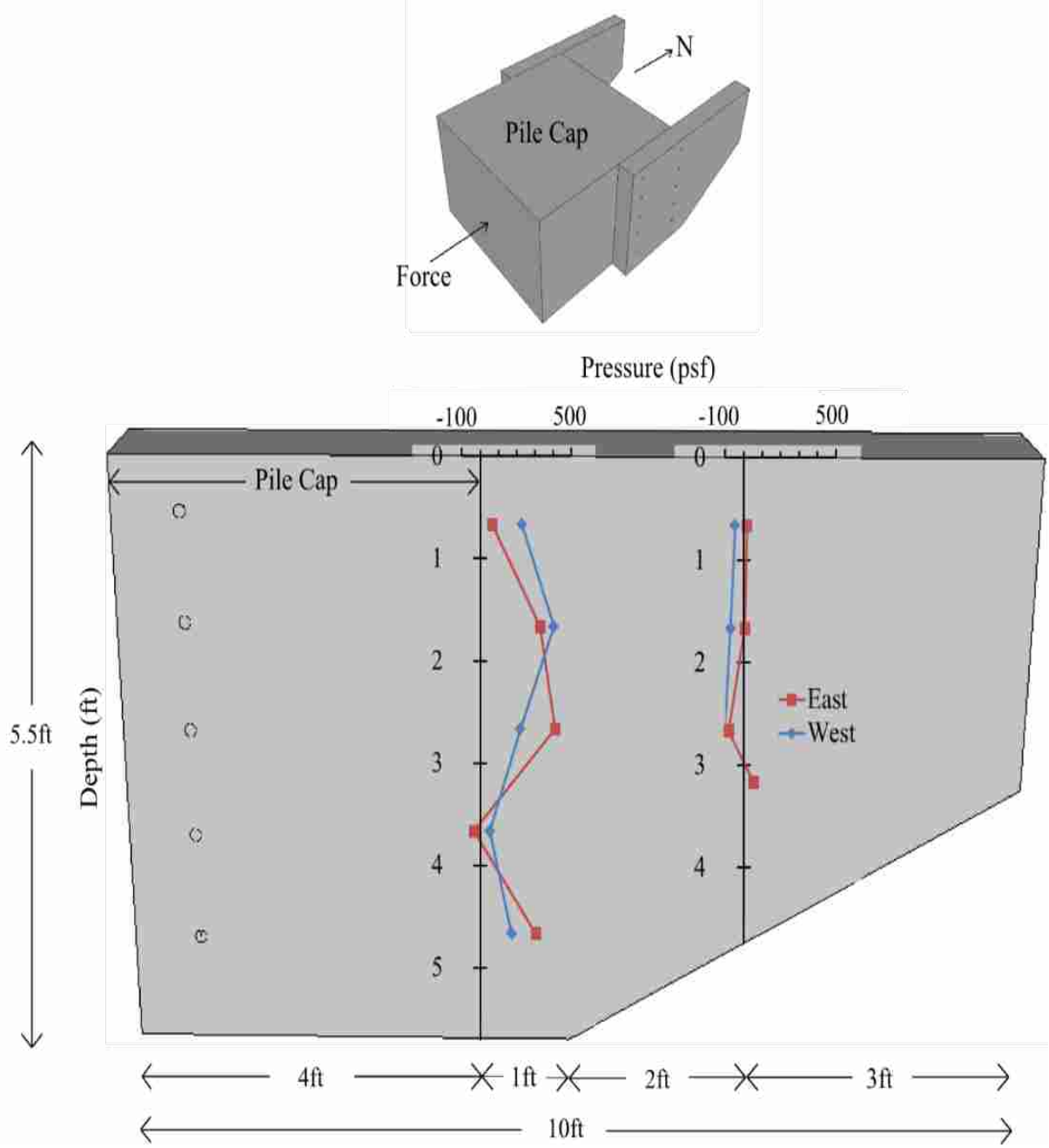

Figure 5.10. Soil pressure on the 0° skew abutment field tests performed by Smith (2014).

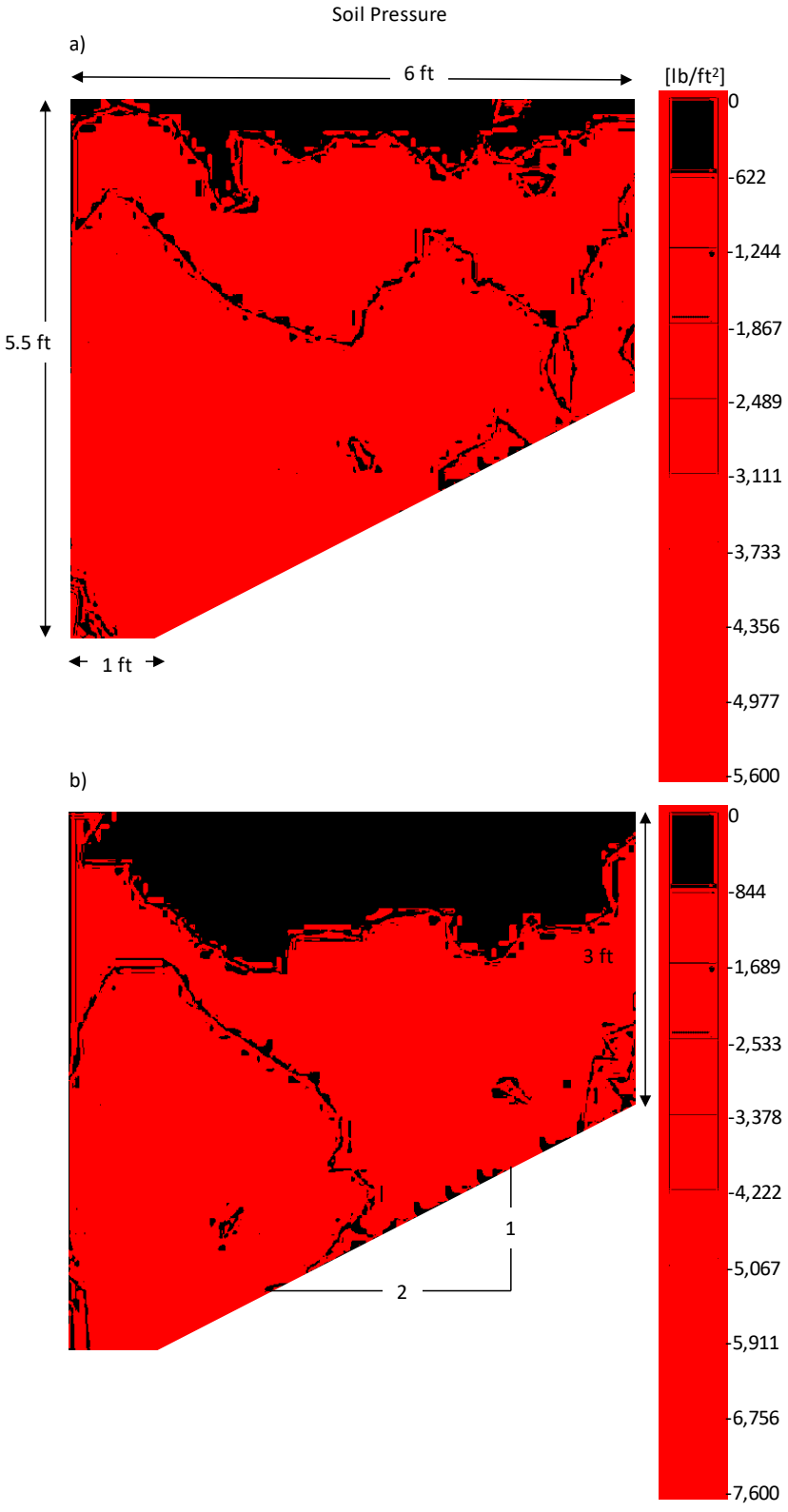

Figure 5.11. Soil pressure developed in west (a) and east (b) wingwall of the 0° skew model.

Figure 5.10 and Figure 5.11 show the soil pressure developed on the wingwalls due to the displacement of the abutment into the backfill soil for the 0° skew field test and the calibrated computer model, respectively. This result was derived by taking a vertical slice through the soil mass at an approximately 1-inch offset from the wingwalls (into the interior soil mass) and by plotting the stress in the lateral ("x") direction. The results from the finite element models for the 11-foot wide abutment significantly over-predict the measured values of the soil pressure acting on the wingwalls. The 0° skew model produces pressures up to about 3,000 psf on the lower half of the wingwall near the connection with the abutment versus only about 500 psf for the field tests. This is likely a result of the higher rotational stiffness of the wingwall connection in the computer model that reduced the lateral wingwall displacements, thereby increasing earth pressure.

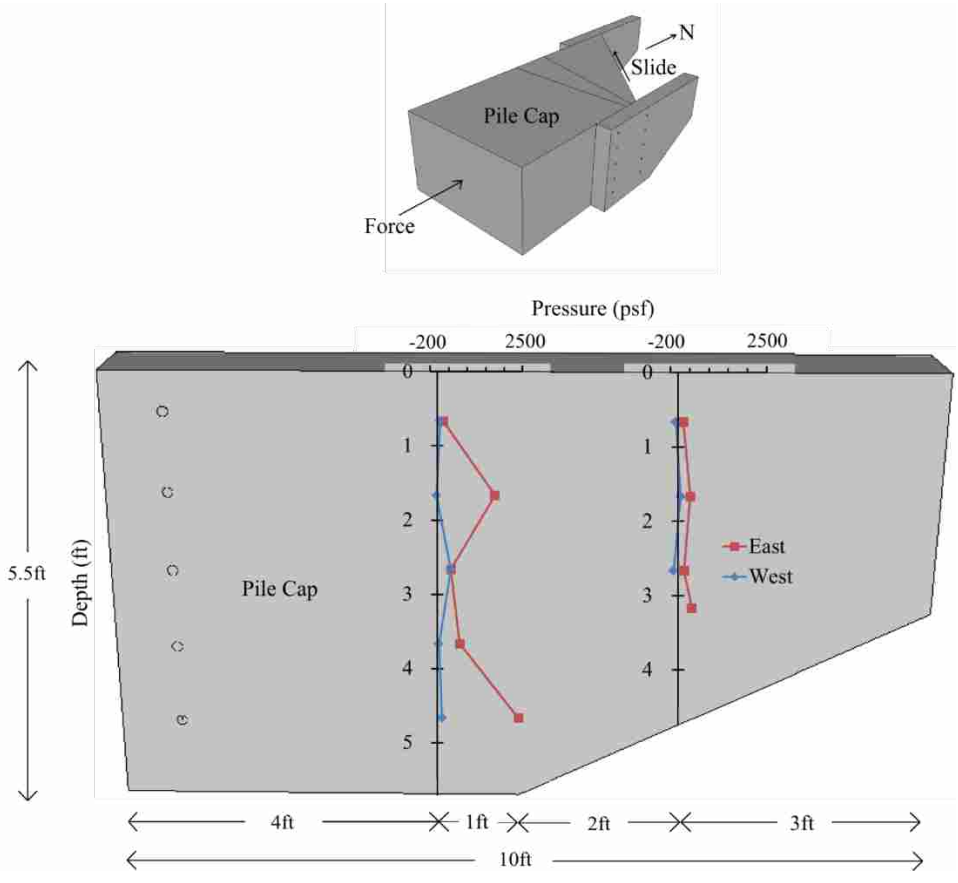

Figure 5.12. Soil pressure on the 45° skew abutment field tests performed by Smith (2014).

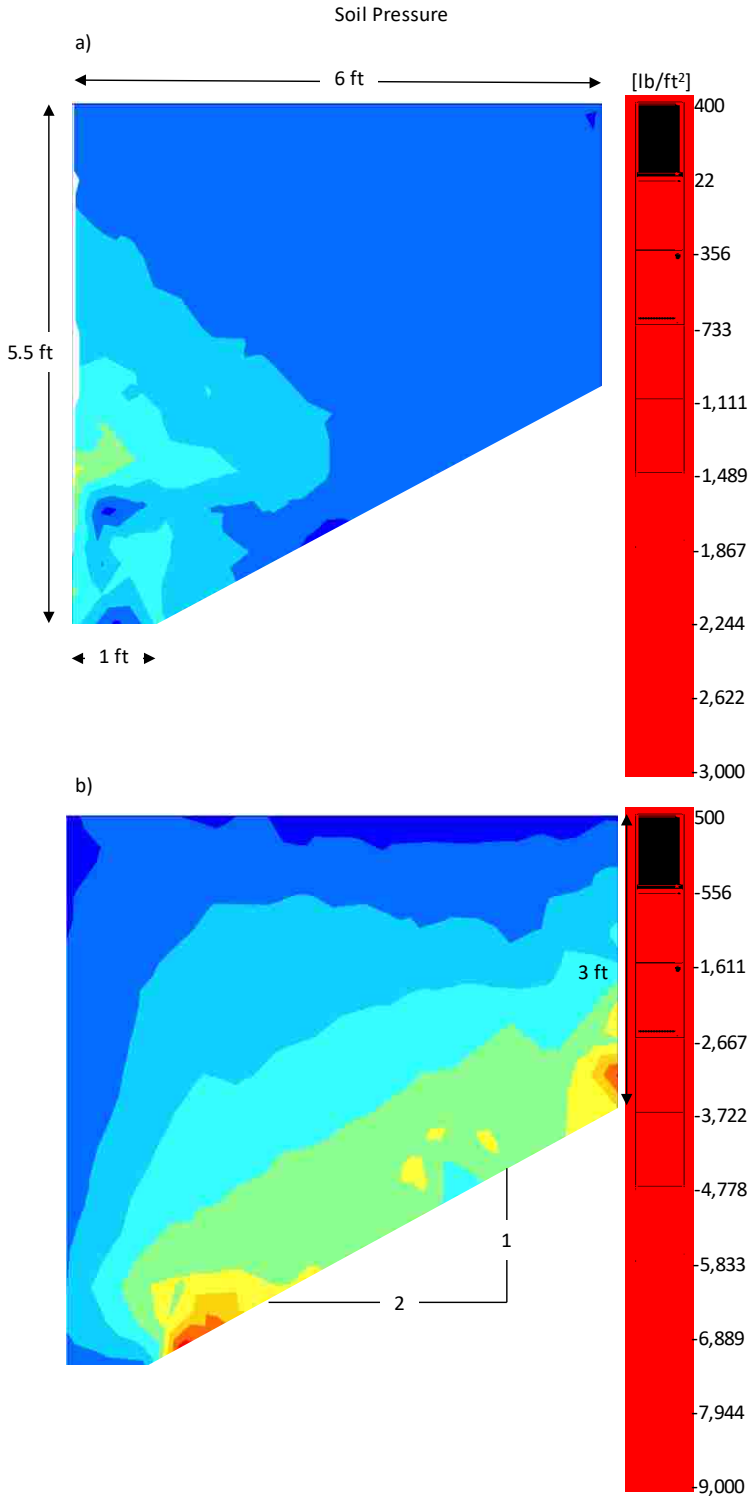

Figure 5.13. Soil pressure developed in west (a) and east (b) wingwall of the 45° skew model.

Figure 5.12 and Figure 5.13 show the soil pressure that develops along the wingwalls due to the displacement of the abutment into the backfill for the 45° skew field test and the calibrated computer model, respectively. This result was derived by taking a vertical slice through the soil mass at an approximately 1-inch offset from the wingwalls (into the interior soil mass) and by plotting the stress in the lateral ("x") direction.

The results from the finite element model for the 11-foot abutment appear to slightly over predict the measured values of the soil pressure acting on the wingwalls. The 45° skew model produces up to about 1,100 psf of pressure on the west wingwall and up to about 5,000 psf on the east wingwall (about 4 to 5 times larger) versus about 1,000 psf and 2,500 psf for the west and east wingwalls, respectively for the field tests. The higher pressure on the east wall develops because the abutment is sliding towards the west. The 45° skew model also shows a differing pressure distribution for the east wingwall relative to the other three wingwalls evaluated. It appears the pressure distribution is extended out along the bottom portion of the wingwall, which is likely caused by the soil pocket that has previously been discussed. These results may be useful in re-allocating reinforcing steel in wingwalls for skewed abutments.

5.1.8 Wingwall Bending Moments

As the abutment is loaded into the soil mass, the soil is displaced vertically (heave), longitudinally (compacting the soil behind it), and then laterally into the wingwalls causing deflection as discussed in Section 5.1.6. This lateral load into the wingwalls produces the bending moments that must be accounted for in design. The results of the field tests are shown in Figure 5.14 and Figure 5.16 versus the finite element models shown in Figure 5.15 and Figure 5.17.

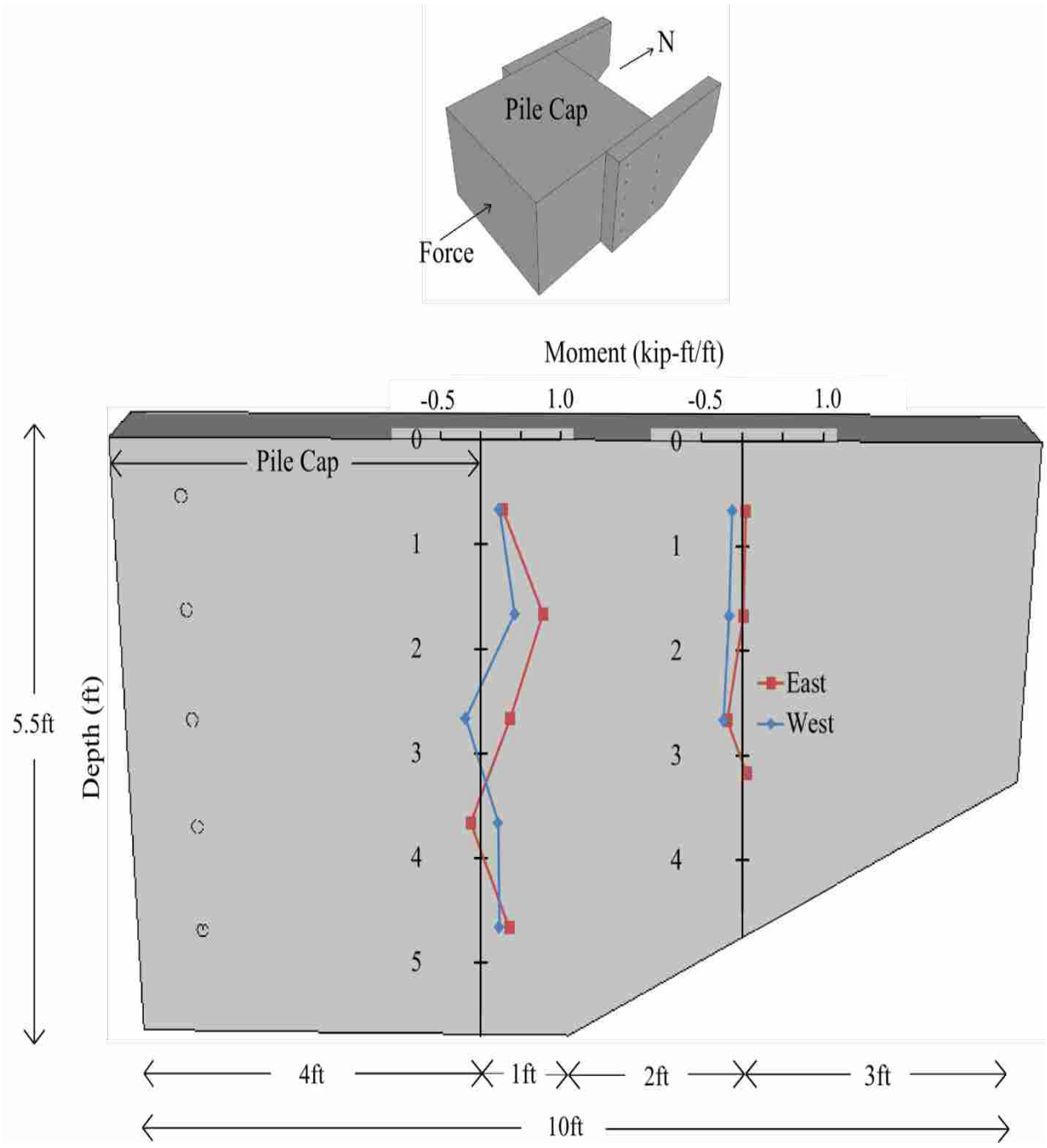

Figure 5.14. Bending moments on east and west wingwalls for 0° skew field test (Smith 2014).

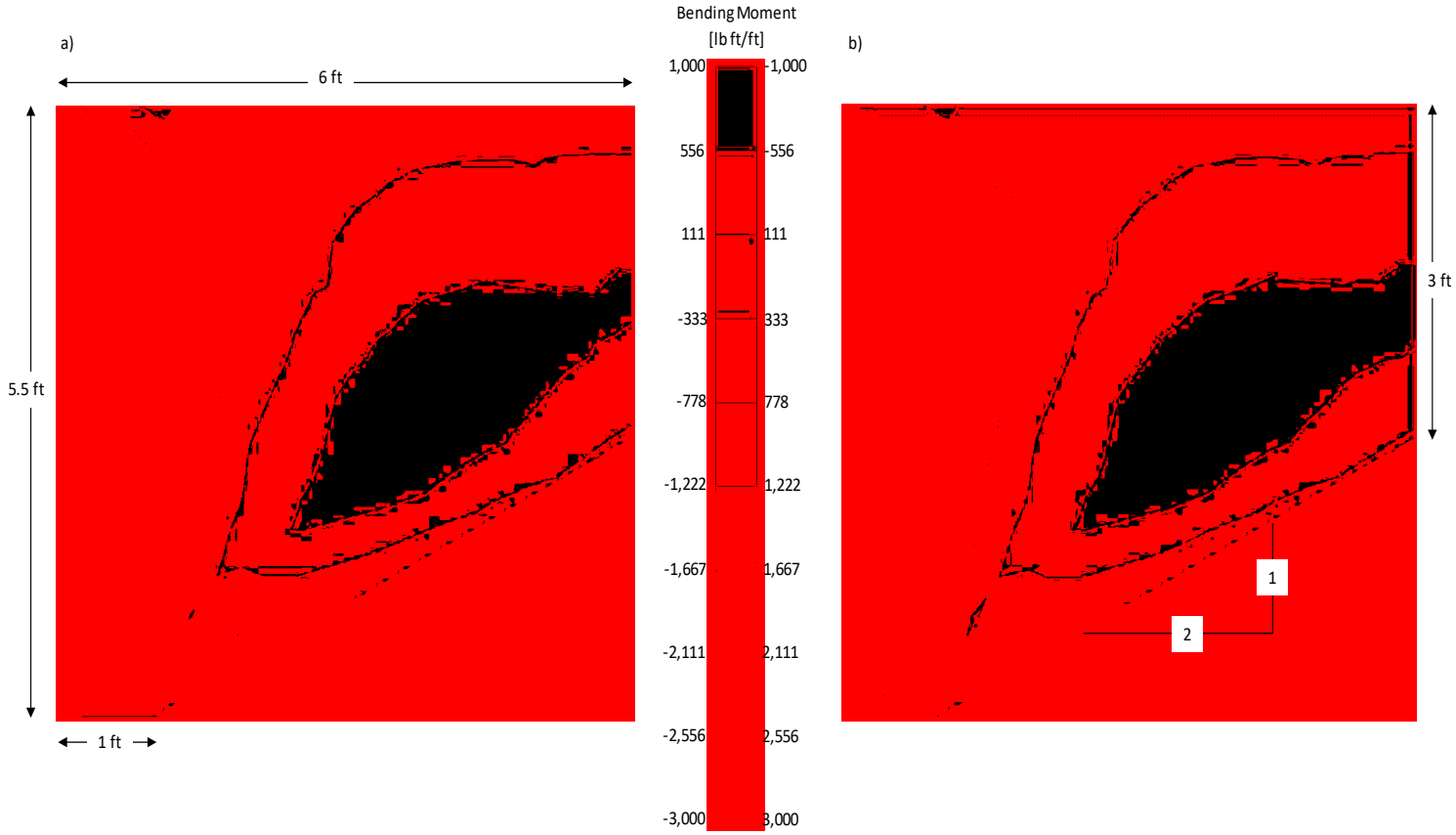

Figure 5.15. Bending moment developed in west (a) and east (b) wingwall of the 0° skew model.

Figure 5.14 and Figure 5.16 show the bending moment developed on the wingwalls due to the displacement of the abutment into the backfill soil for the 0° skew field test and the calibrated computer model, respectively. This result was derived by selecting the wingwalls and by plotting the bending moment about the abutment-wingwall connection ("z" axis).

The field tests performed by Smith (2014) show a maximum value of approximately 0.8 to 0.9 kip-ft/ft of wall or about 800 to 900 lb-ft/ft in comparison to maximum values of up to about 3,000 lb-ft/ft for the computer model. The maximum values are significantly overpredicted in the finite element model, but produce better agreement throughout the remainder of the wingwall with bending moments on the order of 500 lbft/ft to -500 lbft/ft. The model depicts the highest values near to or slightly above the midpoint of the abutment wingwall connection and also depicts comparable (but opposite) bending moments for the west and east wingwalls, which is consistent with the field testing.

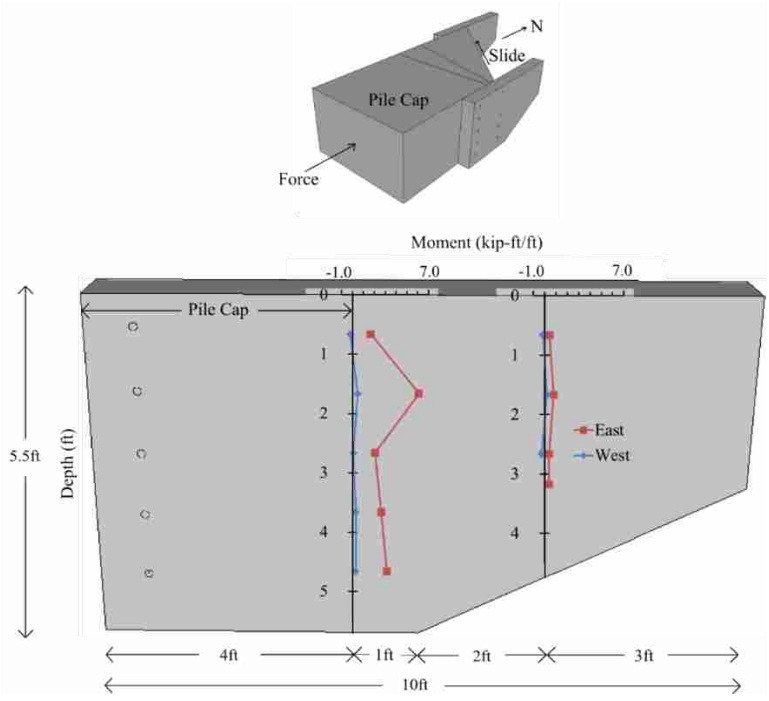

Figure 5.16. Bending moments on east and west wingwalls for 45° skew field test (Smith 2014).

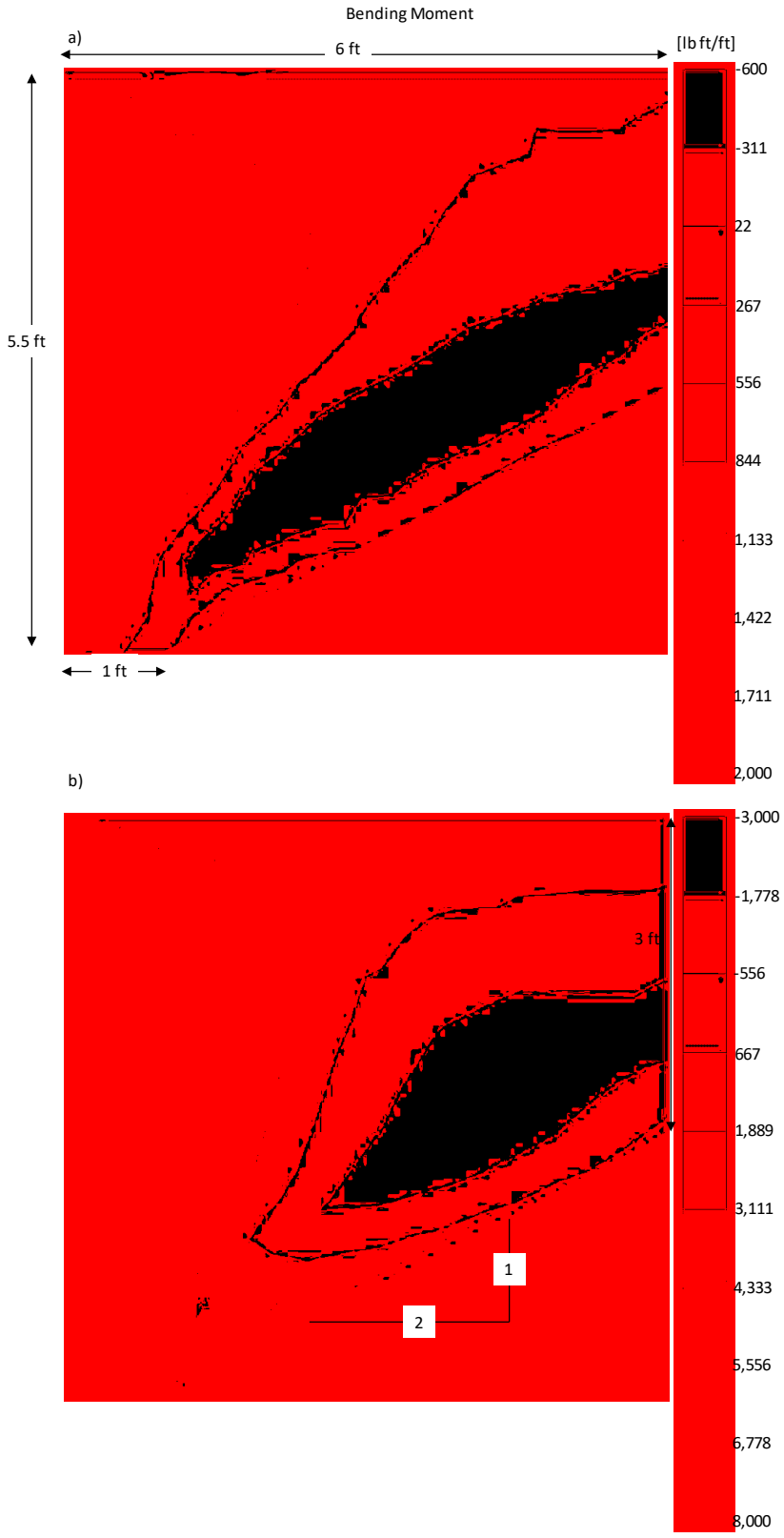

Figure 5.17. Bending moments developed in west (a) and east (b) wingwalls of the 45° skew model.

Figure 5.16 and Figure 5.17 show the bending moment developed on the wingwalls due to the displacement of the abutment into the backfill soil for the 45° skew field test and the calibrated computer model, respectively. This result was derived by selecting the wingwalls and by plotting the bending moment about the abutment-wingwall connection ("z" axis).

The field tests performed by Smith (2014) for the 45° skew abutment show a maximum value of less than approximately 1 kip-ft/ft for the west wingwall (acute abutment-wingwall connection) and approximately 7 kip-ft/ft for the east wingwall (obtuse abutment-wingwall connection). The finite element model also produces significantly larger bending moments in the east wingwall of up to approximately 8,000 lbft/ft (8 kipft/ft) versus up to approximately 2,000 lbft/ft (2 kipft/ft) on the east wingwall. This shows that the maximum values of the bending moment for the west and east wingwalls in the finite element model have relatively good agreement with the field tests and were about 4 times larger in the model versus about 7 times larger for the field tests. In addition, the model again depicts the highest values near the midpoint of the abutment wingwall connection.

This information is valuable to the engineering community as it provides insight into regions of the abutment wingwall connection that will need to be able to resist stronger bending moments. This is true particularly on the obtuse side of skewed abutments (where the soil mass is trapped by the angle of the abutment and adjacent wingwall). The bending moments are on the order of 5 to 7 times greater on the obtuse side based on the finite element and field tests, respectively. Therefore, after additional study engineers may be able to redesign the abutment wingwall connection.

5.2 Two-Lane Model

The Two-lane model was developed to be wide enough to accommodate two 12-ft lanes, a 4-ft inside shoulder, and a 10-ft outside shoulder for a total width of 38-ft. The backfill on both sides of the abutment tapers down at a 2H:1V slope until the backfill is level with the base of the abutment. The model extends a total of 21-ft on either side of the abutment and extends a minimum of 25 feet beyond the abutment backwall to provide adequate space for the log spiral failure surface to develop. The models for the 0° and 45° skew simulations are shown in Figure 5.18 and Figure 5.19, respectively.

The soil properties, wall properties, and soil-wall interface properties used for the 38-ft wide model are the same as those previously described for the 11-ft wide model in Chapter 4.

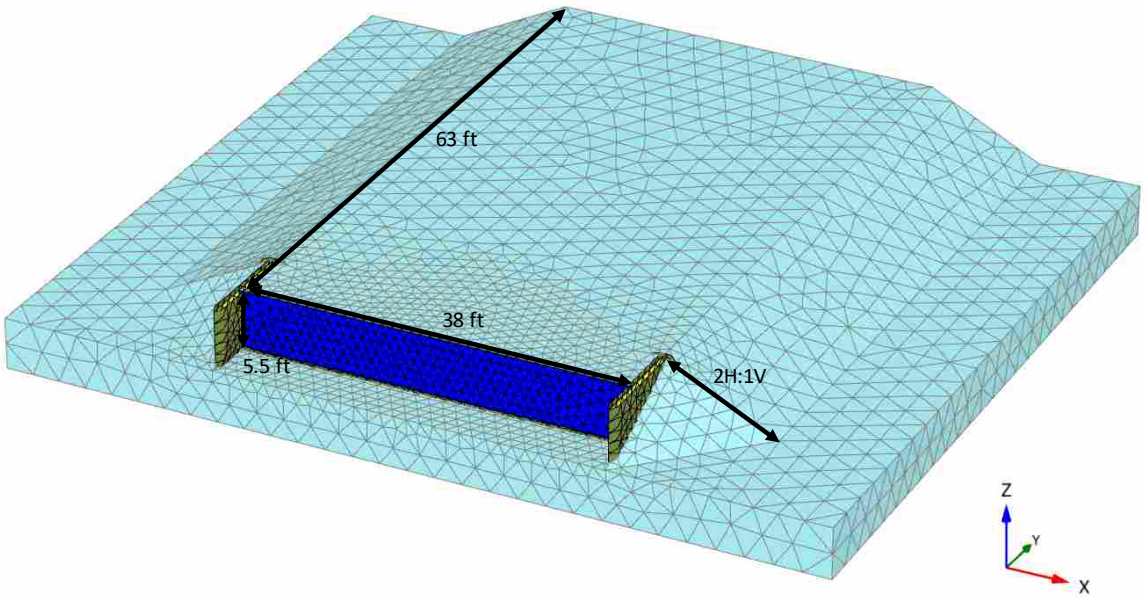

Figure 5.18. Generated mesh for 38-foot 0° skewed abutment.

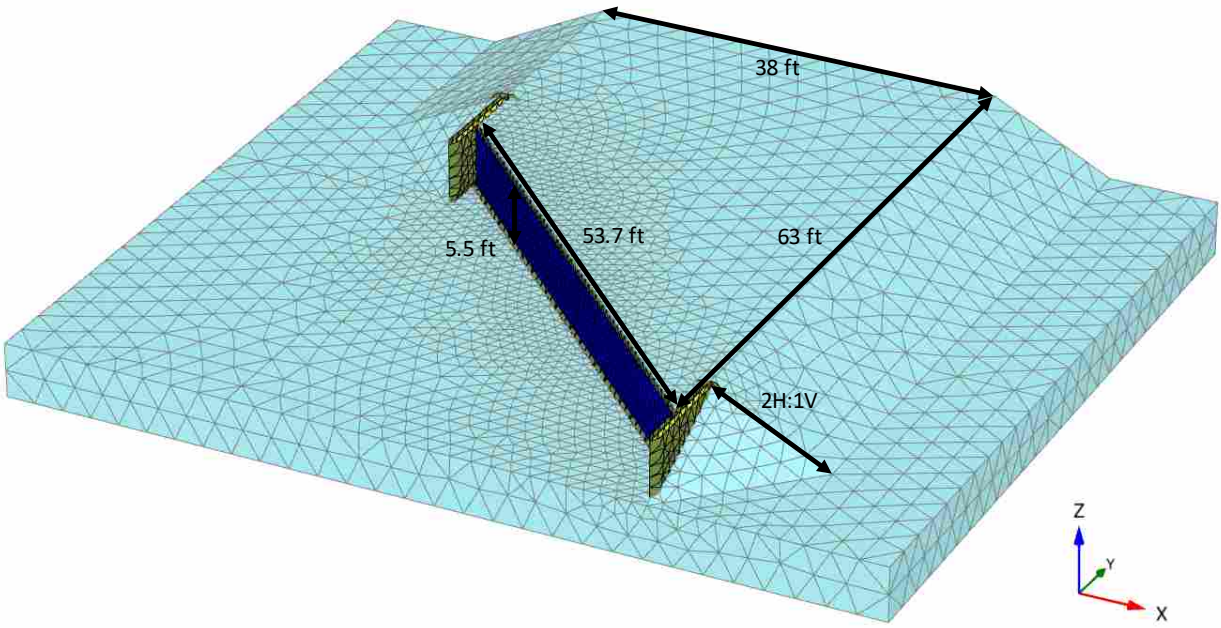

Figure 5.19. Generated mesh for 38-foot 45° skewed abutment.

Care was taken to simplify the models in order to reduce the run time of the calculation process. This was done by the use of mesh refinement. The pile cap was "refined," meaning that the mesh was densified immediately surrounding the abutment to provide more accurate results where stress concentrations were expected. Table 5.1 details the coarseness of each model mesh, the number of elements, nodes, and stress points involved, and the model dimensions.

Table 5.1. 38-Foot Abutment Finite Element Model Details

Model	*Coarseness*	*Elements*	*Nodes*	*Stress Points*	*Model Dimensions (x,y,z)*
0 Degree Skew	Very Fine	33,165	52,077	132,660	(80, 68, 10.5)
45 Degree Skew	Very Fine	44,094	67,791	176,376	(80, 68, 10.5)

5.2.1 Passive Force-Deflection Curves and Skew Reduction Factor

The passive force-deflection curves produced by the two-lane computer models are presented in Figure 5.20.

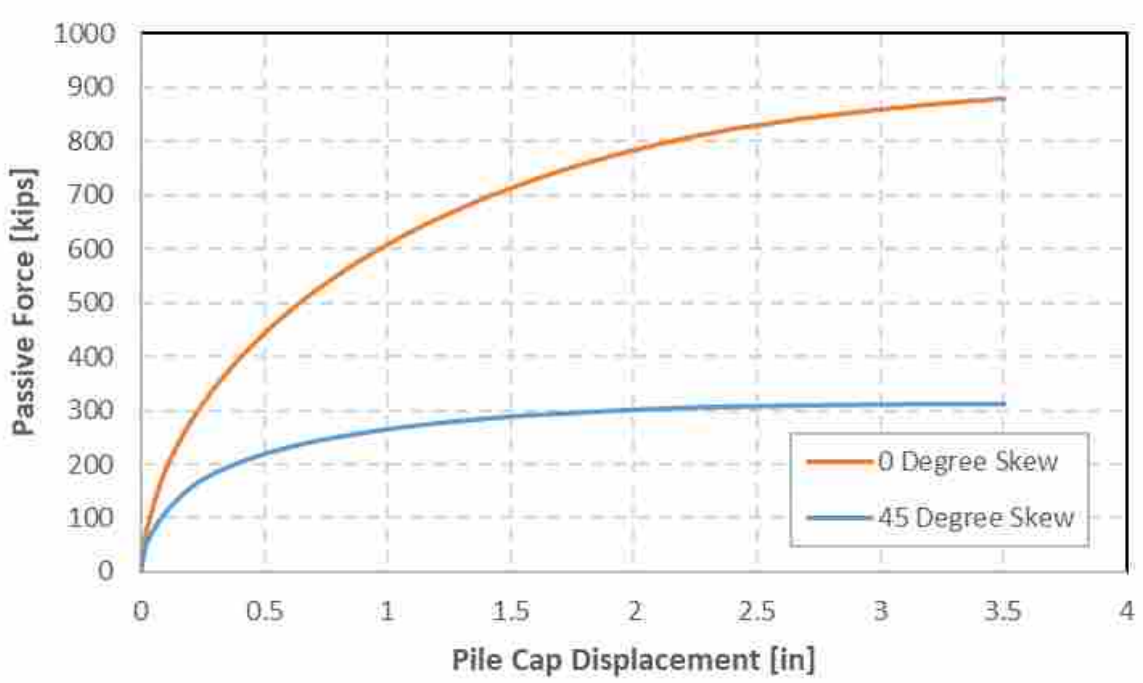

Figure 5.20. Passive force-deflection curves for 38-foot FEM models.

The peak passive force developed for the 38-foot wide 45° skewed abutment model is 311 kips ($P_{p\text{-}skew}$) relative to the peak passive force of 880 kips ($P_{p\text{-}no\ skew}$) for the 0° skewed abutment model. The passive force for the 45° skewed abutment was derived by taking the component of the maximum longitudinal force perpendicular to the abutment backwall (multiplying by a factor of 0.707) required to displace the 38-foot 45° skewed abutment 3½ inches. Based on the computed peak passive forces, the skew reduction factor, R_{skew}, was then determined to be 0.35 using equation (5-1) below.

$$R_{skew} = \frac{P_{p-skew}}{P_{p-no\ skew}} \tag{5-1}$$

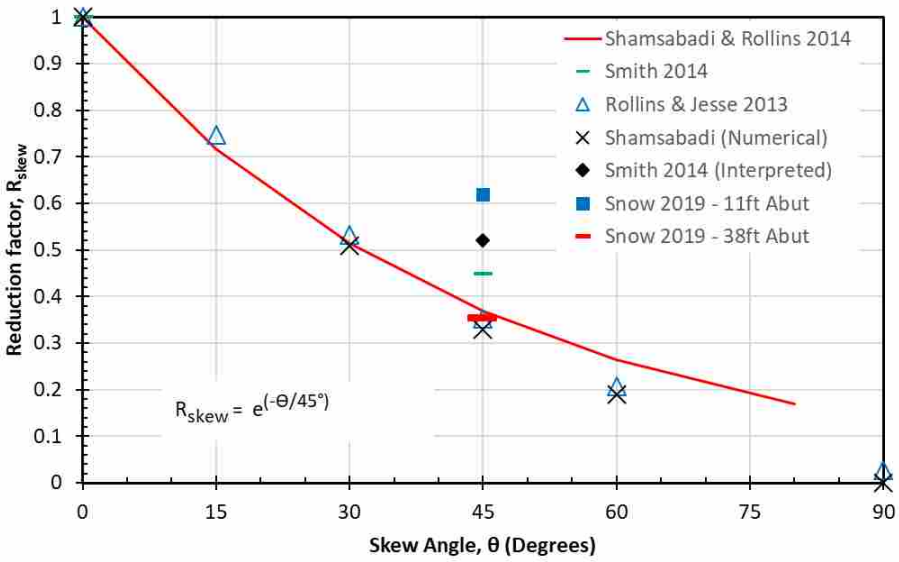

Figure 5.21. Skew reduction curve compared with skew reduction factor from field tests, along with reduction factors from the finite element models of 11 ft and 38 ft wide abutments.

Figure 5.21 shows the reduction factor, R_{skew}, relative to the design curve showing R_{skew} versus the skew angle of the abutment proposed by Shamsabadi and Rollins (2014). The skew reduction factor decreased from approximately 0.62 for the 11-ft wide abutment down to a value of 0.35 for the larger abutment width, which is in excellent agreement with the proposed skew reduction curve. Additional discussion regarding the reason for the improved agreement will be provided later. The improved agreement helps to confirm the accuracy of the proposed reduction curve for wider bridge abutments and may help to incorporate this reduction factor into standard engineering practice for bridges and overpass structures. By understanding the significant reduction in passive force resistance in backfill soils of skewed abutments, engineers can take appropriate measures to better design abutment backfills to reduce bridge collapse caused by earthquake loadings.

5.2.2 Longitudinal Displacement of Soil Backfill

Color contours of the longitudinal displacement ("y-direction") of the soil backfill for the 38-foot wide 0° and 45° skewed abutments are shown in Figure 5.22. For these plots, the longitudinal displacement of the abutment was 3.5 inches.

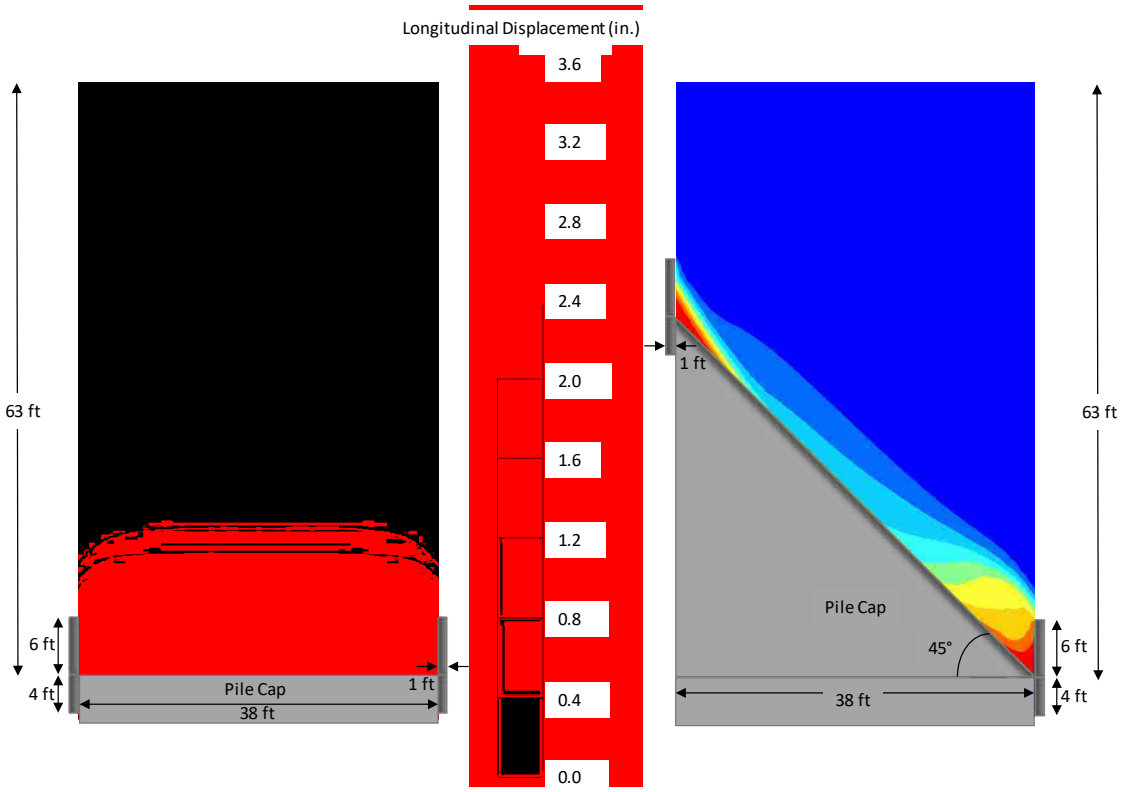

Figure 5.22. Longitudinal displacement of 38-foot wide 0° and 45°skew Plaxis models.

The results from this model show comparable displacement patterns to the field tests and the previous computer models. An important aspect to notice is that with the wider abutment, the influence of the constrained pocket of soil becomes less important relative to the overall length of the abutment backwall as shown in Figure 5.3 and Figure 5.22, respectively. For example, the pocket of soil moving with the abutment is about 6 ft. wide in both cases, but this 6 ft. length represents about 40% of the of the 15.5 ft. length of the backwall. In contrast, this 6 ft. length only represents about 11% of the 54 ft. length of backwall. The length of the soil pocket appears to be

controlled by the length of the wingwall. For the 11-ft wide abutment, the relatively long soil pocket has the effect of reducing the effective skew angle of the pile cap; however, for the 38-ft wide abutment, the pocket is too short to affect the effective skew angle.

5.2.3 Shear Failure Planes

Vertical cross sections were taken through the models in the longitudinal direction as depicted in Figure 5.23, to represent the shear failure planes that developed. Note that due to the 0° skew model being symmetrical, only one cross section was taken whereas cross sections were taken at both the acute and obtuse ends of the abutment for the 45° skew model.

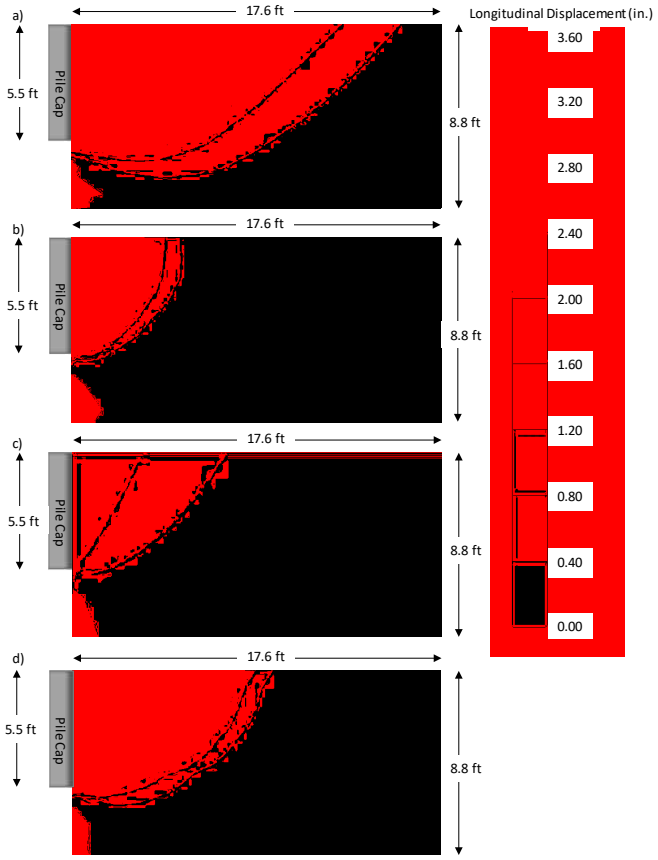

Figure 5.23. Longitudinal displacement showing shear planes of 0° skew model (a), 45° skew model (b) at acute end of abutment, (c) at center of abutment, and (d) at obtuse end.

As previously discussed in Section 5.1.3, cross section (a) is taken in the middle of the backwall of the 0° skew model as the results are essentially symmetrical. The cross sections (b) and (d) are taken approximately 1.2 inches inside the west and east wingwalls, respectively. Cross section (c) is taken in the middle of the backwall of the 45° skew model. This plot shows the shape of the shear failure planes for both cases and again confirms that they are best approximated by a log-spiral curve as previously predicted.

It is important to note that the length of the shear failure plane varies in each case. The acute side of the abutment for the 45° skew model produces the shortest shear failure plane and ultimately the least amount of displacement. For the case of the 38-foot wide abutment, the displacement of the obtuse end of the abutment of the 45° skew model is less than that produced by the same obtuse end of the abutment on the 11-foot calibrated model. This further shows that as the abutment width increases, the influence of the wingwalls on the longitudinal backfill displacement is reduced and the pocket of soil trapped by the wingwall and obtuse end of the abutment. In addition, in the 38-foot case, the 0° skew model produced the highest displacement, likely due to constraint from the wingwalls. As previously discussed, this relationship is important to engineers as this pocket of soil is essentially acting as an extension of the abutment.

5.2.4 Soil Heave

Color contours of the soil backfill heave for the 38-foot abutment models are illustrated in Figure 5.24 at the maximum backwall displacement of 3.5 inches.

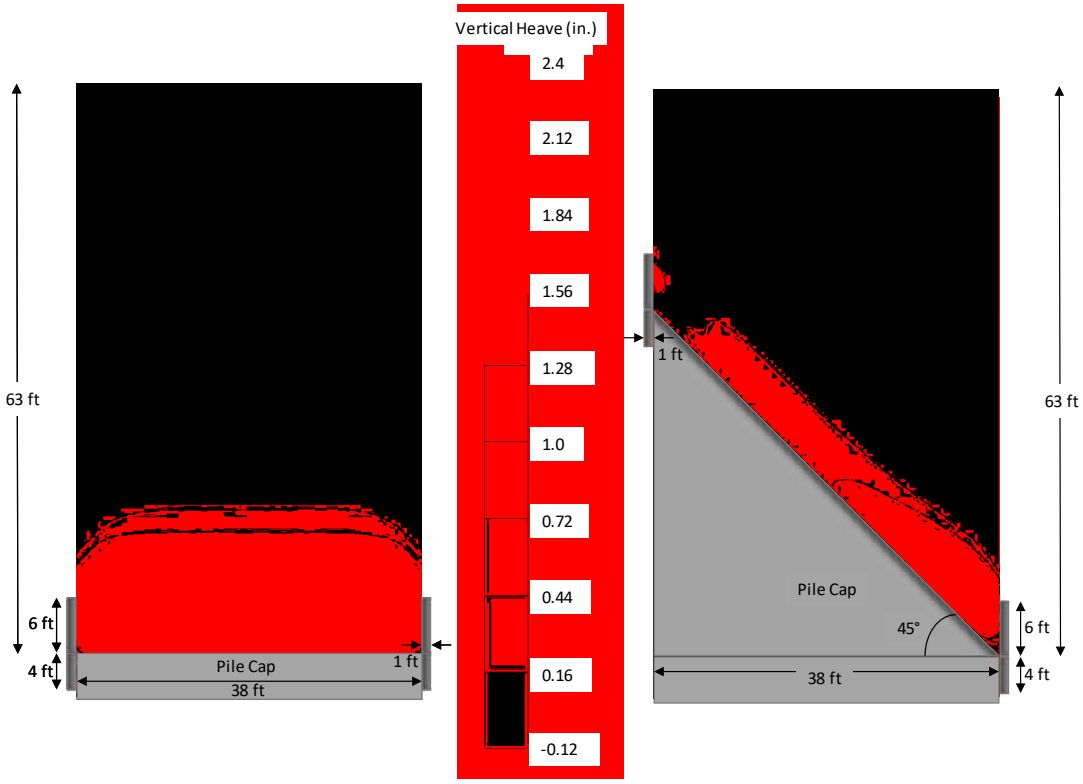

Figure 5.24. Heave for 0° and 45° 38-foot skewed abutment models at longitudinal abutment displacement of 3.5 inches.

Figure 5.24 displays the magnitude of heave, or vertical movement, of the soils caused by the displacing of the abutment into the backfill soil. For the 38-foot abutment case, both the 0° and 45° skew models produce up to approximately 2 to 2.4 inches of heave. In comparison to the 11-foot abutment results shown in Figure 5.6, the heave patterns look relatively similar for the 0° skew model. For the 45° skew model, the increased width of the abutment reduces the amount of heave along the abutment backwall as the heave is primarily located around the obtuse end of the abutment and the trapped soil pocket.

5.2.5 Backwall Pressure Distribution

The pressure distributions along the face of the abutment backwall for the 0° and 45° 38-foot skewed abutment models are shown in Figure 5.25.

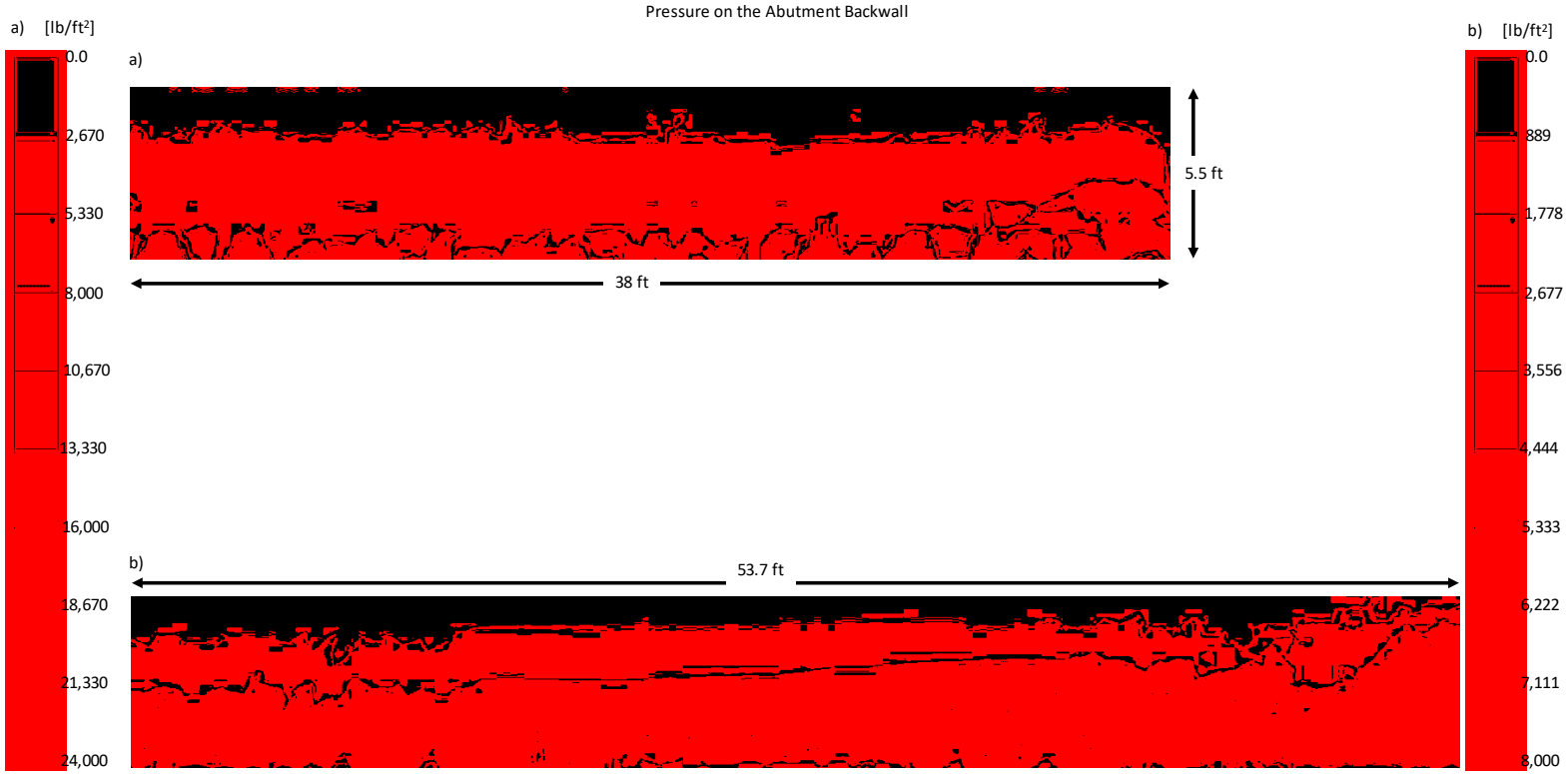

Figure 5.25. Soil pressure on the 38-foot abutment backwall for the 0° (a) and 45° (b) skew calibrated models.

Figure 5.25 shows the magnitude of the pressure acting longitudinally ("y" direction) on the abutment backwall of the 0° (a) and 45° (b) 38-foot skewed abutment models. These results were derived by taking vertical slices through the soil mass at an approximately 1-inch offset from the abutment backwalls. It is important to note that while the plots represent the pressure acting in the longitudinal direction, the backwall for the 45° skew model is oriented at a 45° angle from the longitudinal pressure. To accurately represent the backwall pressure of the 45° skew backwall, the contours of Figure 5.25(b) would need to be reduced by a factor of 0.707.

As might be expected, the figure shows that the pressure is increasing towards the bottom of the abutment. For the 45° skew backwall it also shows that the corner with the acute abutment-wingwall connection experiences significantly less soil pressure buildup (a reduction of approximately 50% or more) with respect to the obtuse abutment-wingwall connection having a magnitude of generally up to about 1,000 to 3,500 psf versus about 5,000 to 7,000 psf for the obtuse abutment-wingwall connection.

5.2.6 Wingwall Deflection

As previously stated, the deflections produced by the wingwalls in the calibrated finite element model were essentially 0 and are similar for the 38-foot abutment. The relative deflection from the end of the wingwall to the wingwall-abutment connection were -0.022 and 0.022 inches for the 0° skew model and -0.025 and -0.12 inches for the 45° skew model for the west and east wingwalls, respectively. This discrepancy is likely due to not being able to correctly model the wingwall connections. In the field test, the reinforced concrete wingwalls were bolted to the abutment walls which provided much more rotational flexibility in comparison to the computer models where the connection was modeled monolithically with the abutment.

5.2.7 Wingwall Pressure Distribution

The pressure distributions on the wingwalls produced by the 38-foot wide abutment finite element models are shown in Figure 5.26 and Figure 5.27.

Figure 5.26 and Figure 5.27 show the soil pressure developed on the wingwalls due to the displacement of the abutment into the backfill soil for the 0° skew field test and calibrated model, respectively. As previously stated, this result was derived by taking a vertical slice through the soil mass at an approximately 1-inch offset of the wingwalls (into the interior soil mass) and by plotting the stress in the lateral ("x") direction.

The results of the finite element models for the 38-foot abutment appear to be consistent with the values produced by the 11-foot abutment models. The pressure distributions are very similar while the produced soil pressures appear slightly higher. The 0° skew models produce soil pressures of up to about 3,000 to 4,000 psf on the lower half of the wingwall near the connection with the abutment. The 45° skew models produces up to about 600 psf on the west wingwall (acute side of the abutment) and about 7,000 to 8,000 psf along the lower half of the east wingwall (obtuse side of the abutment). In comparison, the 45° skew 11-foot abutment model produces about 1,000 and 5,000 psf for the west and east wingwalls, respectively. This results in an increase in the soil pressure of about 35%.

As previously discussed, the results of the developed soil pressures along the wingwalls may be useful in re-allocating reinforcing steel in wingwalls for skewed abutments.

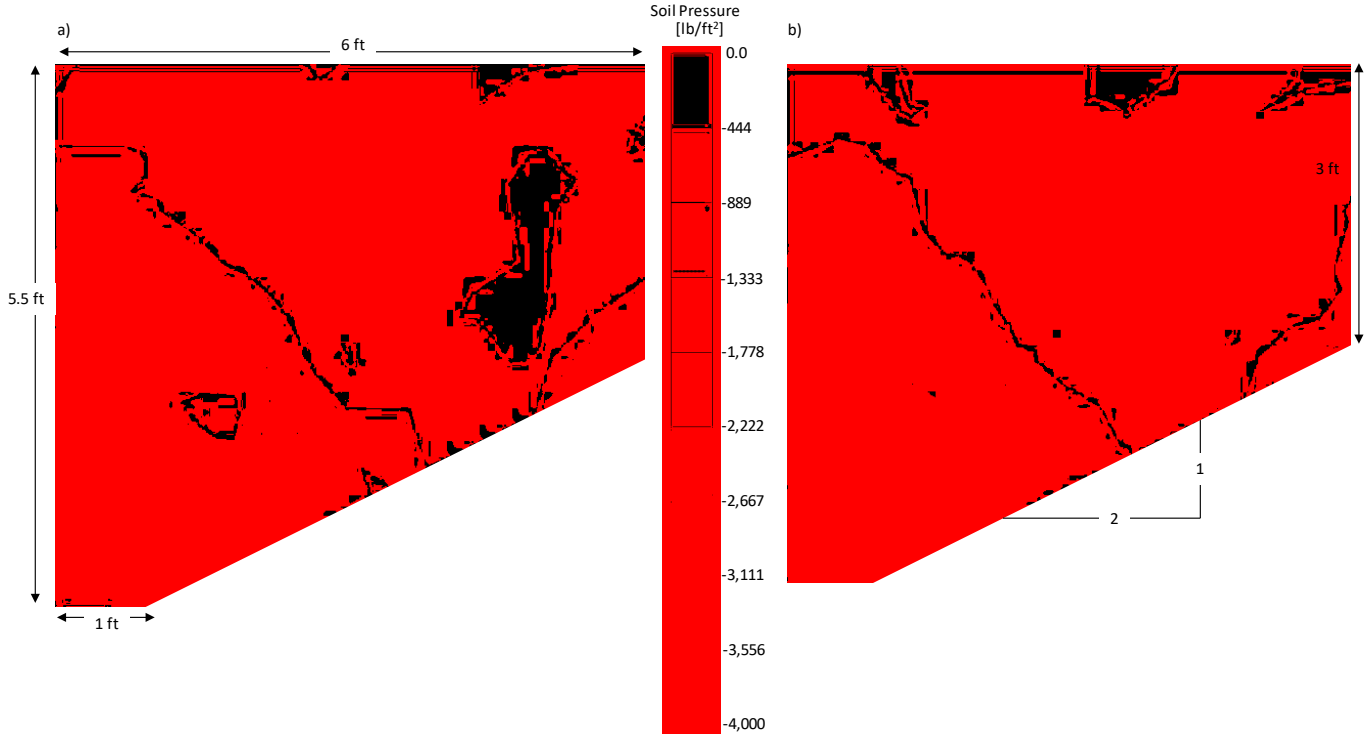

Figure 5.26. Soil pressure developed in west (a) and east (b) wingwall of the 0° 38-foot skewed abutment model.

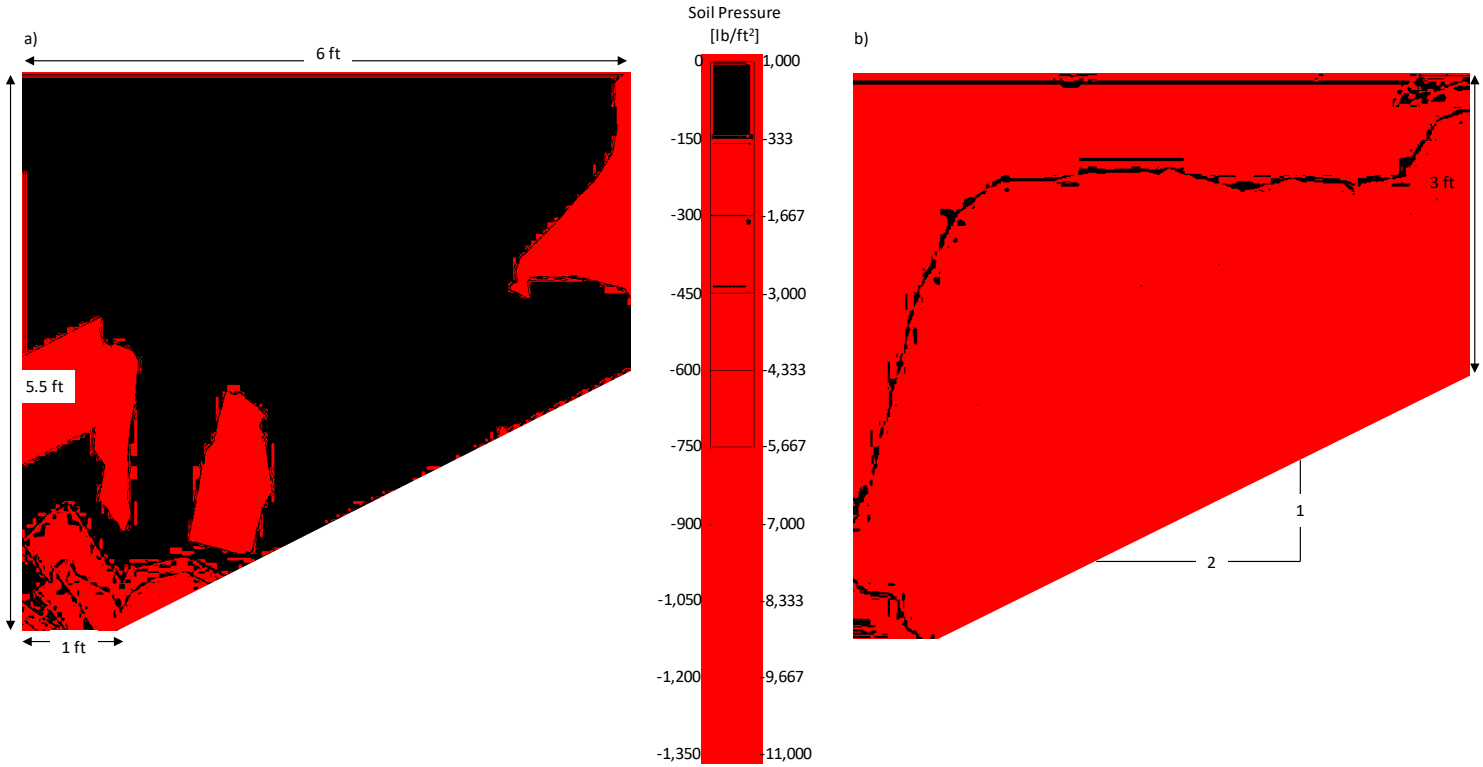

Figure 5.27. Soil pressure developed in west (a) and east (b) wingwall of the 45° 38-foot skewed abutment model.

5.2.8 Wingwall Bending Moments

The bending moment distributions on the wingwalls produced by the 38-foot wide abutment finite element models are shown below in Figure 5.28 and Figure 5.29.

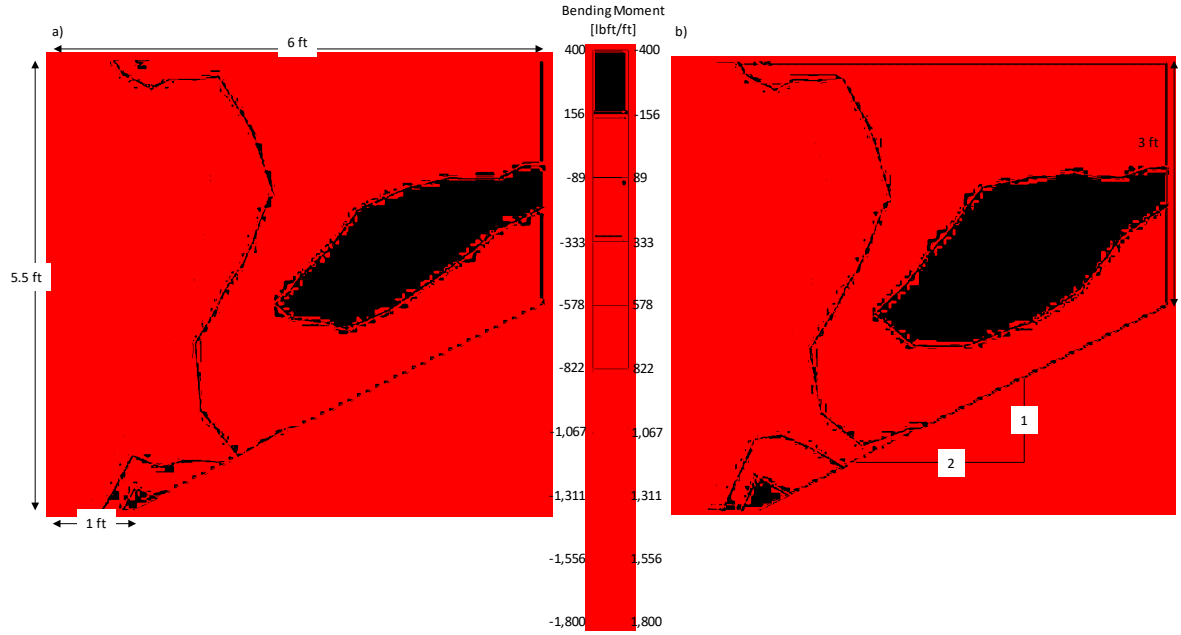

Figure 5.28. Bending moment developed in west (a) and east (b) wingwall of the 0° 38-foot skewed abutment model.

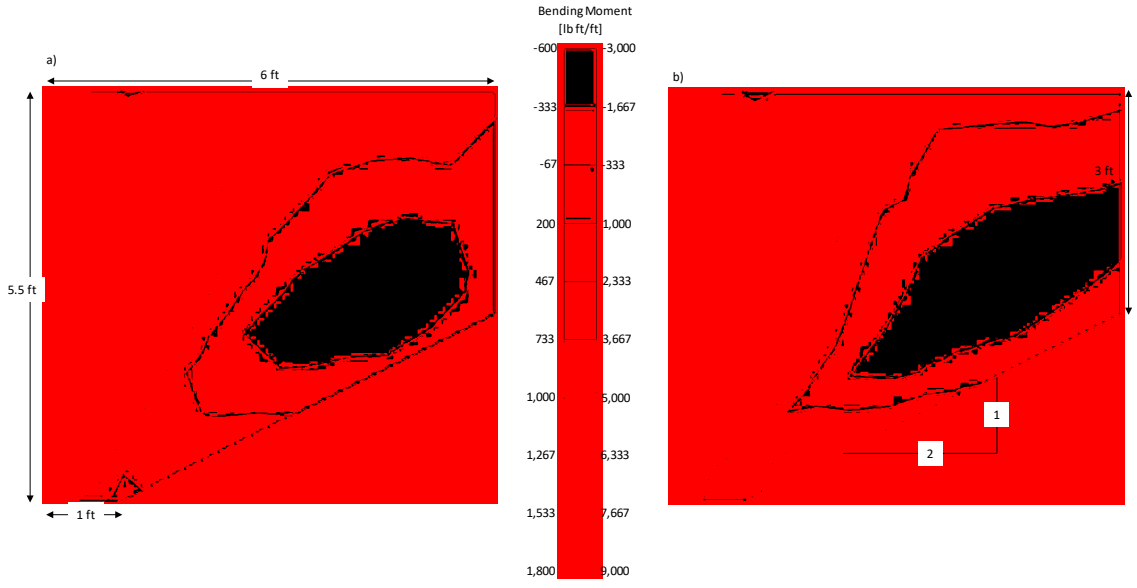

Figure 5.29. Bending moment developed in west (a) and east (b) wingwall of the 45° 38-foot skewed abutment model.

Figure 5.28 and Figure 5.29 show the bending moment developed on the wingwalls due to the displacement of the abutment into the backfill soil for the 38-foot abutment 0° and 45° skew models, respectively. This result was derived by selecting the wingwalls and by plotting the bending moment about the abutment-wingwall connection ("z" axis).

The 0° skew models produced approximately the same magnitude of bending moment of about 1,800 lb-ft/ft in opposite orientations, as expected. The 45° skew models produced approximately the same magnitude of bending moment of about of 1,800 lb-ft/ft on the west wingwall (acute side of the abutment). However, at the east wingwall (obtuse side of the abutment) the model produced approximately 5 times the bending moment at about 9,000 lb-ft/ft.

In comparison, the 11-foot abutment (calibrated) 0° and 45° skew models produce a larger bending moment for the wingwalls in the 0° skew model (3,000 lbft/ft versus 1,800 lbft/ft). This is likely due to the close proximity of the wingwalls relative to each other. In contrast, the 45° skew model for the 11-foot abutment produces a slightly higher moment about the west wingwall (2,000 lbft/ft versus 1,800 lbft/ft) and a slightly lower moment about the east wingwall (8,000 lbft/ft versus 9,000 lbft/ft). In this case, the effects of the confined soil have less influence because of the increased length of the wingwall for the 45° skew model (11-ft versus 15.6-ft) and the longitudinal offset of 11-ft from the start of each wingwall. These results illustrate that the abutment-wingwall connections on the obtuse side of skewed abutments will require significantly stronger connections as the bending moments developed are 4 to 5 times greater.

5.3 Two-Lane Model with Extended Wingwalls

As previously discussed, as the abutment was widened, the skew reduction factor (R_{skew}) decreased to 0.35 to be in excellent agreement with the proposed reduction curve. This is likely

due to the smaller influence of the soil pocket on the effective abutment skew angle. For the 11-foot abutment, the effective skew angle is approximately 30 versus approximately 40 for the 38-foot abutment. This suggests that increasing the length of the wingwalls (specifically on the obtuse side of the abutment) may increase the size of the soil pocket. This increase in size of the soil pocket would likely decrease the effective skew angle.

As such, an additional finite element model was developed with one variation to the previous two-lane model. The wingwalls extended 10 feet, rather than 6 feet, into the soil backfill. To account for this change in length, the wingwall slopes up at a slope of 9H:2.5V, rather than 2H:1V. This was done for simplicity and allowed the remaining wingwall dimensions to stay the same.

The passive force – deflection curves for this additional model are presented in Figure 5.30 and the resulting skew reduction factor is shown in Figure 5.31.

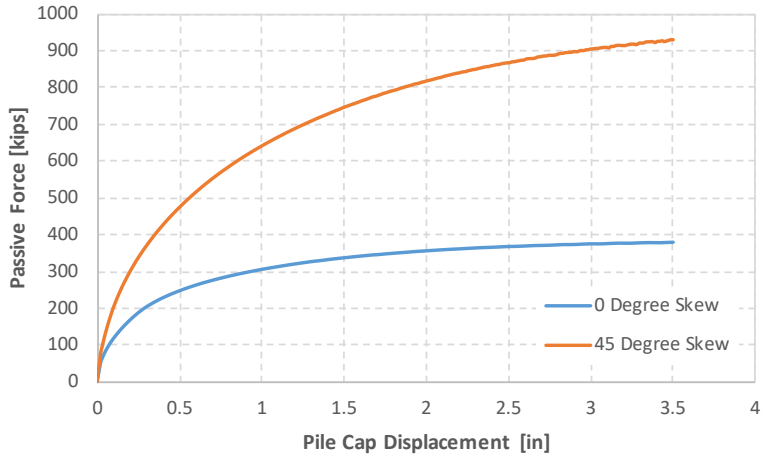

Figure 5.30. Passive force-deflection curves for 38-foot FEM model with wingwalls extended 10 feet into backfill.

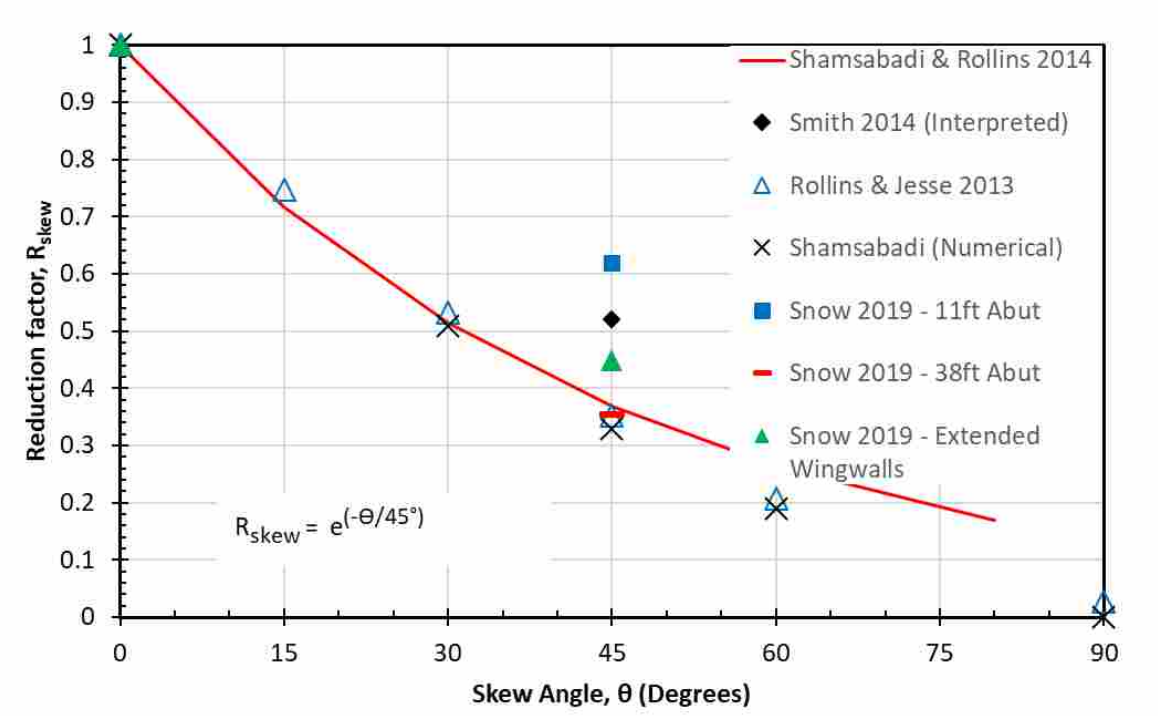

Figure 5.31. Skew reduction curve compared with skew reduction factor from field tests, along with reduction factors from the finite element models of 11 ft, 38 ft, and 38 ft wide abutments with extended wingwalls.

Figure 5.30 shows peak passive resistances of approximately 930 kips and 380 kips for the 0° and 45° skew FE models, respectively. These resistances were then used to calculate the skew reduction factor of 0.41 as shown in Figure 5.31. This result shows that by increasing the length of the obtuse wingwall, and thereby increasing the size of the entrapped soil pocket, the effective skew angle can be decreased. This decrease in the effective skew angle would then decrease the skew reduction factor by increasing the passive soil resistance. Further studies of this effect may be useful in determining if increasing the length of this obtuse wingwall would be a useful remediation tactic to prevent previously skewed bridges from being susceptible to failure.

6 CONCLUSIONS

The conclusions are based on the large-scale lateral load tests on abutments with longitudinal reinforced concrete (RC) wingwalls performed by Smith (2014) and the finite element models produced as part of this study.

1. The finite element models are generally consistent with the previous results obtained from the large-scale field tests performed by Smith (2014), the results obtained from numerical models developed by Shamsabadi et al. (2006), and small-scale lab tests by Jessee (2012) showing a significant reduction in peak passive force as skew angle increases (40 to 65% reduction for 45° skew).
2. A 54 to 57% reduction ($R_{skew} = 43\ to\ 46\%$) was measured by Smith (2014) compared to the recommended 65% reduction ($R_{skew} = 35\%$) for 45° skew. Based on further analysis of the large-scale test data, the reduction in peak passive force produced by large-scale field tests (Smith 2014) overestimated the reduction. Calculations in this study with the same data computes the reduction at 48% (R_{skew} = 52%) versus 54 to 57%. In order to obtain reasonable agreement with both the 0° and 45° field tests, the calibrated models over-predicted the passive force resistance by about 13% and thereby the reduction (38% or R_{skew} = 62%).

3. Passive force resistance for the wider, 38-foot abutment produced a reduction of approximately 65% (R_{skew} = 0.35), which is in excellent agreement with the proposed reduction curve by Shamsabadi and Rollins (2014).
4. The finite element models for the 45° skew showed a pocket of soil located between the obtuse side of the abutment and the wingwall that displaced the same magnitude as the abutment. However, the width of this pocket became smaller relative to the width of the abutment as the abutment became wider. Therefore, the effect of this pocket on passive force became much smaller as the abutment width increased. This pocket influenced multiple other aspects of this study including the development of the shear planes, soil pressures on the wingwalls and abutment backwalls, and bending moments.
5. The finite element models confirmed the finding by Smith (2014) that the passive failure surface for the RC wingwall case appears to develop a failure geometry that closely resembles a 2D, log-spiral failure geometry. In addition, the finite element study showed that length of the shear failure plane varied significantly based on the skew angle and the abutment width.
6. The calibrated finite element models produced similar heave results of about 2 inches in comparison to the large-scale field tests performed by Smith (2014). As the abutment widens, the magnitude of the heave remains approximately the same for the 0° skew model. For the 38-foot 45° skewed abutment model, the magnitude of the heave is the same as the other models but it acts over a much smaller area near the previously discussed soil pocket. The rest of the backfill of this model produced approximately ½ inch of heave or less.
7. The finite element model also showed increased soil pressures along the obtuse side of the abutment backwall due to the development of the soil pocket. These pressures were

typically highest along the lower half of the abutment backwall and were significantly higher (approximately 3 times or more) than the pressures experienced on other portions of the wall. This effect is also shown to a lesser degree on the edges of the abutment of the 0° models due to smaller pockets of soil being confined by the wingwall.

8. The finite element models confirmed the finding by Smith (2014) that the lateral soil pressures were significantly higher on the obtuse side wingwall compared to the wingwall on the acute side for the 45° skewed abutment (about 10 to 14 times greater). Soil pressure distributions acting on non-skewed wingwalls were similar in magnitude to those on the acute side wingwall on the 45° skewed abutment.
9. The finite element models generally confirmed that the maximum bending moment acting on RC wingwalls was measured at the abutment-wingwall connection and generally at the midpoint of the wall or higher (except for the wingwall attached to the acute side of the 45° skewed abutments). This is likely due to this wingwall experiencing the smallest magnitude of soil pressure. In addition, this study also confirms that for the 45° skewed abutment the maximum wingwall bending moment was approximately 4 to 5 times larger on the obtuse side of the abutment compared to the acute side (for both the 11-foot and 38-foot models). In comparison, the 45° skewed abutment field tests produced bending moments that were approximately 14 times larger on the obtuse side of the abutment compared to the acute side and 7 times larger compared to the maximum bending moment from the non-skewed abutment.
10. Increasing the length of the wingwalls on the two-lane (38-foot) FE model resulted in an increase in the size of the soil pocket and an increase in the peak passive resistance for the 45° model. This increase produced an R_{skew} of 0.41 versus 0.35. This suggests that

increasing the length of the wingwall on the obtuse side of the abutment may change the effective skew angle, thereby increasing passive resistance and stability of the bridge. Further studies of this effect may be useful in determining if increasing the length of this obtuse wingwall would be a useful remediation tactic to prevent previously skewed bridges from being susceptible to failure.

REFERENCES

AASHTO (2011). *Guide Specifications for LRFD Seismic Bridge Design*.

Apirakvorapinit, P., Mohammadi, J., and Shen, J. (2012). "Analytical Investigation of Potential Seismic Damage to a Skewed Bridge." *Practice Periodical on Structural Design and* Construction, 17(1), 5-12.

Apirakyorapinit, P., Mohammadi, J., and Shen, J. (2012). "Analytical Investigation of Potential Seismic Damage to a Skewed Bridge." *Practice Periodical on Structural Design and Construction*, 16(1), 5-12.

Caltrans, C. D. o. T. (2010). "Seismic Design Criteria, Version 1.6, November 2010." Division of Engineering Services, Office of Structure Design, Sacramento, California.

Christensen, D. S. (2006). "Full Scale Static Lateral Load Test of a 9 Pile Group in Sand." Master of Science, Brigham Young University, Provo, Utah.

Cole, R., and Rollins, K. (2006). "Passive Earth Pressure Mobilization during Cyclic Loading." Journal of Geotechnical and Geoenvironmental Engineering, 132(9), 1154-1164.

Coulomb, C. A. (1776). "Essai sur une application des règles de maximis & minimis à quelques problèmes de statique, relatifs à l'architecture." (microform, Microopaque), De l'Imprimerie Royale, Paris.

Douglas, D. J., and Davis, E. H. (1964). "The Movement of Buried Footings due to Moment and Horizontal Load and the Movement of Anchor Plates." *Geotechnique, London*, 14(2), 115-132.

Duncan, J., and Mokwa, R. (2001). "Passive Earth Pressures: Theories and Tests." Journal of Geotechnical and Geoenvironmental Engineering, 127(3), 248-257.

Duncan, J. M., and Chang, C. Y. (1970). "Nonlinear Analysis of Stress and Strain in Soils." *Journal of the Soil Mechanics and Foundations Division*, 96(5), 1629-1653.

Elnashai, A. S., Gencturk, B., Kwon, O.-S., Al-Qadi, I. L., Hashash, Y., Roesler, J. R., Kim, S. J., Jeong, S.-H., Dukes, J., and Valdivia, A. (2010). "The Maule (Chile) Earthquake of February 27, 2010: Consequence Assessment and Case Studies."

Franke, B. (2013). "Passive Force on Skewed Abutments with Mechanically Stabilized Earth (MSE) Wingwalls Based on Large-Scale Tests." M.S., Brigham Young University, Provo, Utah.

Guo, A. (2015). “Numerical Analysis of Passive Force on Skewed Bridge Abutments.” M.S., Brigham Young University, Provo, Utah.

Jessee, S. J. (2012). "Skew Effects on Passive Earth Pressures Based on Large-Scale Tests." M.S., Brigham Young University, Provo, Utah.

Johnson, S. R. (2003). "Static Lateral Load Testing of a Full-Scale Pile Group Spaced at 5.65 Pile Diameters."M.S. Thesis, Brigham Young University, Provo, UT.

Lemnitzer, A., Ahlberg, E., Nigbor, R., Shamsabadi, A., Wallace, J., and Stewart, J. (2009). "Lateral Performance of Full-Scale Bridge Abutment Wall with Granular Backfill." Journal of Geotechnical and Geoenvironmental Engineering, 135(4), 506-514.

Marsh, A. (2013). "Evaluation of Passive Force on Skewed Bridge Abutments with Large-Scale Tests." Master of Science, Brigham Young University, Provo, Utah.

Potyondy, J. G. (1961). "Skin Friction Between Various Soils and Construction Materials." Geotechnique, London, 11(1), 339-353.

Rankine, W. J. M. (1857). "On the Stability of Loose Earth." Philosophical Transactions of the Royal Society of London, 147(ArticleType: research-article / Full publication date: 1857 /), 9-27.

Reference Manual: PLAXIS 3D 2015; Edited by R.B.J. Brinkgreve; Delft University of Technology & PLAXIS b.v.; The Netherlands

Rollins, K. M., and Cole, R. T. (2006). "Cyclic Lateral Load Behavior of a Pile Cap and Backfill." Journal of Geotechnical & Geoenvironmental Engineering, 11.

Rollins, K. M., Gerber, T. M., and Heiner, L. (2010). "Passive Force-Deflection Behavior for Abutments With MSE Confined Approach Fills." Brigham Young University Department of Civil & Environmental Engineering, Salt Lake City, UT, 83.

Rollins, K. M., Nasr, M., and Gerber, T. M. (2010). "Numerical Analysis of Dense Narrow Backfills for Increased Passive Resistance." Report No. UT-10.19, Research Division, Utah Department of Transportation, 192 p.

Rollins, K. M., and Sparks, A. (2002). "Lateral Resistance of Full-Scale Pile Cap with Gravel Backfill." Journal of Geotechnical and Geoenvironmental Engineering, 128(9), 711-723.

Shamsabadi, A., Kapuskar, M., and Zand, A. (2006). "Three-Dimensional Nonlinear Finite-Element Soil-Abutment Structure Interaction Model for Skewed Bridges." Fifth National Seismic Conference on Bridges & Highways San Francisco, CA, 14.

Shamsabadi, A., Kapuskar, M., and Zand, A. (2006). "Three-Dimensional Nonlinear Finite-Element Soil-Abutment Structure Interaction Model for Skewed Bridges." 5th National Seismic Conference On Bridges and Highways, FHWA, ed.San Francisco, CA, 1-10.

Shamsabadi, A., Rollins, K. M., and Kapuskar, M. (2007). "Nonlinear Soil-Abutment-Bridge Structure Interaction for Seismic Performance-Based Design." *Journal of Geotechnical & Geoenvironmental Engineering*, 133(6), 14p.

Shamsabadi, A. and Rollins, K.M. (2014). "Three-dimensional nonlinear continuum seismic soil-structure interaction analysis of skewed bridge abutments." Procs., Eighth European Conference on Numerical Methods in Geotechnical Engineering, Delft, the Netherlands, 6 p.

Smith, K. (2014). "Passive Force on Skewed Bridge Abutments with Reinforced Concrete (RC) Wingwalls Based on Large-Scale Tests." M.S., Brigham Young University, Provo, Utah.

Strassburg, A. N. (2010). "Influence of Relative Compaction on Passive Resistance of Abutments with Mechanically Stabilized Earth (MSE) Wingwalls." Master of Science, Brigham Young University, Provo, Utah.

Taylor, A. J. (2006). "Full-Scale-Lateral-Load Test of a 1.2 m Diameter Drilled Shaft in Sand."M.S. Thesis, Brigham Young University, Provo, Utah.

Terzaghi, K. (1943). Theoretical Soil Mechanics, J. Wiley & Sons, New York.

Toro, F., Rubilar, F., Hube, M. A., Santa-Maria, H., and Cabrera, T. (2013). "Statistical Analysis of Underpass Damaged During 2010 Chile Earthquake." Proc. 7th National Seismic Conference of Bridges and Highways (7NSC),Oakland, CA.

Wilson, P., and Elgamal, A. (2010). "Large-Scale Passive Earth Pressure Load-Displacement Tests and Numerical Simulation." Journal of Geotechnical and Geoenvironmental Engineering, ASCE, 136(12), 1634-1643.